Turbulent Combined Wave-Current Boundary Layer Model for Application in Coastal Waters

by

Chelsea Joy Humbyrd

B.S. Ocean Engineering
Texas A&M University, 2008

Submitted to the Department of Civil and Environmental Engineering
in partial fulfillment of the requirements for the degree of

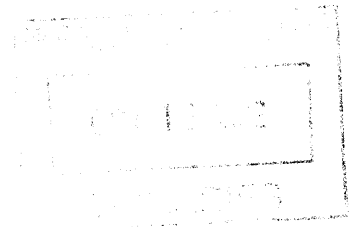Master of Science in Civil and Environmental Engineering
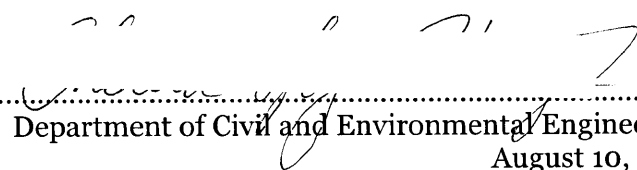
at the
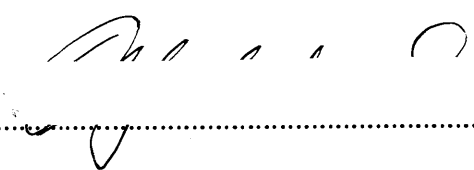
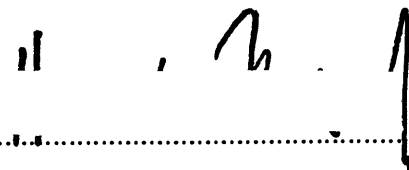Massachusetts Institute of Technology

September 2012

Author ....
Department of Civil and Environmental Engineering
August 10, 2012

Certified by...
Ole Secher Madsen
Donald and Martha Harleman Professor of Civil and Environmental Engineering
Thesis Supervisor

Accepted by...
Heidi M. Nepf
Chair, Departmental Committee for Graduate Students

Turbulent Combined Wave-Current Boundary Layer Model for Application in Coastal Waters

by

Chelsea Joy Humbyrd

Submitted to the Department of Civil and Environmental Engineering
on August 10, 2012 in partial fulfillment of the
requirements for the degree of Master of Science in
Civil and Environmental Engineering

Abstract

Accurately predicting transport processes, including sediment transport, in the coastal environment is impossible without correct current velocity and shear stress information. A combined wave-current boundary layer theory is necessary to predict these quantities, and while the previous Grant-Madsen type boundary layer models are effective, they inconsistently apply a discontinuous two layer eddy viscosity structure to the wave and current problems. We have therefore developed a new continuous three layer model which consistently applies all three layers and leads to a strong coupling between the wave and current solutions.

Boundary layer models require an estimate of the movable bed roughness, and while this roughness is scaled by the sand grain diameter for flat beds, in the coastal environment it is often the case that either wave-generated ripples cover the bed or the near-bed sediment is transported as sheet flow, in which case the roughness is much larger and less straightforward to characterize. The common method of predicting roughness in the ripple regime, while effective, unnecessarily predicts ripple geometry and requires a model-dependent factor, which varies widely, relating ripple geometry and bottom roughness. We have therefore developed an alternative, more direct method of predicting bed roughness: the wave energy dissipation factor is predicted from flow and sediment information and then any desired theoretical friction factor model is used to back-calculate the roughness. This proposed method can also be used in the sheet flow regime, allowing a continuous transition between the two regimes, not possible with the common method.

This thesis derives the new three layer combined wave-current boundary layer theory, develops the common and proposed methods of predicting roughness in the ripple and sheet flow regimes, and presents results of evaluating the theory and methods with field data. The new theory combined with either roughness method successfully predicts current shear velocities in wave-current field flows over beds in the lower flat-bed, ripple, and sheet flow regimes, with the proposed method yielding the smaller bias. Remaining questions concerning the appropriate near-bottom orbital velocity required to describe field conditions must be resolved when additional field data becomes available.

Thesis Supervisor: Ole Secher Madsen

Title: Donald and Martha Harleman Professor of Civil and Environmental Engineering

Contents

List of Figures

List of Tables

Chapter 1

Introduction

Transport processes in the coastal environment, such as oil spills, ocean outfalls, and sediment transport, have huge environmental and economic impacts, and accurately predicting them is of crucial importance. Oil spill cleanup efforts rely on predictions of the spatial and temporal distribution of the oil, which is advected by the surface currents. Evaluating the environmental impacts of ocean outfalls, such as identifying the region surrounding an outfall where concentrations of contaminants are high enough to pose a health risk, is determined by the ambient current. How much sediment is brought into suspension depends on the near-bottom shear stress; once entrained at the bottom, the sediment diffuses up into the overlying water column and is transported by the current. Clearly, accurately predicting transport processes in the coastal environment is impossible without correct current velocity and shear stress information.

In the nearshore coastal environment, where one expects both waves and currents to be present to some degree, it is important to understand the ways in which waves increase the flow resistance and act to retard to current. For moderately strong wave conditions the waves create ripples on the bed, and for very strong waves the near-bed sediment is transported as sheet flow; both of these conditions increase the physical bottom roughness over that of a flat bottom. The second way that waves retard the current is through interaction within the turbulent wave boundary layer, producing an apparent roughness that is much larger than the physical roughness. It is this apparent roughness that is experienced by currents in the presence of

waves. The end result is that when waves are present a current will experience a dramatic increase in apparent bottom roughness, often several orders of magnitude larger than the sand grain diameter, and a correspondingly large reduction in velocity, often by a factor of two, relative to the current velocity in the absence of waves.

The interaction between waves and currents in the near-bottom region, including the relationship between the apparent and physical roughness, is predicted by a hydrodynamic model for combined wave-current boundary layer flows. The physical bottom roughness is estimated with empirical methods independent of the wave-current model, typically by assuming the physical roughness is determined solely by the wave motion.

The Grant-Madsen type wave-current interaction models are widely used due to their physical basis and ease of use; they began with one of the first published wave-current models, that of Grant and Madsen (1979), and continue with the modified forms of Madsen (1994) and Madsen and Salles (1998). These models solve the linearized boundary layer equations, which assume uniform flow and thus neglect convective accelerations. They utilize a two layer, bi-linear, time-invariant eddy viscosity model. Because the eddy viscosity is time-invariant, the time-varying and time-invariant components of the linearized governing equation are separated into two independent equations, one for the waves and another for the current, which are considered individually. The wave problem is then solved assuming that the waves are so much stronger than the current that the current can be neglected in the wave solution. The Grant-Madsen type models have been shown to give excellent results when compared to measurements when the waves and currents are collinear, with less accurate but still adequate results when the waves and currents act at larger angles.

More complicated analytical models include those that employ a time-varying eddy viscosity, such as Trowbridge and Madsen (1984) and Gonzalez-Rodriguez and Madsen (2011). Numerical wave-current models typically utilize a $k - \epsilon$ turbulence closure model for the eddy viscosity, such as Davies et al. (1988), and Holmedal et al. (2003). While these numerical

models provide insights into the non-linear processes, they are typically too computationally expensive to use in practical coastal engineering applications.

The Grant-Madsen type boundary layer models are simple yet accurate, and are fairly widely used. However, the models use a discontinuous two layer eddy viscosity in the current problem, but in the wave problem the lower linearly varying eddy viscosity layer is assumed to extend throughout the wave boundary layer, which in effect inconsistently applies a linear model for the wave solution. Therefore, we will develop a new wave-current theory, which is based on the existing Grant-Madsen theory, but employs a three layer continuous eddy viscosity model and consistently uses all three layers in the solution of both the current and wave problems.

All of the wave-current hydrodynamic models require an estimate of the movable bed roughness, whose prediction method depends on the regime of the sediment bed. For flat sand beds, which are found with limited wave action, this roughness is simply scaled by the sand grain diameter. For stronger wave conditions, however, where wave-generated ripples cover the bed, the roughness is scaled by the ripple dimensions. In the ripple regime, therefore, the roughness is often naturally taken as a function of the ripple geometry, which is predicted from fluid, flow, and sediment parameters. Finding the roughness with this method, however, requires a constant that depends on the choice of theoretical friction factor model. Sheet flow conditions are found for even stronger wave conditions. Finding the roughness using the common method in the sheet flow regime also requires a model-dependent constant.

To find the roughness in the ripple regime, instead of first predicting the ripple dimensions, which are not otherwise needed, we propose to directly predict the wave energy dissipation factor, which can be obtained experimentally and is not model-dependent. Any model can then be used to back-calculate the bed roughness. This proposed energy friction factor method is also applicable to the sheet flow regime, which allows a continuous variation in the roughness prediction between the two regimes. Since the model-dependent constants used

in the common method are determined using the energy friction factor data, the proposed method can be expected to give equal or improved accuracy, and is much simpler.

The goals of this thesis are to develop a consistent theoretical wave-current boundary layer model, to derive expressions for empirical relationships for the bed roughness, and to validate the theoretical model and empirical roughness relationships with wave-current field data.

In Chapter 2 we present the derivation of the three layer turbulent wave-current boundary layer model. As opposed to the previous Grant-Madsen type models, this model consistently uses the same three layer eddy viscosity model in both the current and wave solution. Since it is cumbersome to solve the exact three layer current profile, we also provide an equivalent two layer simplification. Because the wave problem always uses the full three layer model, the simplification gives the same shear stresses and apparent roughness as the full model, the formulations only differ in the current velocity profile very near the transition level, which is of little importance. Using the simplified two layer current velocity profile allows a simple solution procedure which is very similar to that of the original Grant-Madsen models, which employed a two layer eddy viscosity model for the current problem. The results of the model are presented graphically for ranges of the pertinent parameters, and explicit approximations are provided to simplify calculations. The wave-current solution procedure is described and the model is evaluated by comparing predicted current profiles with numerical and laboratory experimental results. Finally, the friction factor relationship for the new model is compared to previously published and tested theories.

The movable bed roughness is an important input into the boundary layer theory developed in Chapter 2, and it depends strongly on the movable bed regime. Chapter 3 describes the three relevant movable bed regimes: the lower flat-bed, ripple, and sheet flow regime, and characterizes the flow conditions that lead to each regime. For the ripple regime, we give a sample of published relationships for the ripple height, and then present our new relationship

developed with laboratory data. We then present relationships for the energy friction factor for the ripple and sheet flow regimes, which provide an alternative method of finding the roughness.

In Chapter 4, the relationships developed in Chapter 3 are used to develop methods of determining the roughness in the different regimes. In the ripple and sheet flow regimes, two methods are considered: the common method is more direct but includes a model-dependent constant; the proposed method is based on measurements of the energy friction factor and is independent of friction factor model. The common method requires a friction factor model-dependent factor, and the best-fit factors for the ripple and sheet flow regimes are found for laboratory data using the new boundary layer theory. The results of back-calculating the roughness from the energy friction factor relationships are provided to illustrate the proposed roughness method. The roughness procedure for all three regimes is then summarized.

In Chapter 5, the wave-current theory derived in Chapter 2 and the roughness methods developed in Chapters 3 and 4 are evaluated using data on combined wave-current flows in the field. The results using the different roughness methods in the different regimes are presented, and different ways of characterizing random waves under field conditions are considered.

Chapter 2

Turbulent combined wave-current boundary layer theory

In this chapter we present a relatively simple hydrodynamic model for turbulent combined wave-current boundary layer flows. Most analytical boundary layer models employ a time-invariant eddy viscosity model, and for simplicity we will continue that trend with this current model. However, while many models divide the flow into two layers for the eddy viscosity structure, we use a continuous three layer model, and we consistently use all three layers in the solutions for both the wave and current. The current and wave problems are described and the model results are presented for a range of the applicable parameters. We then outline the suggested solution procedure to solve combined wave-current problems using the new three layer wave-current model. The new model is tested against results from both a more complex numerical model and from fixed-bed experiments, where the bed roughness is well quantified. The friction factor variation predicted from the new three layer model is then compared to other accepted published friction factor models whose applicability has been more widely examined.

2.1   Three layer model for combined wave-current flows

The Grant-Madsen type boundary layer models, the most recent of which are Madsen (1994) and Madsen and Salles (1998), assume a time-invariant discontinuous two layer vertical structure for the eddy viscosity. The eddy viscosity profile consists of two linear segments, one inside the wave boundary layer and the other outside it, within the current boundary layer. The

wave friction factor, phase shift, and wave boundary layer thickness, however, were developed ignoring the effect of currents, therefore the effective eddy viscosity for the wave solution extends the bottom layer to the whole depth, giving a simple linear profile (Madsen, 1994; Madsen and Salles, 1998). As this two layer model uses a different eddy viscosity formulation for the wave and current problems, we decided to develop a three layer model which consistently applies the same eddy viscosity structure for the entire problem. Also, the continuous eddy viscosity variation resulting from including a third, middle layer yields a smooth velocity profile, providing a more realistic transition from the wave to the current boundary layer.

The linearized governing equation for a wave-current boundary layer, assuming uniform flow and thus neglecting convective accelerations, can be written as

$$\rho \frac{\partial \vec{u}}{\partial t} = -\nabla p + \frac{\partial \vec{\tau}}{\partial z} \tag{2.1}$$

where $\vec{u}$ is the horizontal velocity vector, p is the pressure, $\vec{\tau}$ is the shear stress vector, z is the elevation above the bottom, and ρ is the fluid density. For turbulent flows, the shear stress is related to the velocity through the turbulent eddy viscosity, ν_t, by

$$\frac{\vec{\tau}}{\rho} = \nu_t \frac{\partial \vec{u}}{\partial z} \tag{2.2}$$

Inserting (2.2) into (2.1) yields

$$\frac{\partial \vec{u}}{\partial t} = -\frac{1}{\rho} \nabla_{\mathrm{h}} p + \frac{\partial}{\partial z}\left(\nu_t \frac{\partial \vec{u}}{\partial z}\right) \tag{2.3}$$

where ∇_{h} denotes the gradient operator in the horizontal (x, y) directions.

To make this problem tractable analytically, a model for the eddy viscosity structure must be chosen. Within the wave boundary layer, $z < \delta_w$, the eddy viscosity is scaled by the maximum combined wave-current shear velocity, u_{*m}, given by

$$\rho u_{*m}^2 = \tau_m = |\vec{\tau}_{wm} + \vec{\tau}_c| \tag{2.4}$$

where the magnitude of the maximum combined shear stress, τ_m, is the vector sum of the maximum wave shear stress, $\tau_{wm} = \rho u_{*wm}^2$, and the current shear stress, $\tau_c = \rho u_{*c}^2$. Outside the wave boundary layer the eddy viscosity is scaled by the current shear velocity, u_{*c}.

The vertical scale of the wave boundary layer, l, is given by

$$l = \frac{\kappa u_{*m}}{\omega} \tag{2.5}$$

where $\omega = 2\pi/T$ is the wave orbital frequency and κ is von Kármán's constant ($\kappa \approx 0.4$). The non-dimensional vertical coordinate is then

$$\zeta = \frac{z}{l} \tag{2.6}$$

and the other vertical distances can be similarly non-dimensionalized, e.g., $\zeta_w = \delta_w/l$.

Based on law-of-the-wall arguments, the eddy viscosity near the boundary should vary linearly. For steady turbulent flow, the most common eddy viscosity models are, in increasing order of complexity, linear, linear-constant, and parabolic. The linear-constant variation is often used due to its balance between simplicity and accuracy. It can be shown that by taking the transition level between linear and constant variations at 1/6 of the water depth, the resulting velocity profile well represents the accepted logarithmic profile for steady flow (Clauser, 1956). Generalizing from the steady case, we choose to take a time-invariant linear-constant eddy viscosity profile within the wave boundary layer with the transition from linear to constant portions occurring at 1/6 of the thickness of the wave boundary layer. At distances well above the wave boundary layer the eddy viscosity variation has little effect on the solution, so we choose to use a simple linear variation. The full three layer eddy viscosity model for combined wave-current flows is therefore

$$\nu_t = \begin{cases} \kappa u_{*m} z, & z_0 \leq z < \delta_t \\ \kappa u_{*m} \delta_t, & \delta_t \leq z < \frac{u_{*m}}{u_{*c}}\delta_t \\ \kappa u_{*c} z, & z > \frac{u_{*m}}{u_{*c}}\delta_t \end{cases} \tag{2.7}$$

21

where δ_t is the lower transition level between linear and constant portions and z_0 is the elevation of the theoretical bottom, where the velocity vanishes. This reasonably simple eddy viscosity is illustrated in Figure 2-1.
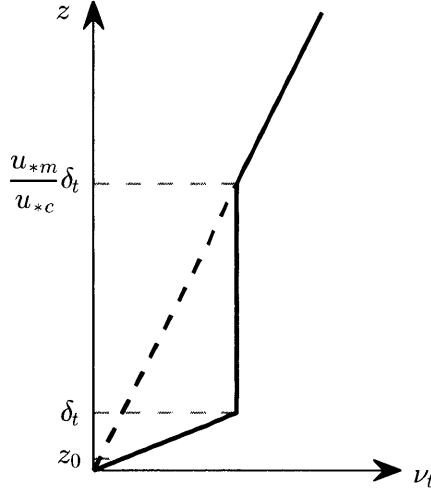
Figure 2-1: Illustration of three layer eddy viscosity structure, as defined by (2.7), assuming $\delta_t = \delta_w/6 > z_o$.

As mentioned above, the transition between the bottom two layers is taken to be at 1/6 of the thickness of the wave boundary layer, or $\delta_t = \delta_w/6$. However, it is possible with a very rough bottom for the elevation of the theoretical bottom, z_0, to be located above the level $\delta_w/6$, in which case the constant portion of the eddy viscosity model extends all the way to z_0, effectively reducing the model to two layers. To account for this effect, the transition level between the bottom two regions is explicitly defined as

$$\delta_t = \max\{\delta_w/6, z_0\} \qquad (2.8)$$

where the roughness length z_0, the elevation of the theoretical bottom, is given by

$$z_0 = \max\left\{\frac{\nu}{9u_{*m}}, \frac{k_N}{30}\right\} \qquad (2.9)$$

where ν is the kinematic viscosity of water and k_N is the equivalent Nikuradse sand grain roughness, and the two expressions are valid for smooth and rough turbulent flow, respectively.

The transition level between the top two layers is located at $z = (u_{*m}/u_{*c})\delta_t$. To simplify the expressions, we define a parameter α as the current-maximum shear velocity ratio, which varies between $\alpha = 0$ for the pure wave case to $\alpha = 1$ for the pure current case,

$$\alpha = \frac{u_{*c}}{u_{*m}} \tag{2.10}$$

Note that using this parameter, the transition level between the upper two layers is simply $z = \delta_t/\alpha$. For the pure wave case, with $\alpha = 0$, the upper transition level goes to infinity, and the eddy viscosity becomes a two layer linear-constant model, while for the pure current case, with $\alpha = 1$, the upper transition level is the same as the lower transition level, and the eddy viscosity becomes a simple linear model (Figure 2-2). Note that, as mentioned above, for very rough conditions it is possible to have $\delta_t = z_0 > \delta_w/6$, in which case the eddy viscosity structure for the pure wave case would reduce to a simple constant model.
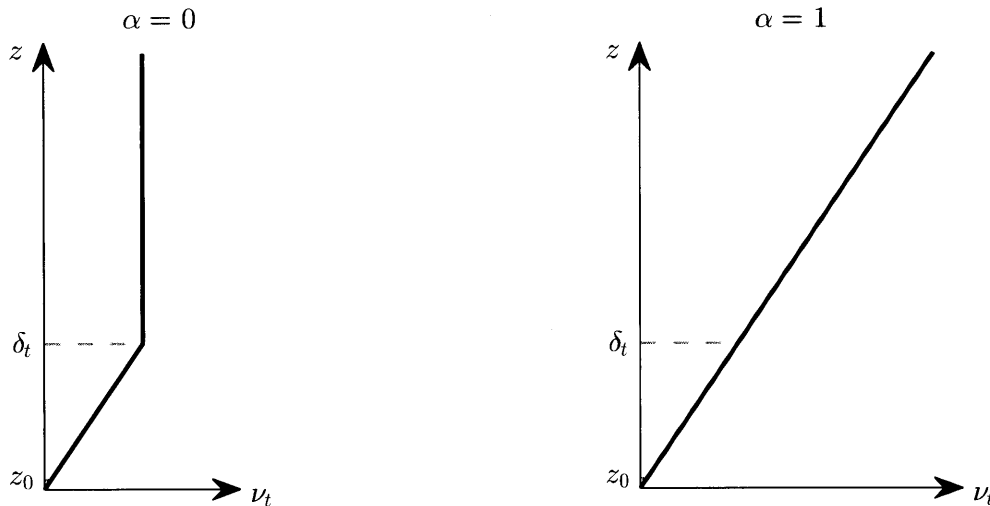
Figure 2-2: Illustration of the limits of the three layer eddy viscosity structure, for $\alpha = 0$ and $\alpha = 1$, assuming $\delta_t > z_o$.

As the shear velocities and the eddy viscosity are time-invariant, the velocity and pressure can be resolved into their mean and time-varying components, where the mean component is related to the current and the time-varying component is related to the oscillatory wave motion,

$$\vec{u} = \vec{u}_w + \vec{u}_c$$

$$p = p_w + p_c \tag{2.11}$$

where the subscripts w and c refer to the wave and current components, respectively. Introducing these expressions into the governing equation, (2.3), yields two separate equations for the wave and current motion. In order to describe the wave and current motions in terms of magnitudes and not vector quantities, we define the x-direction as the direction of wave propagation, and the current velocity is directed at an angle ϕ_{cw} from the x-axis, where ϕ_{cw} is the acute angle between the wave and current directions. The wave motion is described by

$$\frac{\partial \tilde{u}_w}{\partial t} = -\frac{1}{\rho}\frac{\partial \tilde{p}_w}{\partial x} + \frac{\partial}{\partial z}\left(\nu_t \frac{\partial \tilde{u}_w}{\partial z}\right) \tag{2.12}$$

where the tilde denotes time-varying quantities. Using the relationship predicted by potential theory between the wave-induced pressure and the near-bottom velocity, $\tilde{u}_b$, the wave equation reduces to

$$\frac{\partial (\tilde{u}_w - \tilde{u}_b)}{\partial t} = \frac{\partial}{\partial z}\left(\nu_t \frac{\partial (\tilde{u}_w - \tilde{u}_b)}{\partial z}\right) \tag{2.13}$$

Based on a law-of-the-wall argument, the pressure gradient term in the current equation can be neglected, and the magnitude of the current motion is therefore described by

$$\frac{\tau_c}{\rho} = u_{*c}^2 = \nu_t \frac{du_c}{dz} \tag{2.14}$$

where the definition of the current shear stress at the bottom has been used. The direction of the current as well as its bottom shear stress, τ_c, is at an angle ϕ_{cw} to the x-axis, that is, the wave direction.

2.1.1   Current solution

With the eddy viscosity model given by (2.7), and the governing equation for the current motion by (2.14), the general equation for the current at all three levels is given by

24

$$u_{*c}^2 = \begin{cases} \kappa u_{*m} z \dfrac{du_c}{dz}, & z_0 < z < \delta_t \\[2ex] \kappa u_{*m} \delta_t \dfrac{du_c}{dz}, & \delta_t < z < \delta_t/\alpha \\[2ex] \kappa u_{*c} z \dfrac{du_c}{dz}, & z > \delta_t/\alpha \end{cases} \qquad (2.15)$$

For the bottom layer, where the eddy viscosity is linear, the solution to (2.15) is

$$u_c = \alpha \frac{u_{*c}}{\kappa} \ln\left(\frac{z}{z_0}\right) = \alpha \frac{u_{*c}}{\kappa} \ln\left(\frac{\zeta}{\zeta_0}\right) \qquad (2.16)$$

where the no-slip bottom boundary condition has been applied at z_0. Then for the intermediate layer, with a constant eddy viscosity, the general solution to (2.15) is

$$u_c = \alpha \frac{u_{*c}}{\kappa} \left(\frac{z}{\delta_t} + C_1\right) = \alpha \frac{u_{*c}}{\kappa} \left(\frac{\zeta}{\zeta_t} + C_1\right) \qquad (2.17)$$

The constant C_1 is found by requiring the velocity to be continuous at $z = \delta_t$, which gives

$$u_c = \alpha \frac{u_{*c}}{\kappa} \left(\frac{z}{\delta_t} + \ln\left(\frac{\delta_t}{z_0}\right) - 1\right) = \alpha \frac{u_{*c}}{\kappa} \left(\frac{\zeta}{\zeta_t} + \ln\left(\frac{\zeta_t}{\zeta_0}\right) - 1\right) \qquad (2.18)$$

For the upper layer, the eddy viscosity is again linear, and the general solution to (2.15) is

$$u_c = \frac{u_{*c}}{\kappa} \ln z + C_2 = \frac{u_{*c}}{\kappa} \ln \zeta + C_2' \qquad (2.19)$$

The constant C_2 or C_2' is found by requiring the velocity to be continuous between the middle and upper layers at $z = \delta_t/\alpha$, which gives

$$u_c = \frac{u_{*c}}{\kappa} \left[\ln\left(\alpha \frac{z}{\delta_t}\right) + 1 + \alpha\left(\ln\left(\frac{\delta_t}{z_0}\right) - 1\right)\right] = \frac{u_{*c}}{\kappa} \left[\ln\left(\alpha \frac{\zeta}{\zeta_t}\right) + 1 + \alpha\left(\ln\left(\frac{\zeta_t}{\zeta_0}\right) - 1\right)\right] \qquad (2.20)$$

The velocity in the upper layer follows a simple logarithmic profile, so by combining the constants it can also be written as

$$u_c = \frac{u_{*c}}{\kappa} \ln\left(\frac{z}{z_{0a}}\right) \qquad (2.21)$$

25

where z_{0a} is the apparent roughness, the elevation of zero velocity if the top layer profile were extended towards the bottom. Thus, the apparent roughness is found from setting the current velocity in (2.20) equal to zero at $z = z_{0a}$, which gives

$$\frac{z_{0a}}{z_0} = \frac{1}{\alpha}\left(\frac{\delta_t}{ez_0}\right)^{1-\alpha} \tag{2.22}$$

where $e = \exp\{1\}$.

Combined, the full current velocity profile is

$$u_c = \begin{cases} \alpha\dfrac{u_{*c}}{\kappa}\ln\left(\dfrac{z}{z_0}\right), & z_0 < z < \delta_t \\[2ex] \alpha\dfrac{u_{*c}}{\kappa}\left(\dfrac{z}{\delta_t} + \ln\left(\dfrac{\delta_t}{z_0}\right) - 1\right), & \delta_t < z < \delta_t/\alpha \\[2ex] \dfrac{u_{*c}}{\kappa}\left[\ln\left(\alpha\dfrac{z}{\delta_t}\right) + 1 + \alpha\left(\ln\left(\dfrac{\delta_t}{z_0}\right) - 1\right)\right], & z > \delta_t/\alpha \end{cases} \tag{2.23}$$

This three layer velocity profile is nice because it is smooth, but it is clumsy to work with and having an accurate representation of the velocity in the middle layer is not critical. Therefore, we can sacrifice smoothness and consistency and find an equivalent two layer profile for the current, by extending the bottom and top layers until they meet. This way, the only difference between the two profiles is in the middle layer. Therefore, the three layer continuous eddy viscosity model given by (2.7) becomes the simpler, but discontinuous eddy viscosity model in (2.24), consisting of the two linear segments of the top and bottom layers,

$$v_t = \begin{cases} \kappa u_{*m}z, & z < \delta_{cw} \\ \kappa u_{*c}z, & z > \delta_{cw} \end{cases} \tag{2.24}$$

where δ_{cw}, the wave-current boundary layer thickness, is the transition level between the bottom layer, scaled by the maximum combined shear velocity, and the top layer, scaled by the current shear velocity. The bottom and top layers approximately correspond to the wave and current boundary layers, respectively, although the wave boundary layer thickness, δ_w, is almost always greater than δ_{cw} ($\delta_w < \delta_{cw}$ only occurs for very small values of α, $\alpha \lesssim 0.076$). The transition level is found by equating the top and bottom velocity profiles at $z = \delta_{cw}$, which gives

$$\delta_{cw} = \frac{\delta_t}{e} \alpha^{\left(\frac{1}{\alpha-1}\right)} \tag{2.25}$$

The two layer velocity profile resulting from this simplified eddy viscosity model is given by

$$u_c = \begin{cases} \alpha \dfrac{u_{*c}}{\kappa} \ln\left(\dfrac{z}{z_0}\right), & z < \delta_{cw} \\[3mm] \dfrac{u_{*c}}{\kappa} \ln\left(\dfrac{z}{z_{0a}}\right), & z > \delta_{cw} \end{cases} \tag{2.26}$$

The apparent roughness, z_{0a}, can be written in terms of δ_{cw} using (2.25) in (2.22),

$$\frac{z_{0a}}{z_0} = \left(\frac{\delta_{cw}}{z_0}\right)^{1-\alpha} \tag{2.27}$$

For the pure-current case, when $\alpha = 1$, $z_{0a} = z_0$, and the current profile (2.26) reduces to the simple logarithmic steady current profile, as expected.

An example comparison of the eddy viscosity structure and the current velocity profile for the three layer model and the simplified two layer model is shown in Figure 2-3. The non-dimensional eddy viscosity, $\nu_t/(\kappa u_{*m} \delta_t)$, and current velocity, $u_c/(u_{*c} \kappa)$, are plotted against the non-dimensional elevation, z/δ_t. Using these scalings, the only parameters which must be chosen are α and z_0/δ_t, which are arbitrarily chosen to be $\alpha = 0.25$ and $z_0/\delta_t = 0.01$.
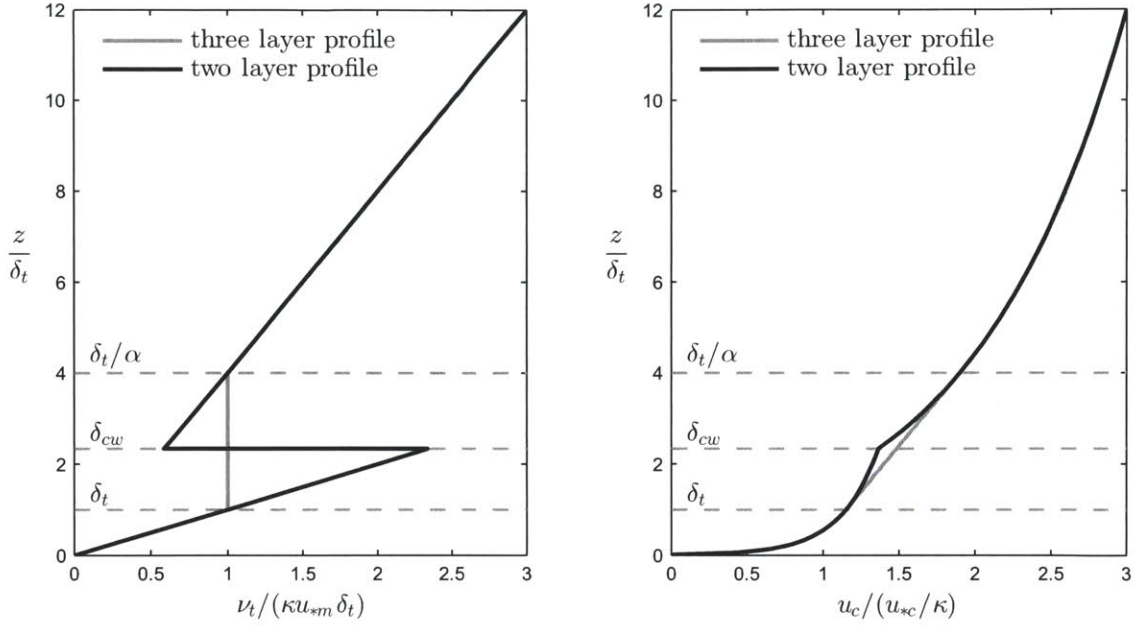
Figure 2-3: Comparison of eddy viscosity structure (left) and current velocity profile (right) for the three layer model (gray) and the two layer simplification (black) for $\alpha = 0.25$ and $z_o/\delta_t = 0.01$.

The transition level between the two layers of the simplified two layer profile was derived in this section by matching the velocity profiles from the top and bottom layers. As derived in the Appendix, the same transition level is found for simplifying a three layer suspended sediment concentration profile to two layers.

The current velocity profile is thus given by either (2.23) or (2.26) for the three and two layer profiles, respectively. In either case, to evaluate the expressions requires knowledge of α and δ_t, which in turn are dependent on the maximum combined shear velocity, u_{*m}, and the wave boundary layer thickness, δ_w, respectively. These parameters are found from the wave solution and the friction factor closure.

2.1.2 Wave solution

According to linear theory, the wave orbital velocity at the bottom is

$$\tilde{u}_b = u_{bm}\mathcal{R}e\{e^{i\omega t}\} = u_{bm}\cos\omega t \tag{2.28}$$

28

where u_{bm} is the magnitude of the bottom orbital velocity, the operator $\mathcal{R}e$ indicates the real part of the argument, and i is the imaginary unit. We define the normalized deficit velocity as

$$\tilde{u}_d = \frac{\tilde{u}_w - \tilde{u}_b}{u_{bm}} \tag{2.29}$$

and

$$\tilde{u}_d = \mathcal{R}e\{u_d e^{i\omega t}\} \tag{2.30}$$

where u_d is the complex magnitude of the deficit velocity. Substituting (2.29) into the governing equation for the wave motion, (2.13), gives

$$\frac{\partial \tilde{u}_d}{\partial t} = \frac{\partial}{\partial z}\left(\nu_t \frac{\partial \tilde{u}_d}{\partial z}\right) \tag{2.31}$$

and applying (2.30) yields the governing equation for the time-varying component of the velocity field within the wave boundary layer,

$$\frac{d}{dz}\left(\nu_t \frac{du_d}{dz}\right) - i\omega u_d = 0 \tag{2.32}$$

Using the three layer eddy viscosity model described by (2.7), general solutions for the deficit velocity can be found for each of the three regions. In the lower region, $z < \delta_t$, where the eddy viscosity is linear, (2.32) becomes

$$\frac{d}{dz}\left(\kappa u_{*m} z \frac{du_d}{dz}\right) - i\omega u_d = 0 \tag{2.33}$$

or, invoking (2.5) and (2.6),

$$\frac{d}{d\zeta}\left(\zeta \frac{du_d}{d\zeta}\right) - i u_d = 0 \tag{2.34}$$

Using Hildebrand (1976), the general solution to (2.34) is

$$u_d = A\left(\ker 2\sqrt{\zeta} + i\,\mathrm{kei}\,2\sqrt{\zeta}\right) + B\left(\mathrm{ber}\,2\sqrt{\zeta} + i\,\mathrm{bei}\,2\sqrt{\zeta}\right) \tag{2.35}$$

where ker, kei, ber, and bei are Kelvin functions of zeroth order and A and B are complex constants.

In the intermediate region, $\delta_t < z < \delta_t/\alpha$, where the eddy viscosity is constant, the governing equation (2.32) becomes

$$\kappa u_{*m}\delta_t \frac{d^2 u_d}{dz^2} - i\omega u_d = 0 \tag{2.36}$$

Or, using the non-dimensional boundary layer scale (2.6),

$$\frac{d^2 u_d}{d\zeta^2} - \frac{i}{\zeta_t} u_d = 0 \tag{2.37}$$

with the general solution

$$u_d = C e^{-\sqrt{i}\frac{\zeta}{\sqrt{\zeta_t}}} + D e^{\sqrt{i}\frac{\zeta}{\sqrt{\zeta_t}}} \tag{2.38}$$

where C and D are complex constants and $\sqrt{i} = (1+i)/\sqrt{2}$.

In the upper region, $z > \delta_t/\alpha$, the eddy viscosity is again linear, and (2.32) becomes

$$\frac{d}{dz}\left(\kappa u_{*c} z \frac{du_d}{dz}\right) - i\omega u_d = 0 \tag{2.39}$$

Or, using (2.5), (2.6), and (2.10),

$$\frac{d}{d\zeta}\left(\zeta \frac{du_d}{d\zeta}\right) - \frac{i}{\alpha} u_d = 0 \tag{2.40}$$

Using Hildebrand (1976), the general solution to (2.40) is

$$u_d = E\left(\mathrm{ker}\, 2\sqrt{\zeta/\alpha} + i\,\mathrm{kei}\, 2\sqrt{\zeta/\alpha}\right) + F\left(\mathrm{ber}\, 2\sqrt{\zeta/\alpha} + i\,\mathrm{bei}\, 2\sqrt{\zeta/\alpha}\right) \tag{2.41}$$

where E and F are complex constants. For the upper boundary condition the wave velocity must equal the near-bottom velocity, or the deficit velocity must vanish far away from the bottom, $u_d \to 0$ as $\zeta \to +\infty$. Since ber and bei become exponentially large when their arguments go to infinity, it can be seen that

$$F = 0 \tag{2.42}$$

and (2.41) becomes

$$u_d = E\left(\mathrm{ker}\, 2\sqrt{\zeta/\alpha} + i\,\mathrm{kei}\, 2\sqrt{\zeta/\alpha}\right) \tag{2.43}$$

Combining (2.35), (2.38), and (2.43), the full deficit velocity profile can be written as

$$
u_d = \begin{cases}
A\big(\ker 2\sqrt{\zeta} + i\,\mathrm{kei}\,2\sqrt{\zeta}\big) + B\big(\mathrm{ber}\,2\sqrt{\zeta} + i\,\mathrm{bei}\,2\sqrt{\zeta}\big), & \zeta_0 < \zeta < \zeta_t \\[2mm]
Ce^{-\sqrt{i}\frac{\zeta}{\sqrt{\zeta_t}}} + De^{\sqrt{i}\frac{\zeta}{\sqrt{\zeta_t}}}, & \zeta_t < \zeta < \zeta_t/\alpha \\[2mm]
E\big(\ker 2\sqrt{\zeta/\alpha} + i\,\mathrm{kei}\,2\sqrt{\zeta/\alpha}\big), & \zeta > \zeta_t/\alpha
\end{cases}
\tag{2.44}
$$

There are five complex constants remaining, which require five conditions: the remaining bottom boundary condition and four matching conditions, for the velocities and shear stresses at each of the two transition levels. Since ν_t is continuous, matching the shear stress is equivalent to matching the velocity gradient. Because the derivatives of Kelvin functions will be used multiple times, the generic form is given here (Abramowitz and Stegun, 1972).

$$
\begin{aligned}
\frac{d}{d\zeta}\Big(\ker\big(2\sqrt{\zeta/\alpha}\big)\Big) &= \frac{1}{\sqrt{2\alpha\zeta}}\big[\ker_1\big(2\sqrt{\zeta/\alpha}\big) + \mathrm{kei}_1\big(2\sqrt{\zeta/\alpha}\big)\big] \\
\frac{d}{d\zeta}\Big(\mathrm{kei}\big(2\sqrt{\zeta/\alpha}\big)\Big) &= \frac{1}{\sqrt{2\alpha\zeta}}\big[-\ker_1\big(2\sqrt{\zeta/\alpha}\big) + \mathrm{kei}_1\big(2\sqrt{\zeta/\alpha}\big)\big] \\
\frac{d}{d\zeta}\Big(\mathrm{ber}\big(2\sqrt{\zeta/\alpha}\big)\Big) &= \frac{1}{\sqrt{2\alpha\zeta}}\big[\mathrm{ber}_1\big(2\sqrt{\zeta/\alpha}\big) + \mathrm{bei}_1\big(2\sqrt{\zeta/\alpha}\big)\big] \\
\frac{d}{d\zeta}\Big(\mathrm{bei}\big(2\sqrt{\zeta/\alpha}\big)\Big) &= \frac{1}{\sqrt{2\alpha\zeta}}\big[-\mathrm{ber}_1\big(2\sqrt{\zeta/\alpha}\big) + \mathrm{bei}_1\big(2\sqrt{\zeta/\alpha}\big)\big]
\end{aligned}
\tag{2.45}
$$

At the bottom boundary, the no-slip condition in terms of the normalized deficit velocity is $u_d = -1$ at $\zeta = \zeta_0$. Applying this condition to (2.35) gives

$$
A\big(\ker 2\sqrt{\zeta_0} + i\,\mathrm{kei}\,2\sqrt{\zeta_0}\big) + B\big(\mathrm{ber}\,2\sqrt{\zeta_0} + i\,\mathrm{bei}\,2\sqrt{\zeta_0}\big) = -1
\tag{2.46}
$$

At the first transition level, $\zeta = \zeta_t$, the velocities from above and below must match. Using (2.44), this gives

$$
A\big(\ker 2\sqrt{\zeta_t} + i\,\mathrm{kei}\,2\sqrt{\zeta_t}\big) + B\big(\mathrm{ber}\,2\sqrt{\zeta_t} + i\,\mathrm{bei}\,2\sqrt{\zeta_t}\big) = Ce^{-\sqrt{i\zeta_t}} + De^{\sqrt{i\zeta_t}}
\tag{2.47}
$$

As ν_t is continuous at $\zeta = \zeta_t$, matching the shear stress is equivalent to matching the velocity gradient, which gives

31

$$\frac{d}{d\zeta}\left[A\left(\ker 2\sqrt{\zeta} + i\,\mathrm{kei}\,2\sqrt{\zeta}\right) + B\left(\mathrm{ber}\,2\sqrt{\zeta} + i\,\mathrm{bei}\,2\sqrt{\zeta}\right)\right]_{\zeta=\zeta_t}$$

$$= \frac{d}{d\zeta}\left[Ce^{-\sqrt{i}\frac{\zeta}{\sqrt{\zeta_t}}} + De^{\sqrt{i}\frac{\zeta}{\sqrt{\zeta_t}}}\right]_{\zeta=\zeta_t} \tag{2.48}$$

Using (2.45) with $\alpha = 1$ and simplifying, (2.48) becomes

$$A\left(-i\,\ker_1 2\sqrt{\zeta_t} + \mathrm{kei}_1\,2\sqrt{\zeta_t}\right) + B\left(-i\,\mathrm{ber}_1\,2\sqrt{\zeta_t} + \mathrm{bei}_1\,2\sqrt{\zeta_t}\right) = -Ce^{-\sqrt{i\zeta_t}} + De^{\sqrt{i\zeta_t}} \tag{2.49}$$

The velocities must also match at the second transition level, $\zeta = \zeta_t/\alpha$. Applying this condition to (2.44) gives

$$E\left[\ker\left(\frac{2}{\alpha}\sqrt{\zeta_t}\right) + i\,\mathrm{kei}\left(\frac{2}{\alpha}\sqrt{\zeta_t}\right)\right] = Ce^{-\sqrt{i\zeta_t}/\alpha} + De^{\sqrt{i\zeta_t}/\alpha} \tag{2.50}$$

Again, the eddy viscosity is continuous at $\zeta = \zeta_t/\alpha$, so matching the shear stress is equivalent to matching the velocity gradient.

$$\frac{d}{d\zeta}\left[E\left(\ker 2\sqrt{\zeta/\alpha} + i\,\mathrm{kei}\,2\sqrt{\zeta/\alpha}\right)\right]_{\zeta=\zeta_t/\alpha} = \frac{d}{d\zeta}\left[Ce^{-\sqrt{i}\frac{\zeta}{\sqrt{\zeta_t}}} + De^{\sqrt{i}\frac{\zeta}{\sqrt{\zeta_t}}}\right]_{\zeta=\zeta_t/\alpha} \tag{2.51}$$

Again, we use (2.45) and simplify (2.51) to

$$E\left[-i\,\ker_1\left(\frac{2}{\alpha}\sqrt{\zeta_t}\right) + \mathrm{kei}_1\left(\frac{2}{\alpha}\sqrt{\zeta_t}\right)\right] = -Ce^{-\sqrt{i\zeta_t}/\alpha} + De^{\sqrt{i\zeta_t}/\alpha} \tag{2.52}$$

Equations (2.46), (2.47), (2.49), (2.50), and (2.52) are five equations from which the five complex constants A, B, C, D and E may be determined. With the five constants known, the deficit velocity is given by (2.44). The five constants, and therefore the deficit velocity, are functions of α, ζ_0, and ζ_w.

The deficit velocity profile depends on the wave boundary layer thickness, $\delta_w = \zeta_w l$, which is not known a priori. We define the wave boundary layer thickness, $z = \delta_w$ or $\zeta = \zeta_w$ as the height at which the maximum boundary layer velocity deviates by ε (%) from the near-bottom wave velocity, or in terms of the normalized deficit velocity,

$$|u_d| = \varepsilon \tag{2.53}$$

For $\alpha = u_{*c}/u_{*m} > 1/6$, it follows that $\zeta_w > \zeta_t/\alpha$, and therefore the top of the wave boundary layer is located within the upper portion of the velocity profile. For this case, the normalized deficit velocity at the top of the wave boundary layer is

$$u_d = E\left(\ker 2\sqrt{\zeta/\alpha} + i \ker 2\sqrt{\zeta/\alpha}\right), \qquad \zeta > \zeta_t/\alpha \tag{2.54}$$

However, for the case when $\alpha < 1/6$, when the waves are very strong compared to the current, the wave boundary layer thickness is located within the middle, constant portion of the eddy viscosity profile. For this case, the normalized deficit velocity at the top of the wave boundary layer is

$$u_d = C e^{-\sqrt{i}\frac{\zeta}{\sqrt{\zeta_t}}} + D e^{\sqrt{i}\frac{\zeta}{\sqrt{\zeta_t}}}, \qquad \zeta_t < \zeta < \zeta_t/\alpha \tag{2.55}$$

Combining these regions, the wave boundary layer thickness can be found for any α by solving

$$\varepsilon = \begin{cases} \left| E\left(\ker 2\sqrt{\zeta_w/\alpha} + i \ker 2\sqrt{\zeta_w/\alpha}\right) \right|, & \alpha \geq 1/6 \\ \left| C e^{-\sqrt{i}\frac{\zeta_w}{\sqrt{\zeta_t}}} + D e^{\sqrt{i}\frac{\zeta_w}{\sqrt{\zeta_t}}} \right|, & \alpha \leq 1/6 \end{cases} \tag{2.56}$$

In the original Grant-Madsen model (Grant and Madsen, 1979), the wave boundary layer thickness was taken as a constant multiple of the boundary layer scale, $\delta_w = Al$, where A was taken to be between 1 and 2 corresponding to experimental results by Jonsson (1966). Madsen and Salles (1998) were the first to realize that $A = \zeta_w$ is not a constant but is in fact a function of the relative roughness. Like the new model, they defined the wave boundary layer thickness as the height at which the amplitude of the boundary layer velocity deviates by a certain percentage, ε, from the maximum near-bottom wave velocity. ε is the only parameter in the model which must be chosen, and there are multiple reasonable values to choose from, such as $\varepsilon = 1\%, 2\%$, or 5%. Madsen and Salles defined the boundary layer with $\varepsilon = 5\%$, which gave $\zeta_w = 2$ with the roughness corresponding to Jonsson's experiments, making this choice consistent with the original Grant-Madsen model. As that model yields acceptable results when compared to experiments, we likewise choose this value,

$$\varepsilon = 5\% \tag{2.57}$$

to define the extent of the wave boundary layer for the new three layer model.

2.1.3 Friction factor closure

With the introduction of the wave boundary layer thickness, there are two unknowns remaining in the model formulation, the normalized bottom roughness, $\zeta_0 = z_0/l$, and the maximum combined shear velocity, $u_{*m} = \sqrt{\tau_m/\rho}$. The maximum combined shear stress is the vector sum of the maximum wave shear stress and the current shear stress

$$\vec{\tau}_m = \vec{\tau}_{wm} + \vec{\tau}_c = (\tau_{wm} + \tau_c |\cos \phi_{wc}|, \tau_c |\sin \phi_{wc}|) \tag{2.58}$$

where ϕ_{wc} is the acute angle between the wave and the current directions. The magnitude of the maximum combined shear stress vector is therefore

$$\tau_m = \sqrt{\tau_{wm}^2 + 2\tau_{wm}\tau_c |\cos \phi_{wc}| + \tau_c^2} \tag{2.59}$$

To simplify the expressions, we introduce two new variables relating the shear stresses,

$$C_\mu = \frac{\tau_m}{\tau_{wm}} = \frac{u_{*m}^2}{u_{*wm}^2} \tag{2.60}$$

and

$$\mu = \frac{\tau_c}{\tau_{wm}} = \frac{u_{*c}^2}{u_{*wm}^2} \tag{2.61}$$

Using (2.59), it can be seen that C_μ and μ are related according to

$$C_\mu = \sqrt{1 + 2\mu |\cos \phi_{wc}| + \mu^2} \tag{2.62}$$

Note that the variable α can be written in terms of these variables as

$$\alpha = \frac{u_{*c}}{u_{*m}} = \sqrt{\frac{\mu}{C_\mu}} \tag{2.63}$$

We define the generalized wave friction factor for combined wave and current motion by

34

$$\tau_{wm} = \frac{1}{2}\rho f_{wc} u_{bm}^2 \tag{2.64}$$

Re-arranging (2.64) yields

$$\sqrt{\frac{f_{wc}}{2}} = \sqrt{\frac{\tau_{wm}}{\rho u_{bm}^2}} = \frac{u_{*wm}}{u_{bm}} = \frac{u_{*wm}}{A_{bm}\omega} \tag{2.65}$$

where A_{bm} is the near-bottom wave excursion amplitude, related to u_{bm} by

$$A_{bm} = \frac{u_{bm}}{\omega} \tag{2.66}$$

The definition of ζ_0 in (2.6) can be written in terms of the friction factor using (2.65) and (2.62)

$$\zeta_0 = \frac{z_0}{l} = \frac{z_0}{\kappa u_{*m}/\omega} = \frac{z_0}{\kappa\sqrt{C_\mu}u_{*wm}/\omega} = \frac{z_0}{C_\mu A_{bm}}\frac{\sqrt{C_\mu}}{\kappa\sqrt{f_{cw}/2}} \tag{2.67}$$

For the pure wave case, the relative roughness parameter X is given by

$$X = \frac{A_{bm}}{30z_0} \tag{2.68}$$

or $X = A_{bm}/k_N$ for fully rough turbulent flow conditions. For the combined wave-current case, we define a wave-current relative roughness parameter X_μ

$$X_\mu = C_\mu \frac{A_{bm}}{30z_0} \tag{2.69}$$

Using (2.69) we can re-write (2.67) as

$$\zeta_0 = \frac{1}{30X_\mu}\frac{\sqrt{2}}{\kappa}\sqrt{\frac{C_\mu}{f_{cw}}} \tag{2.70}$$

To fully close the problem, we use the known wave velocity profile near the bed to find another relationship for the friction factor. The maximum shear stress due to the waves is by definition

$$\tau_{wm} = \rho\nu_t \frac{\partial u_w}{\partial z}\bigg|_{z=z_0} \tag{2.71}$$

or, in terms of the normalized deficit velocity,

$$\tau_{wm} = \rho u_{bm} \left(\nu_t \frac{\partial u_d}{\partial z} \right)_{z=z_0} \tag{2.72}$$

Evaluating the eddy viscosity at the bottom using (2.7) and re-writing (2.72) in terms of the non-dimensional vertical scale in (2.6) gives

$$u_{*wm}^2 = \left| \frac{\tau_{wm}}{\rho} \right| = \kappa u_{bm} u_{*m} \zeta_0 \left| \frac{\partial u_d}{\partial \zeta} \right|_{\zeta=\zeta_0} \tag{2.73}$$

Using (2.65) and (2.60), (2.73) becomes

$$\sqrt{\frac{f_{wc}}{2C_\mu}} = \kappa \zeta_0 \left| \frac{\partial u_d}{\partial \zeta} \right|_{\zeta=\zeta_0} \tag{2.74}$$

Using the deficit velocity profile given in (2.44) and the expressions for the derivatives of Kelvin functions given in (2.45), the derivative of the deficit velocity at the bottom can be written in terms of a complex function F_{AB}

$$\left. \frac{\partial u_d}{\partial \zeta} \right|_{\zeta=\zeta_0} = \sqrt{\frac{i}{\zeta_0}} F_{AB}(\zeta_0, \zeta_w, \alpha) \tag{2.75}$$

where F_{AB} is a function of the complex constants A and B, and the parameters ζ_0, ζ_w, and α.

$$F_{AB}(\zeta_0, \zeta_t, \alpha) = A\left[-i\,\mathrm{ker}_1\,2\sqrt{\zeta_0} + \mathrm{kei}_1\,2\sqrt{\zeta_0}\right] + B\left[-i\,\mathrm{ber}_1\,2\sqrt{\zeta_0} + \mathrm{bei}_1\,2\sqrt{\zeta_0}\right] \tag{2.76}$$

Then (2.74) becomes

$$\frac{f_{wc}}{C_\mu} = 2\kappa^2 \zeta_0 [|F_{AB}(\zeta_0, \zeta_w, \alpha)|]^2 \tag{2.77}$$

We can use (2.70) with (2.77) to get an expression for the friction factor in terms of the relative roughness parameter

$$\frac{f_{wc}}{C_\mu} = 2\left[\frac{\kappa}{30} \frac{|F_{AB}(\zeta_0, \zeta_w, \alpha)|^2}{X_\mu}\right]^{2/3} \tag{2.78}$$

Equations (2.78) and (2.70) can be used to develop a modified combined wave friction factor diagram which shows the dependency of the friction factor on the relative roughness.

The phase angle between the shear stress and the near-bottom velocity, φ_τ, will also be of interest, although it is not needed to close the problem. It is given by the argument of the complex near-bottom shear stress

$$\varphi_\tau = \varphi_\tau(\zeta_0) = \arg\{\tau_{wm}\} \tag{2.79}$$

With (2.73) and (2.75), the phase is found to be

$$\varphi_\tau = \frac{\pi}{4} + \arg\{F_{AB}(\zeta_0, \zeta_w, \alpha)\} \tag{2.80}$$

where F_{AB} is again given by (2.76). For a constant eddy viscosity, such as is found in a laminar boundary layer, the phase shift is constant and equal to $\varphi_{\tau,lam} = \pi/4$. For very rough beds (corresponding to small X_μ), the bottom roughness ζ_0 becomes larger than $\zeta_w/6$ and the bottom linear layer of the three layer eddy viscosity profile disappears. The eddy viscosity profile is then constant up to the edge of the top layer, at $\zeta = \zeta_t/\alpha = \zeta_0/\alpha$, so the thickness of this constant layer increases as ζ_0 increases. Thus, as the roughness increases (or X_μ decreases), the eddy viscosity structure becomes constant over more of the depth, the function F_{AB} goes to one, and the phase shift approaches the laminar value, $\varphi_\tau \to \pi/4$.

Extension to random waves

The waves in the model are specified by the amplitude of the near-bottom wave orbital velocity, u_{bm}, the wave radian frequency, ω, and the direction of propagation, ϕ_w. In the case of spectral waves, these quantities are given by those of the representative periodic wave, u_{br}, ω_r, and ϕ_{wr}, respectively, as described in Madsen (1994). The near-bottom velocity amplitude of the representative periodic wave is the root-mean-square (rms) velocity, $u_{b,rms}$, given by the directional near-bottom orbital velocity spectrum, $S_{u_b}(\omega, \theta)$,

$$u_{bm} = u_{b,r} = u_{b,rms} = \sqrt{2 \iint S_{u_b}(\omega, \theta) d\omega d\theta} \tag{2.81}$$

The radian frequency of the representative periodic wave is the mean frequency, given by

$$\omega = \omega_r = \frac{\iint \omega S_{u_b}(\omega, \theta) d\omega d\theta}{\iint S_{u_b}(\omega, \theta) d\omega d\theta} \tag{2.82}$$

and the direction of propagation is given by

$$\tan \phi_w = \tan \phi_{wr} = \frac{\iint S_{u_b}(\omega, \theta) \sin \theta \, d\omega d\theta}{\iint S_{u_b}(\omega, \theta) \cos \theta \, d\omega d\theta} \tag{2.83}$$

2.1.4   Model results and explicit approximations

The five complex constants A, B, C, D, and E, given by equations (2.46), (2.47), (2.49), (2.50), and (2.52), are functions of α, ζ_0, and ζ_w. The wave boundary layer thickness, ζ_w, is a function of α and ζ_0 by (2.56). The zero-velocity level, ζ_0, and the friction factor, f_{cw}, given by (2.70) and (2.77), are functions of C_μ, X_μ, and ζ_w and α through $F_{AB}(\zeta_0, \zeta_w, \alpha)$. Finally, α and C_μ are both functions of the wave shear velocity, which is a function of f_{cw} in (2.65). If the wave characteristics, u_{bm} and ω, the current characteristics, u_{*c} and ϕ_{cw}, and the bottom roughness, k_N, are known, we can solve these equations simultaneously to find all of the parameters and the current velocity profile.

The parameter $\alpha = u_{*c}/u_{*m}$ ranges from $\alpha = 0$, when there is no current and only waves, to $\alpha = 1$, when there is only a current. Solving the model with $\alpha = 0$ is the same as solving for a pure wave boundary layer with a linear-constant eddy viscosity model. Solving for the wave parameters, such as the wave boundary layer thickness, seems illogical for the pure current case, when $\alpha = 1$. However, the wave parameters, f_{cw}/C_μ, ζ_w, and ϕ_τ, only depend on the relative magnitudes of the current and wave through α, so as far as the wave solution is concerned, the magnitude of α simply determines the eddy viscosity structure, and it is irrelevant that in this three layer model taking $\alpha = 1$ corresponds to the pure current case. When $\alpha = 1$ the constant eddy viscosity layer disappears and the eddy viscosity reduces to a simple linear profile scaled by u_{*m}. Therefore, the results from solving this new model with $\alpha = 1$ are equivalent to solving for

38

a pure wave boundary layer with a linear eddy viscosity model, such as was used in the modified Grant-Madsen boundary layer model (Madsen, 1994).

By solving these equations for a range of values of X_μ and α, we can create general diagrams of the friction factor, wave boundary layer thickness, and phase angle. For X_μ values in the range $0.05 < X_\mu < 10^5$ and six values of $\alpha = 0, 0.2, 0.4, 0.6, 0.8, 1$, the relationships for the wave boundary layer thickness, friction factor, and phase angle are shown in Figure 2-4, Figure 2-5, and Figure 2-6, respectively. Also shown for comparison on the figures is the corresponding result for the most recent Madsen model, for which the friction factor and phase are given in Madsen (1994) and the wave boundary layer thickness is given in Madsen and Salles (1998). Both Madsen (1994) and Madsen and Salles (1998) used a linear eddy viscosity model for the wave solution, which is equivalent to the new model with $\alpha = 1$, and Madsen and Salles (1998) defined the boundary layer thickness with $\varepsilon = 5\%$, as in the current model. The results for the boundary layer thickness for the new model with $\alpha = 1$ and Madsen and Salles (1998) are slightly different because Madsen and Salles offset the elevation in the Madsen (1994) model by taking $z \rightarrow z + z_0$.
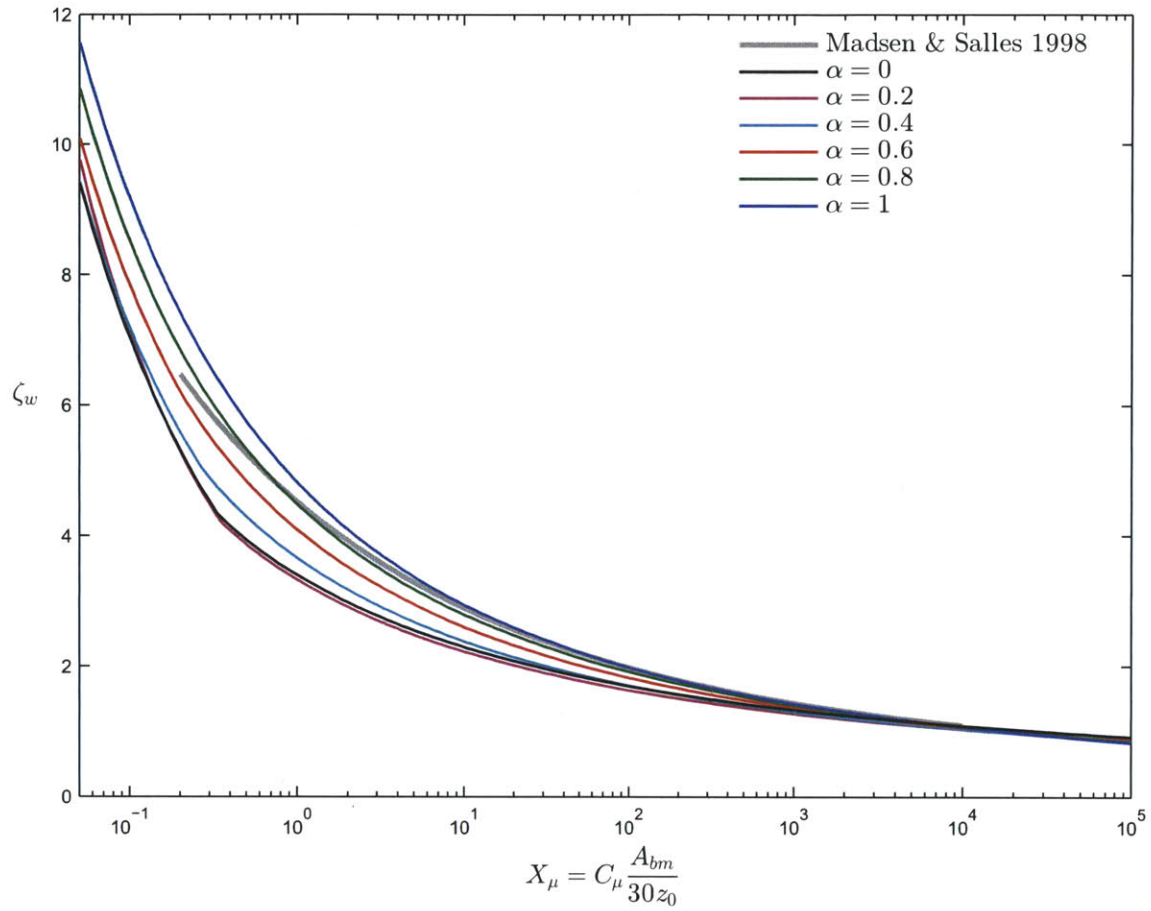
Figure 2-4: Wave boundary layer thickness variation with the relative roughness and α for the new model (colors), and for Madsen and Salles (1998) (gray).
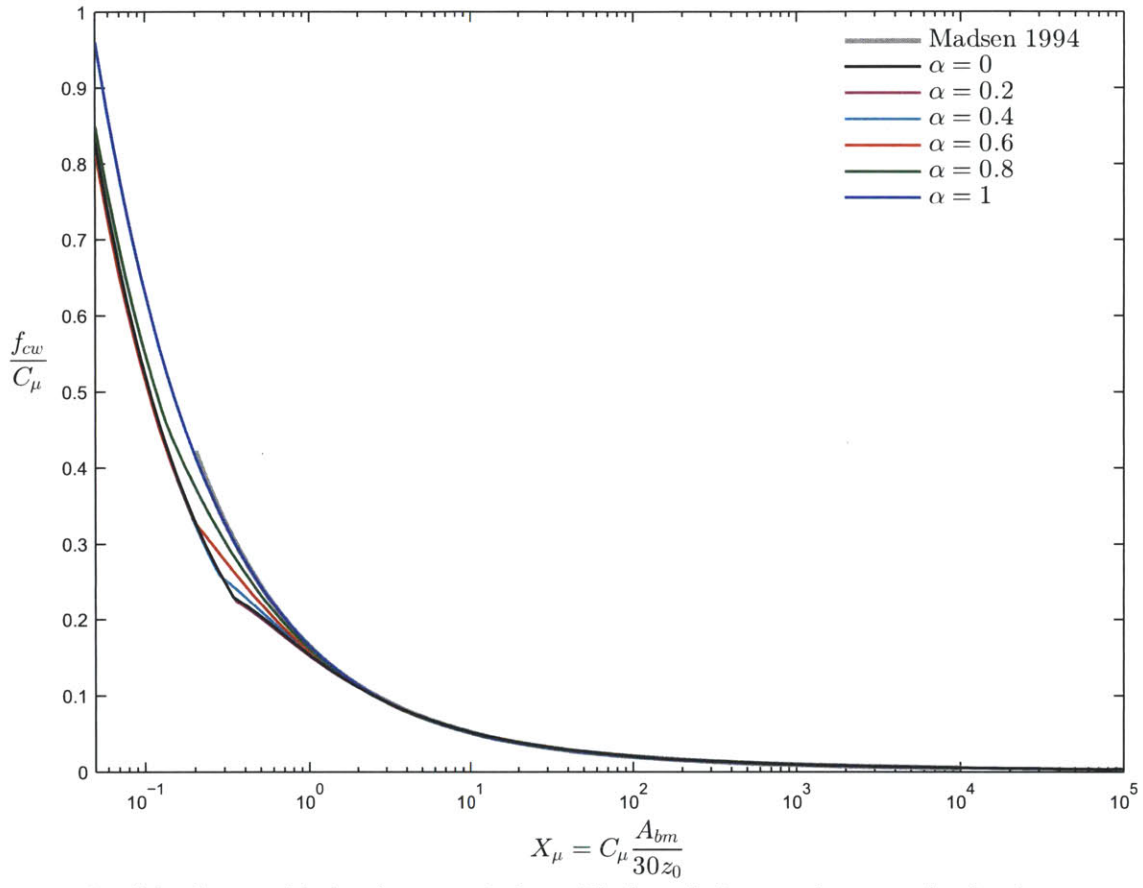
Figure 2-5: Combined wave friction factor variation with the relative roughness and α for the new model (colors), and for Madsen (1994) (gray).
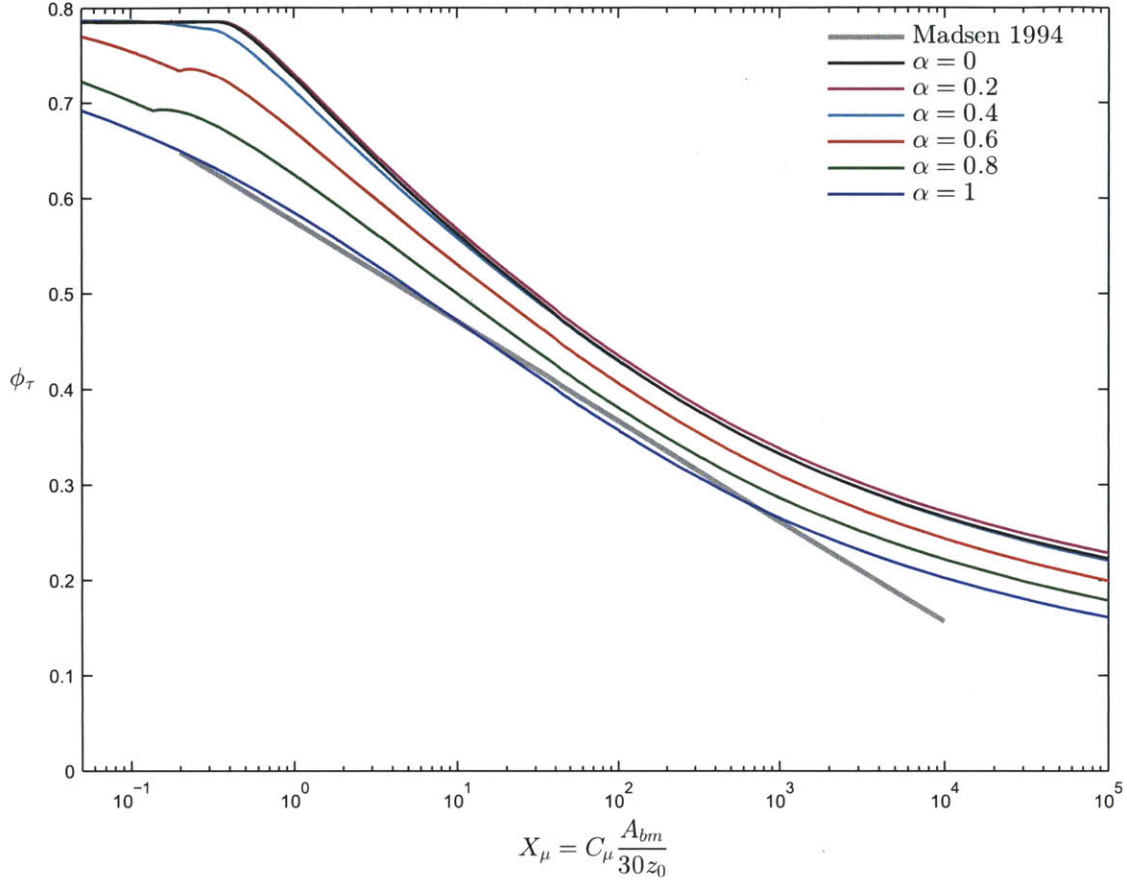
Figure 2-6: Phase angle variation with the relative roughness and α for the new model (colors), and for Madsen (1994) (gray).

The kinks seen in the diagrams near $X_\mu = 0.2$ occur where the model changes from $\zeta_t = \zeta_w/6$ for larger values of X_μ to $\zeta_t = \zeta_0$ for very large roughness, or very small values of X_μ. The value of X_μ where this transition occurs is denoted $X_{\mu,crit}$, and varies with α. An explicit approximation to the relationship between $X_{\mu,crit}$ and α is given by

$$X_{\mu,crit} = \begin{cases} 0.342, & 0 \leq \alpha \leq 0.15 \\ 22.6\alpha^3 - 18.9\alpha^2 + 4.83\alpha - 0.035, & 0.15 < \alpha \leq 0.3 \\ 0.222\alpha^2 - 0.619\alpha + 0.490, & 0.3 < \alpha \leq 1 \end{cases} \qquad (2.84)$$

The critical roughness value given by the explicit fit (2.84) is within 0.5% of the true value of $X_{\mu,crit}$ for all values of α.

To make it easier to solve wave-current problems, explicit approximations have been developed for the friction factor, wave boundary layer thickness, and phase angle, as functions of

X_μ and α, that is, $\zeta_w, f_{cw}/C_\mu, \phi_\tau = f(X_\mu, \alpha)$. For $\alpha = 0$, the pure wave case, the intermediate layer

extends to infinity, so in this limit the three layer model reduces to two layers, with a

corresponding linear-constant eddy viscosity variation. For the pure wave case, explicit

theoretical expressions exist for the condition of very large physical roughness, when $X_\mu <$

$X_{\mu,crit}$, or $\zeta_t = \zeta_0 > \zeta_w/6$, for which the eddy viscosity is constant and takes the value $v_t =$

$\kappa u_{*m} z_0$. For $\alpha = 0$, the critical value of the relative roughness is a function of ε only, and is

approximately $X_{\mu,crit} = 0.342$ for $\varepsilon = 5\%$. Therefore, in the following explicit expressions for the

pure-wave case, (2.85), (2.86), and (2.87), the expression over the range $0.05 \leq X_\mu < X_{\mu,crit} =$

0.342 is exact, whereas the expressions for $X_\mu > X_{\mu,crit} = 0.342$ are fits to the theoretical curves.

The explicit expressions for the wave boundary layer thickness for the pure wave case are

$$\zeta_w(\alpha = 0) = \begin{cases} (30\kappa^2 X_\mu)^{-2/3} - \sqrt{2}\ln\varepsilon\,(30\kappa^2 X_\mu)^{-1/3}, & 0.05 \leq X_\mu \leq 0.342 \\ \exp\{1.36 X_\mu^{-0.148} - 0.135\}, & 0.342 \leq X_\mu < 10 \\ \exp\{2.03 X_\mu^{-0.0849} - 0.845\}, & 10 < X_\mu \leq 10^5 \end{cases} \quad (2.85)$$

The wave friction factor can be approximated for the pure wave case by

$$\frac{f_{cw}}{C_\mu}(\alpha = 0) = \begin{cases} 2\left(\frac{30}{\kappa}X_\mu\right)^{-2/3}, & 0.05 \leq X_\mu \leq 0.342 \\ \exp\{-1.69 X_\mu^{0.344} - 0.473\} + 0.0388, & 0.342 < X_\mu \leq 10 \\ \exp\{5.70 X_\mu^{-0.101} - 7.46\}, & 10 < X_\mu \leq 10^5 \end{cases} \quad (2.86)$$

and the phase shift can be approximated by

$$\varphi_\tau(\alpha = 0) = \begin{cases} \frac{\pi}{4}, & 0.05 \leq X_\mu \leq 0.342 \\ -0.303 X_\mu^{0.260} + 0.00967 X_\mu + 1.02, & 0.342 < X_\mu \leq 10 \\ 0.649 X_\mu^{-0.160} + 0.118, & 10 < X_\mu \leq 10^5 \end{cases} \quad (2.87)$$

Comparisons between the actual computed parameters and the piecewise fits given by (2.85),

(2.86), and (2.87) are shown in Figure 2-7, Figure 2-8, and Figure 2-9. The goodness of these fits

is determined by the mean relative error, MRE, defined as

$$MRE = \text{mean} \left\{ \frac{|Y_{computed} - Y_{fit}|}{Y_{computed}} \right\} \qquad (2.88)$$

where $Y_{computed}$ are the computed values using the full model for a range of X_μ, and Y_{fit} are the values given by the explicit piecewise fit. For the pure-wave case, the mean relative errors of the fits over the range $0.05 \leq X_\mu \leq 10^5$ are $E = 0.11\%$, 0.20%, and 0.19%, respectively, for ζ_w, f_{cw}/C_μ, and φ_τ. Although the fits were developed over this X_μ range, ending at $X_\mu = 10^5$, the error of applying them at $X_\mu = 10^6$ is less than 3% for all the parameters.
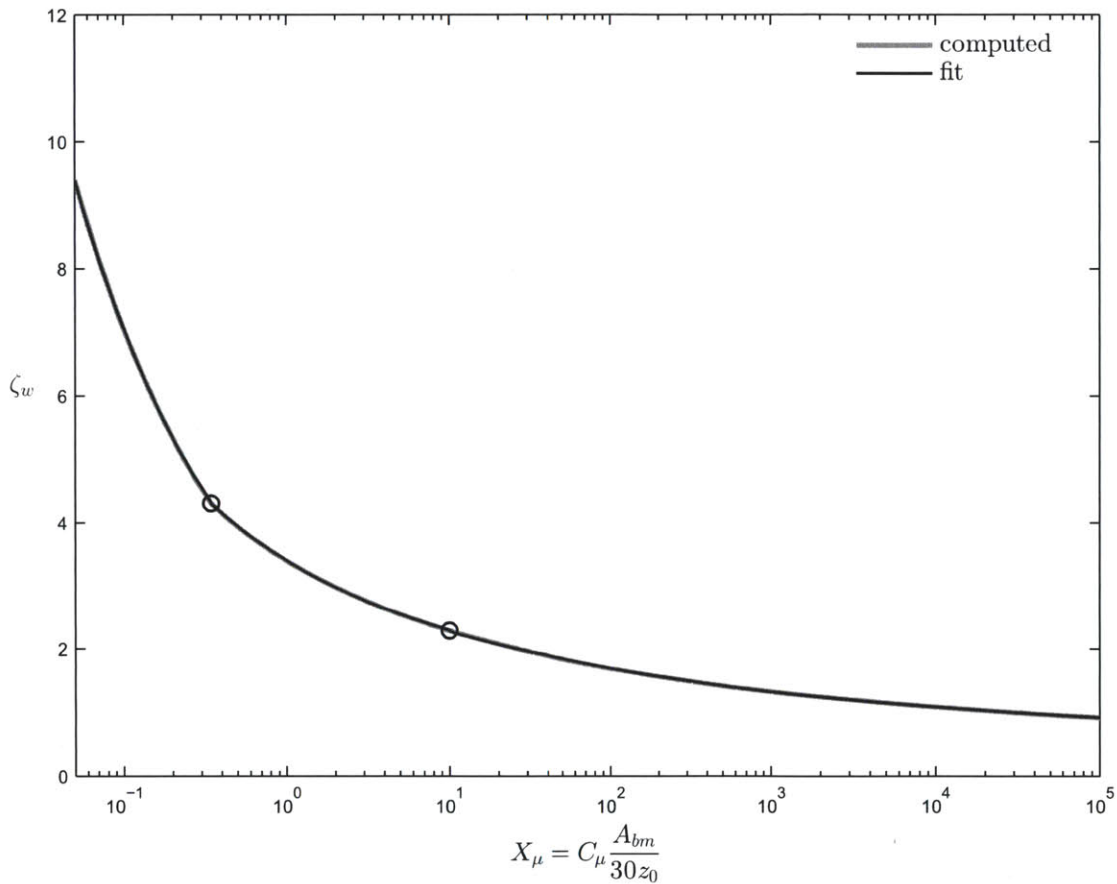
Figure 2-7: Comparison of the computed (gray) and piecewise explicit fit (2.85) (black) for the wave boundary layer thickness for the pure wave case, $\alpha = 0$. The circles indicate boundaries between segments of the piecewise fit.
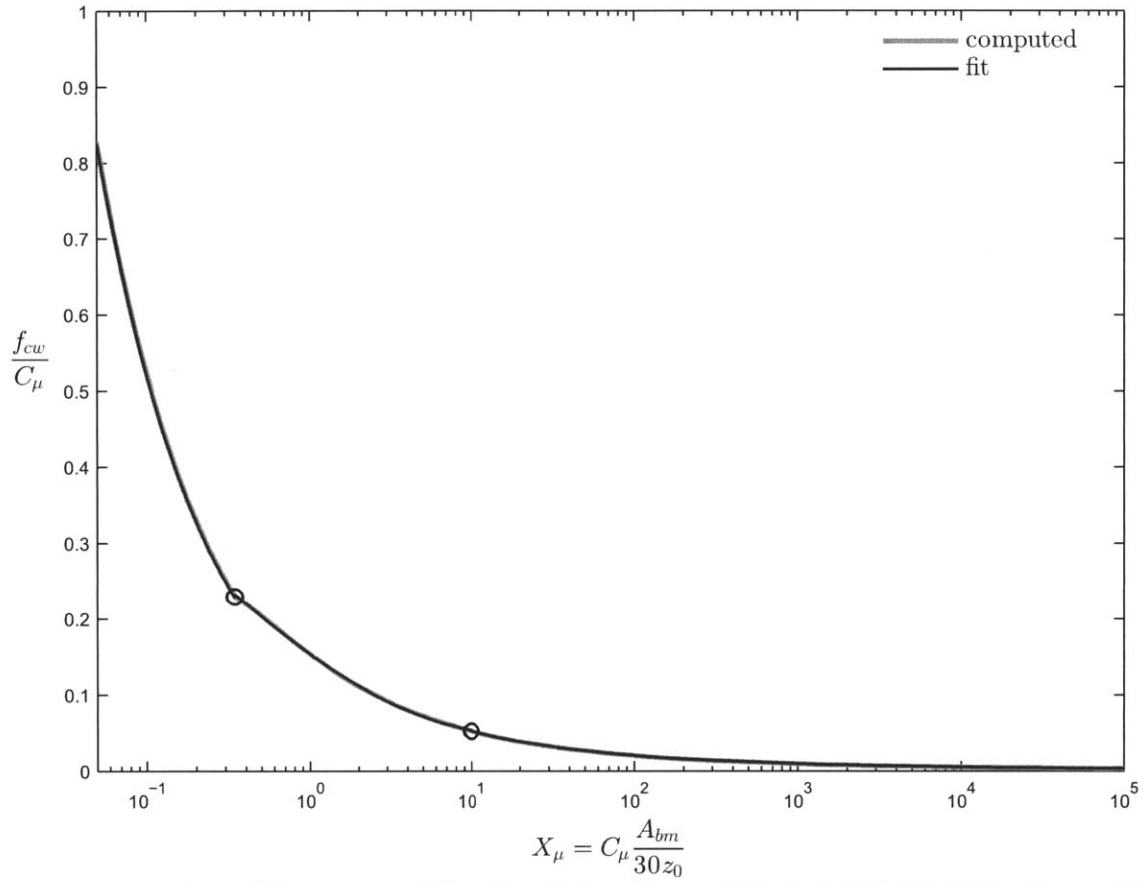
Figure 2-8: Comparison of the computed (gray) and piecewise explicit fit (2.86) (black) for the combined wave friction factor for the pure wave case, $\alpha = 0$. The circles indicate boundaries between segments of the piecewise fit.
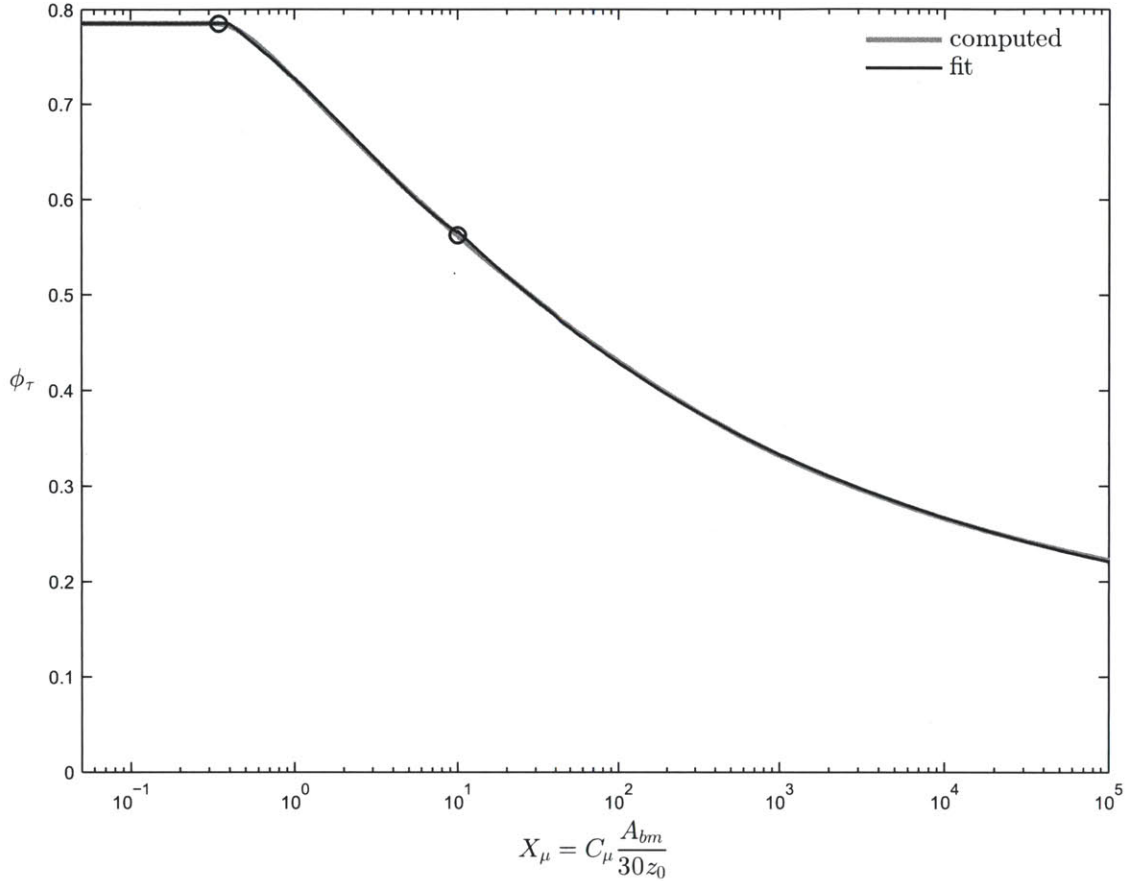
Figure 2-9: Comparison of the computed (gray) and piecewise explicit fit (2.87) (black) for the phase shift for the pure wave case, $\alpha = 0$. The circles indicate boundaries between segments of the piecewise fit.

In general, for any α, explicit approximations to the analytical curves can be given as combinations of exponential and power functions and polynomials with general coefficients, which are functions of α. For small values of α, there is very little difference between the coefficients, and the expressions given in (2.85), (2.86), and (2.87) for $\alpha = 0$ are approximately valid for $\alpha \leq 1/6$. Using the expressions developed for $\alpha = 0$ for values of α up to $\alpha = 1/6$ over the range $0.05 \leq X_\mu \leq 10^5$ gives a maximum relative error of about 2% for f_{cw}/C_μ and φ_τ, and a maximum relative error of about 8% for ζ_w (at the smallest value of X_μ). The value of $\alpha = 1/6$ is a natural dividing line; for $\alpha < 1/6$ the wave boundary layer thickness is found within the intermediate, constant eddy viscosity layer, whereas for $\alpha > 1/6$, the wave boundary layer thickness is located within the top layer. Even though the values of the coefficients for $\alpha \leq 1/6$

46

are already given above for the $\alpha = 0$ case, they are repeated in the equations below so that those equations are valid for all cases. In the expressions that follow, the best-fit coefficients are given for the general functional forms, which gives slightly different results for the $\alpha = 0$ case for very small values of the relative roughness, $X_\mu < X_{\mu,crit}$, compared to the theoretical expressions given in (2.85), (2.86), and (2.87).

For the wave boundary layer thickness, the general functional form for the dependence on X_μ is

$$\zeta_w = \begin{cases} \exp\{a_1 X_\mu{}^{b_1} + c_1\}, & 0.05 \leq X_\mu \leq X_{\mu,crit} \\ \exp\{a_2 X_\mu{}^{b_2} + c_2\}, & X_{\mu,crit} < X_\mu \leq 10 \\ \exp\{a_3 X_\mu{}^{b_3} + c_3\}, & 10 < X_\mu \leq 10^5 \end{cases} \tag{2.89}$$

and the coefficients in (2.89) are given by (2.90)

$$a_1 = \begin{cases} 7.86, & 0 \leq \alpha \leq 1/6 \\ X_{\mu,crit}[155\alpha^4 - 393\alpha^3 + 368\alpha^2 - 133\alpha + 25.0], & 1/6 < \alpha \leq 1 \end{cases}$$

$$b_1 = \begin{cases} -0.0467, & 0 \leq \alpha \leq 1/6 \\ X_{\mu,crit}[3.51\alpha^4 - 9.86 + 8.10\alpha^2 - 3.14\alpha - 0.103], & 1/6 < \alpha \leq 1 \end{cases}$$

$$c_1 = \begin{cases} -6.80, & 0 \leq \alpha \leq 1/6 \\ a_1/[10.4\alpha^4 - 34.4\alpha^3 + 33.0\alpha^2 - 13.6\alpha + 0.256], & 1/6 < \alpha \leq 1 \end{cases}$$

$$a_2 = \begin{cases} 1.36, & 0 \leq \alpha \leq 1/6 \\ 0.455\alpha^3 - 0.233\alpha^2 + 0.564\alpha + 1.29, & 1/6 < \alpha \leq 1 \end{cases}$$

$$b_2 = \begin{cases} -0.148, & 0 \leq \alpha \leq 1/6 \\ a_2/[-8.80\alpha^3 + 4.61\alpha^2 - 4.87\alpha - 8.70], & 1/6 < \alpha \leq 1 \end{cases} \tag{2.90}$$

$$c_2 = \begin{cases} -0.135, & 0 \leq \alpha \leq 1/6 \\ X_{\mu,crit}[-7.98\alpha^4 + 1.96\alpha^3 + 3.60\alpha^2 - 2.92\alpha - 0.108], & 1/6 < \alpha \leq 1 \end{cases}$$

$$a_3 = \begin{cases} 2.03, & 0 \leq \alpha \leq 1/6 \\ -0.381\alpha^3 + 0.795\alpha^2 + 0.831\alpha + 1.92, & 1/6 < \alpha \leq 1 \end{cases}$$

$$b_3 = \begin{cases} -0.0849, & 0 \leq \alpha \leq 1/6 \\ a_3/[9.84\alpha^3 - 25.5\alpha^2 - 8.77\alpha - 22.6], & 1/6 < \alpha \leq 1 \end{cases}$$

$$c_3 = \begin{cases} -0.845, & 0 \leq \alpha \leq 1/6 \\ X_{\mu,crit}[-17.4\alpha^3 + 6.96\alpha^2 - 5.40\alpha - 1.77], & 1/6 < \alpha \leq 1 \end{cases}$$

For the friction factor, the general form is

$$\frac{f_{cw}}{C_\mu} = \begin{cases} a_1 X_\mu{}^{b_1} + c_1, & 0.05 \le X_\mu \le X_{\mu,crit} \\ \exp\{a_2 X_\mu{}^{b_2} + c_2\} + d_2, & X_{\mu,crit} < X_\mu \le 10 \\ \exp\{a_3 X_\mu{}^{b_3} + c_3\}, & 10 < X_\mu \le 10^5 \end{cases} \tag{2.91}$$

and the coefficients for (2.91) are given by (2.92).

$$a_1 = \begin{cases} 0.112, & 0 \le \alpha \le 1/6 \\ X_{\mu,crit}[-0.858\alpha^4 + 4.96\alpha^3 - 4.62\alpha^2 + 1.92\alpha + 0.0722], & 1/6 < \alpha \le 1 \end{cases}$$

$$b_1 = \begin{cases} -2/3, & 0 \le \alpha \le 1/6 \\ X_{\mu,crit}[-16.7\alpha^4 + 37.3\alpha^3 - 34.4\alpha^2 + 9.50\alpha - 2.67], & 1/6 < \alpha \le 1 \end{cases}$$

$$c_1 = \begin{cases} 0, & 0 \le \alpha \le 1/6 \\ X_{\mu,crit}[3.60\alpha^4 - 9.29\alpha^3 + 8.98\alpha^2 - 3.29\alpha + 0.372], & 1/6 < \alpha \le 1 \end{cases}$$

$$a_2 = \begin{cases} -1.69, & 0 \le \alpha \le 1/6 \\ -8.85\alpha^{3.51} - 75.7\alpha^{15.9} - 1.66, & 1/6 < \alpha \le 1 \end{cases}$$

$$b_2 = \begin{cases} 0.344, & 0 \le \alpha \le 1/6 \\ 1.68\alpha^4 - 2.99\alpha^3 + 1.33\alpha^2 - 0.410\alpha + 0.397, & 1/6 < \alpha \le 1 \end{cases}$$

$$c_2 = \begin{cases} -0.473, & 0 \le \alpha \le 1/6 \\ a_2[3.58\alpha^4 - 5.35\alpha^3 + 1.33 - 1.04\alpha + 0.502], & 1/6 < \alpha \le 1 \end{cases} \tag{2.92}$$

$$d_2 = \begin{cases} 0.0388, & 0 \le \alpha \le 1/6 \\ a_2 \cdot 0.01[-4.60\alpha^4 + 2.99\alpha^3 + 4.50\alpha^2 - 0.492\alpha - 2.42], & 1/6 < \alpha \le 1 \end{cases}$$

$$a_3 = \begin{cases} 5.70, & 0 \le \alpha \le 1/6 \\ -0.206\alpha + 5.79, & 1/6 < \alpha \le 1 \end{cases}$$

$$b_3 = \begin{cases} -0.101, & 0 \le \alpha \le 1/6 \\ -0.00812\alpha - 0.0983, & 1/6 < \alpha \le 1 \end{cases}$$

$$c_3 = \begin{cases} -7.46, & 0 \le \alpha \le 1/6 \\ 0.220\alpha - 7.56, & 1/6 < \alpha \le 1 \end{cases}$$

For the phase shift, the general functional form is

$$\varphi_\tau = \begin{cases} \min\left\{a_1 X_\mu{}^2 + b_1 X_\mu + c_1, \dfrac{\pi}{4}\right\}, & 0.05 \le X_\mu \le X_{\mu,crit} \\ a_2 X_\mu{}^{b_2} + c_2 X_\mu + d_2, & X_{\mu,crit} < X_\mu \le 10 \\ a_3 X_\mu{}^{b_3} + c_3, & 10 < X_\mu \le 10^5 \end{cases} \tag{2.93}$$

and the coefficients for (2.93) are given by (2.94).

48

$$a_1 = \begin{cases} 0, & 0 \le \alpha \le 1/6 \\ 79.8\alpha^4 - 237\alpha^3 + 255\alpha^2 - 113\alpha + 17.5, & 1/6 < \alpha \le 1 \end{cases}$$

$$b_1 = \begin{cases} 0, & 0 \le \alpha \le 1/6 \\ X_{\mu,crit}[-159\alpha^4 + 453\alpha^3 - 476\alpha^2 + 205\alpha - 30.9], & 1/6 < \alpha \le 1 \end{cases}$$

$$c_1 = \begin{cases} \pi/4, & 0 \le \alpha \le 1/6 \\ X_{\mu,crit}[20.2\alpha^4 - 47.3\alpha^3 + 45.4\alpha^2 - 14.3\alpha + 3.81], & 1/6 < \alpha \le 1 \end{cases}$$

$$a_2 = \begin{cases} -0.303, & 0 \le \alpha \le 1/6 \\ X_{\mu,crit}^{-1}[0.535\alpha^4 - 1.75\alpha^3 + 1.81\alpha^2 - 0.574\alpha - 0.0466], & 1/6 < \alpha \le 1 \end{cases}$$

$$b_2 = \begin{cases} 0.260, & 0 \le \alpha \le 1/6 \\ X_{\mu,crit}^{-1}[-0.261\alpha^4 + 0.289\alpha^3 + 0.103\alpha^2 - 0.257\alpha + 0.142], & 1/6 < \alpha \le 1 \end{cases}$$

$$\tag{2.94}$$

$$c_2 = \begin{cases} 0.00967, & 0 \le \alpha \le 1/6 \\ 0.01X_{\mu,crit}^{-1}[-1.40\alpha^4 + 2.52\alpha^3 - 1.10\alpha^2 - 0.477\alpha + 0.475], & 1/6 < \alpha \le 1 \end{cases}$$

$$d_2 = \begin{cases} 1.02, & 0 \le \alpha \le 1/6 \\ X_{\mu,crit}^{-1}[-1.30\alpha^4 + 3.82\alpha^3 - 3.61\alpha^2 + 0.869\alpha + 0.301], & 1/6 < \alpha \le 1 \end{cases}$$

$$a_3 = \begin{cases} 0.649, & 0 \le \alpha \le 1/6 \\ c_3[16.5\alpha^4 - 43.3\alpha^3 + 49.3\alpha^2 - 15.4\alpha + 6.67], & 1/6 < \alpha \le 1 \end{cases}$$

$$b_3 = \begin{cases} -0.160, & 0 \le \alpha \le 1/6 \\ c_3[-3.48\alpha^4 + 8.87\alpha^3 - 10.7\alpha^2 + 3.70\alpha - 1.67], & 1/6 < \alpha \le 1 \end{cases}$$

$$c_3 = \begin{cases} 0.118, & 0 \le \alpha \le 1/6 \\ 0.201\exp(-1.52\alpha) - 0.185\exp(-10.1\alpha), & 1/6 < \alpha \le 1 \end{cases}$$

Comparisons of these explicit approximations with the exact theoretical model are shown in Figure 2-10, Figure 2-11, and Figure 2-12, for a range of α values, $\alpha = 0, 0.2, 0.4, 0.6, 0.8, 1$, over the range $0.05 \le X_\mu \le 10^5$. The mean relative error for all three parameters for the six values of α over the full range of X_μ values is less than 1%. The maximum relative error for each of the six values of α is less than 2% for ζ_w and φ_τ. For f_{cw}/C_μ, the maximum relative error is less than about 3% for values of α in the range $\alpha \in [0,0.8]$, but the maximum relative error is about 8% for $\alpha = 1$, and this maximum occurs at $X_\mu = 10$, at the transition between piecewise fits.
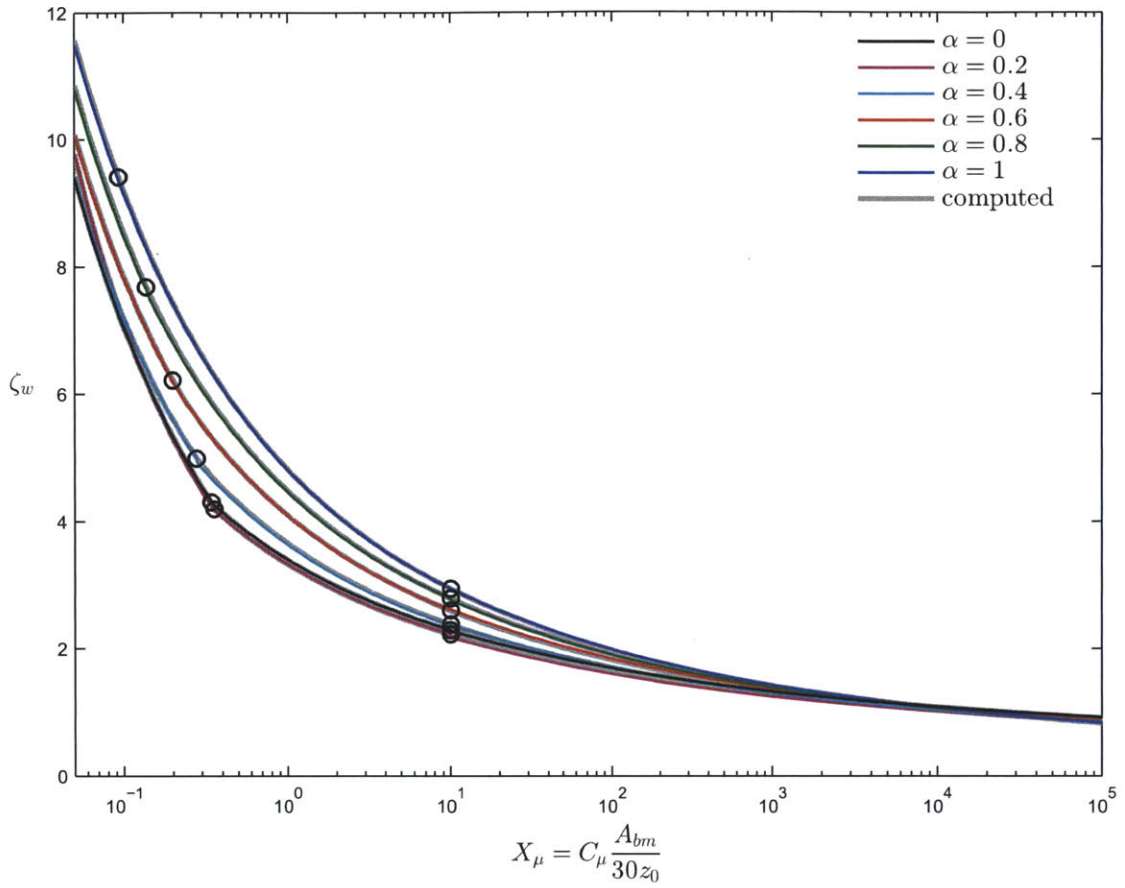
Figure 2-10: Comparison of the computed (gray) and piecewise explicit fits (2.89) and (2.90) (colors) for the wave boundary layer thickness for six values of α. The circles indicate boundaries between segments of the piecewise fits.
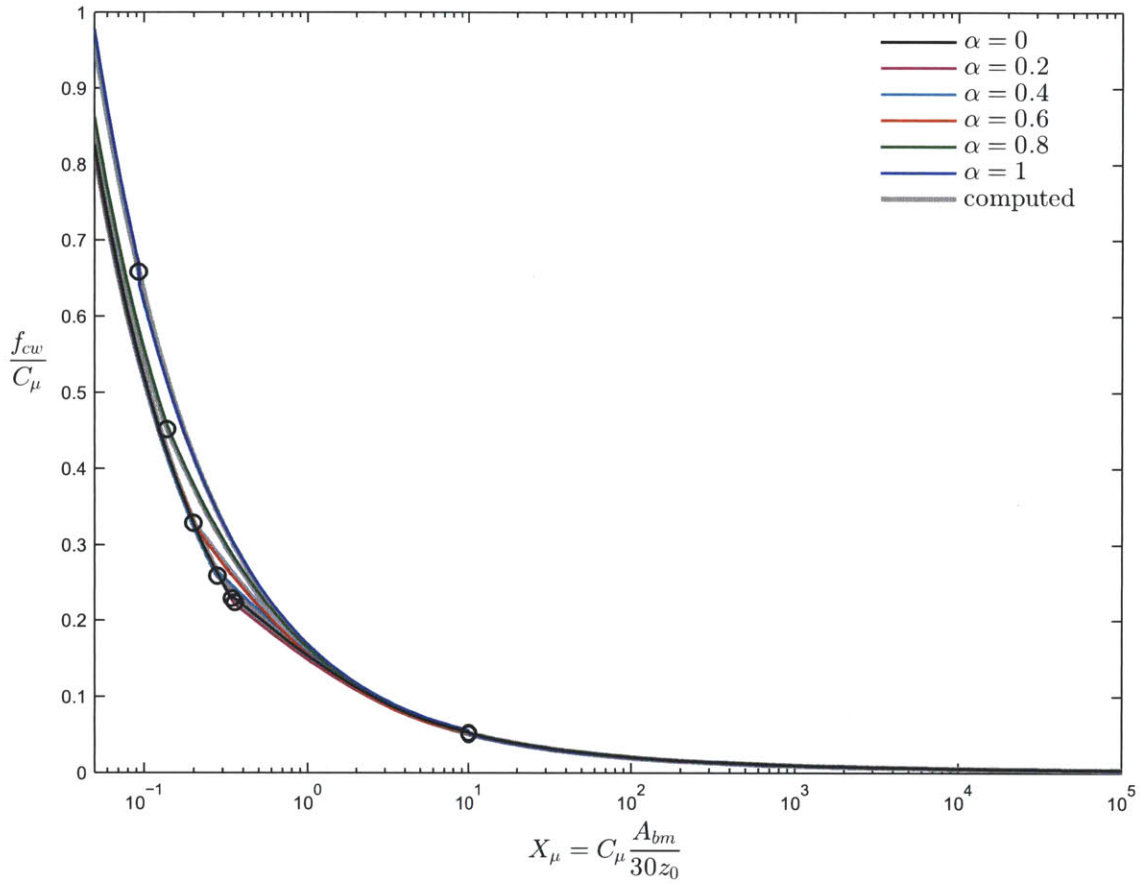
Figure 2-11: Comparison of the computed (gray) and piecewise explicit fits (2.91) and (2.92) (colors) for the combined friction factor for six values of α. The circles indicate boundaries between segments of the piecewise fits.
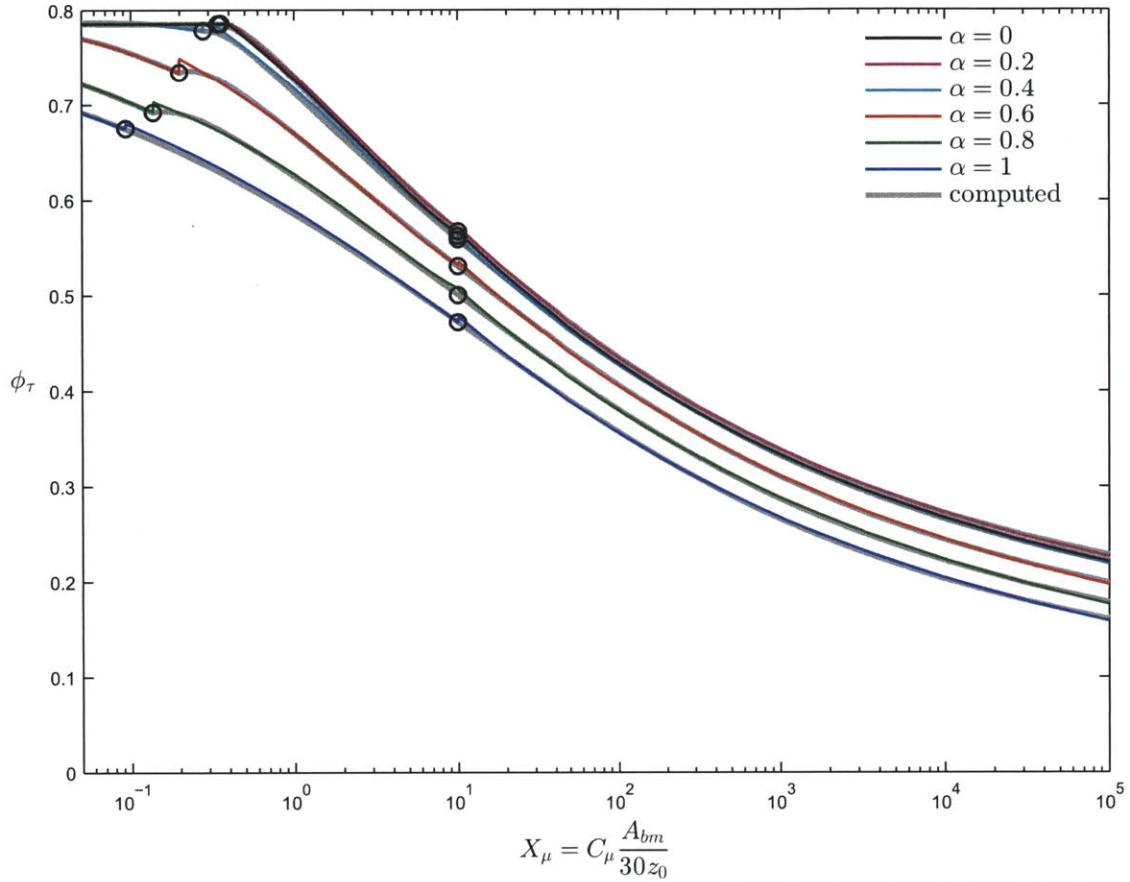
Figure 2-12: Comparison of the computed (gray) and piecewise explicit fits (2.93) and (2.94) (colors) for the phase angle for six values of α. The circles indicate boundaries between segments of the piecewise fits.

2.1.5 Comparison with a simpler, two layer wave model

The major contribution of this new three layer model over the previous Grant-Madsen models is that it accounts for the current throughout the solution of the wave boundary layer problem by consistently using all three layers in both the current and wave problems. The original and modified Grant-Madsen models assumed a two layer bi-linear eddy viscosity profile for the current problem, but only used the bottom linear layer in the wave problem, which allows the current to influence the wave solution only through u_{*m} in the eddy viscosity. Also, the transition level between the two layers was assumed to be a constant multiple of the wave boundary layer scale, l. Madsen and Salles (1998) derived the wave boundary layer thickness as a function of the relative roughness, but still solved the wave problem with a single layer linear

eddy viscosity model, which effectively decouples the current from the waves. This model is more complex than the earlier models in two main ways: it employs a three layer linear-constant-linear eddy viscosity model, and it consistently uses all three layers in the wave problem, which fully accounts for the current. While including the current in the solution of the wave boundary layer is entirely consistent, it greatly increases the complexity of the model, as seen in the expressions for the explicit fits to the model results, which depend on α in addition to X_μ. The added complexity in the new model is not due to using three layers in the current problem, but is a result of using all three layers in the wave problem. Thus, an easy way to simplify this model would be to use only the bottom two layers in the wave problem. Therefore, it is pertinent to know how much benefit is gained by using the more complex, consistent three layer model as opposed to using a simpler model that ignores the current in the wave solution.

If the current is ignored in the wave problem, the top layer of the eddy viscosity structure is removed, and the constant viscosity layer extends to infinity, effectively reducing the model to two layers. This simplified model, which uses all three layers in the current solution but only the bottom two linear-constant layers in the wave solution, will be termed the 'three/two-layered' model, to avoid confusion with the two layer Grant-Madsen models. The three/two-layered model is developed following the same process as the full three layer model, using a two layer eddy viscosity structure with the same transition level, namely, $\delta_t = \max\{\delta_w/6, z_0\}$, and taking the wave boundary layer thickness as the elevation where the amplitude of the velocity in the boundary layer deviates by 5% from the maximum near-bottom orbital velocity. The eddy viscosity structure for the wave problem in the three/two layer model is therefore

$$
\nu_{t,waves} = \begin{cases} \kappa u_{*m} z, & z_0 \leq z < \delta_t \\ \kappa u_{*m} \delta_t, & \delta_t \leq z \end{cases}
\tag{2.95}
$$

As there is no α in the three/two layer model, the effect of the current is completely ignored. Note that when $\alpha = 0$ is used in the three layer model the transition level between the top two layers goes to infinity and the effective eddy viscosity structure is identical to (2.95).

Therefore, the solution of the three layer model with $\alpha = 0$ is exactly equivalent to the three/two layer model solution, where there is no current in the three layer model and the current is simply ignored in the three/two layer model.

Comparing the three and three/two layer models shows the error in neglecting the current in the wave solution. When $\alpha < 1/6$ in the three layer model, the top of the wave boundary layer is found within the middle constant viscosity layer, whereas for $\alpha > 1/6$, the top of the wave boundary layer is found in the top, linear viscosity layer. Therefore, the three/two and three layer models are expected to be very similar for $\alpha < 1/6$, although they are not exactly the same, because the velocity profile in the middle layer of the three layer model is still affected by the presence of the current as it must match the velocity at the transition to the top layer. As α increases, the current begins to dominate over the wave motion, and the difference between the two models is expected to increase.

The ratio of the parameters for the full three layer model to the three/two layer model are shown in Figure 2-13, Figure 2-14, and Figure 2-15 for the wave boundary layer thickness, friction factor, and phase shift, respectively, for a range of α values, $\alpha = 0, 1/6, 0.2, 0.4, 0.6, 0.8, 1$, over the range $0.05 \leq X_\mu \leq 10^5$. Because $\alpha = 1/6$ is the cut-off for the wave boundary layer extending into the top layer, this value of α is included in these figures even though it was not included in the previous figures showing the model results.
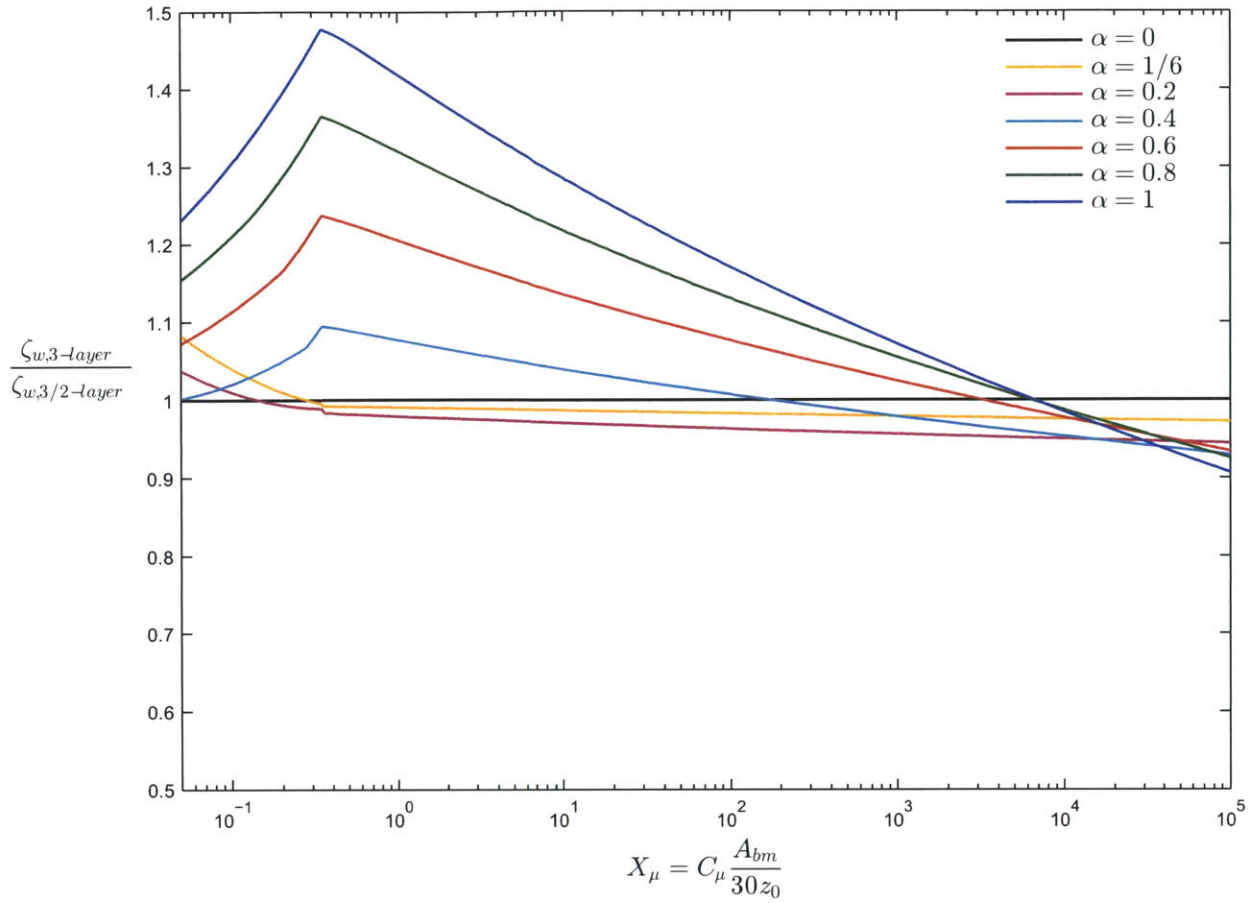
Figure 2-13: Ratio of the scaled wave boundary layer thickness for the three and three/two layer models for seven values of α.

$$\frac{(f_{cw}/C_\mu)_{3\text{-layer}}}{f_{w,3/2\text{-layer}}}$$

$$X_\mu = C_\mu \frac{A_{bm}}{30 z_0}$$

Legend:
- $\alpha = 0$
- $\alpha = 1/6$
- $\alpha = 0.2$
- $\alpha = 0.4$
- $\alpha = 0.6$
- $\alpha = 0.8$
- $\alpha = 1$
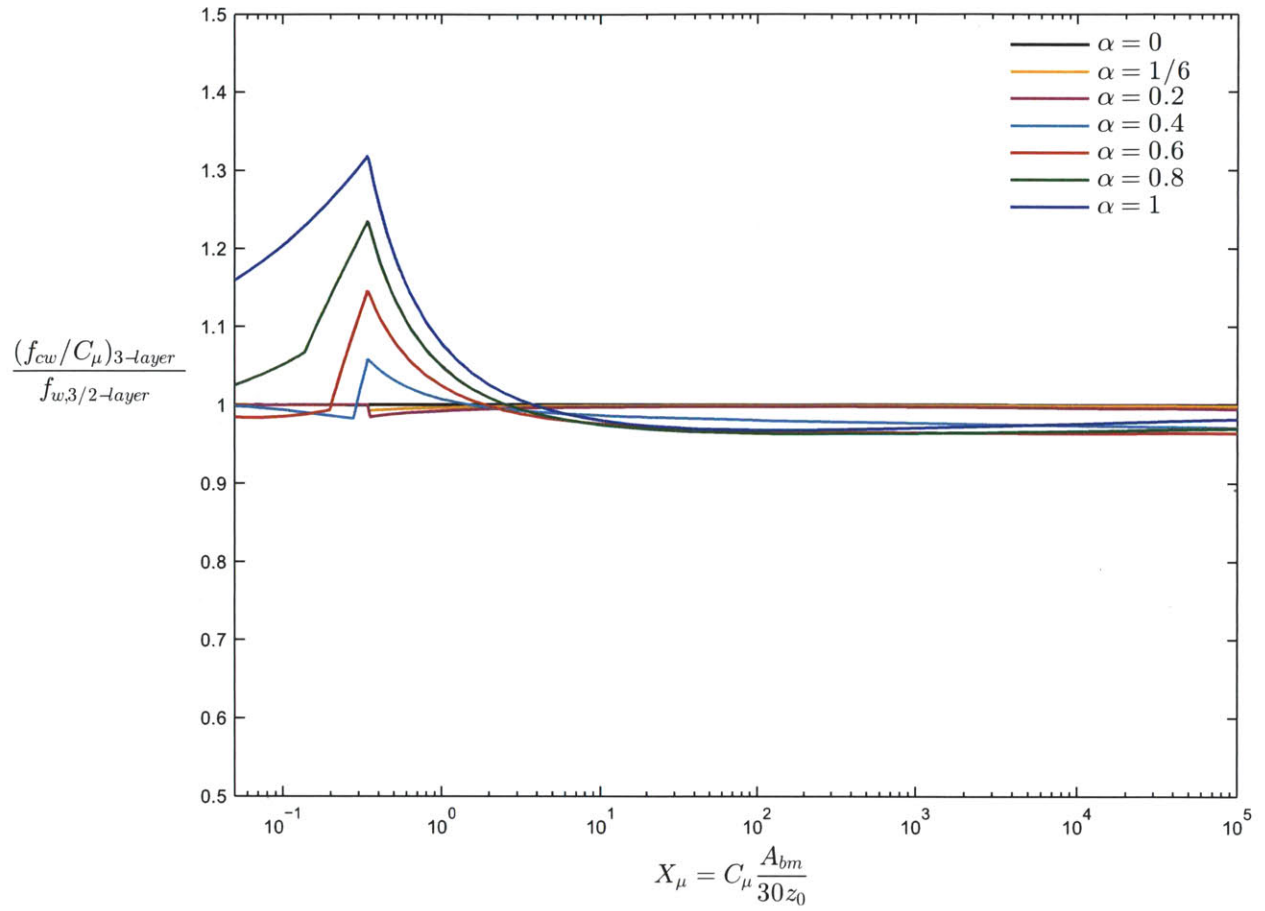
Figure 2-14: Ratio of the combined scaled friction factor for the three layer model and wave friction factor of the three/two layer models for seven values of α.

$$X_\mu = C_\mu \frac{A_{bm}}{30 z_0}$$

Figure 2-15: Ratio of the phase shift for the three and three/two layer models for seven values of α.

For $\alpha = 0$, as expected, the models give identical results, and the ratio is one for all values of X_μ. For $\alpha \leq 0.2$, the ratios for all three parameters show somewhat different trends than for $\alpha > 0.2$, with ratios much closer to one for the small values of α, as expected. The ζ_w and f_{cw} ratios overall converge towards unity as X_μ increases, while the ratio for ϕ_τ diverges. The peaks in the ratios for $\alpha \geq 0.4$ occur at the critical values of the relative roughness for the three/two layer model, $X_{\mu,crit,3/2-layer} = X_{\mu,crit}(\alpha = 0) = 0.342$. The other kinks visible in the f_{cw} and ϕ_τ ratios occur at the critical roughness values of the three layer model, which vary with α.

For $\alpha \leq 0.4$, the three/two and three layer models are within 10% of each other for all three parameters and for the entire range of X_μ values tested, which is very good agreement as

57

far as boundary layer models are concerned. The greatest difference between the models is found for $\alpha = 1$, as would be expected, in which case the three layer model predicts an almost 50% larger boundary layer thickness and a 32% larger friction factor at the value of $X_\mu = X_{\mu,crit}(\alpha = 0) = 0.342$, and a 28% smaller phase shift at the highest value of X_μ considered, $X_\mu = 10^5$. However, even for the extreme case of $\alpha = 1$, the two models are within 30% of each other for all the parameters for all but the smallest values of the inverse relative roughness, $X_\mu \gtrsim 8$. Therefore, if a simpler model is desired, using the three/two layer model can be expected to give acceptable results when the current is small compared to the wave, $\alpha \leq 0.4$, or the relative roughness, k_N/A_{bm}, is not too large (X_μ is not too small).

2.2 Wave-current solution procedure

The combined wave-current boundary layer model developed above can be used to solve for all of the pertinent boundary layer parameters and the current velocity profile given information about the environment, waves, current, and bed. The boundary layer model must be solved iteratively, and a solution procedure for stepping through the equations describing the model is provided here, although other procedures are certainly possible. This wave-current solution procedure is nearly identical to that used in any of the Grant-Madsen type models (e.g., Madsen, 1994), with the difference that the combined wave–current friction factor and the wave boundary layer thickness are computed using the new three layer model.

The environment is specified by the water density and kinematic viscosity, ρ and ν, respectively, the bed is specified by its physical roughness height, k_N, the waves are specified by their near-bottom orbital velocity, u_{bm}, and radian frequency, ω, the current is specified by its direction relative to the wave motion, ϕ_{cw}, and either the current shear velocity, u_{*c}, or a reference current velocity at a reference elevation z_r, $u_{c,r} = u_c(z = z_r)$. Note that because the two layer reduction is used, it appears, from a mathematical standpoint, that the reference

elevation for the current reference velocity must only be higher than the wave-current boundary layer thickness, i.e., $z_r > \delta_{cw}$. However, to accurately reproduce the three layer model results, the reference elevation for the current reference velocity must be within the top layer of the three layer profile, $z_r > \delta_t/\alpha$, which is above δ_{cw}. The equations given below for the wave-current solution procedure are found in some form in section 2.1, but they are repeated here with consecutive equation numbers for clarity.

To begin the iterative calculation procedure, the flow is initially assumed to be fully rough turbulent, in which case the elevation where the velocity disappears is given by

$$z_0 = \frac{k_N}{30} \tag{2.96}$$

and the current is assumed to be negligible compared to the waves, giving

$$\mu = \left(\frac{u_{*c}}{u_{*wm}}\right)^2 = 0 \tag{2.97}$$

Then, the following parameters are calculated with (2.98) through (2.110) until the updated value of μ, μ_{new}, is within an acceptable percentage of the previous value of μ, as given by (2.111).

The wave-current parameters C_μ and α are computed from μ as

$$C_\mu = \sqrt{1 + 2\mu|\cos\phi_{cw}| + \mu^2} \tag{2.98}$$

and

$$\alpha = \sqrt{\frac{\mu}{C_\mu}} \tag{2.99}$$

and the inverse wave-current relative roughness is found from

$$X_\mu = C_\mu X = C_\mu \frac{A_{bm}}{30z_0} \tag{2.100}$$

The combined wave-current friction factor is found from X_μ and α by solving the full wave-current model in section 2.1, or with the explicit approximations: (2.91) and (2.92) for the general case, or (2.86) for the pure-wave approximation if $\alpha = 0$.

59

$$f_{cw}/C_\mu = \mathcal{F}(X_\mu, \alpha) \tag{2.101}$$

The wave and combined maximum shear stresses are found from f_{cw}, u_{bm}, and C_μ,

$$u_{*wm} = \sqrt{\tfrac{1}{2}f_{cw}}\,u_{bm} \tag{2.102}$$

$$u_{*m} = \sqrt{C_\mu}\,u_{*wm} = \sqrt{\tfrac{1}{2}f_{cw}C_\mu}\,u_{bm} \tag{2.103}$$

If u_{*m} is very small and the roughness is not very large, the flow may be smooth turbulent, in which case z_0 would need to be adjusted from the initial rough turbulent assumption of $z_0 = k_N/30$. The value of z_0 can be found for either case as

$$z_0 = \max\left\{\frac{k_N}{30}, \frac{\nu}{9u_{*m}}\right\} \tag{2.104}$$

Procedure variation according to current specification

If the current shear velocity is known a priori, then at this point the new value of μ, μ_{new}, can be calculated with (2.110) below and the calculations above up to (2.104) are repeated until the value of μ converges according to (2.111). In this case, the wave boundary layer thickness and related parameters, given below by (2.105) through (2.108), can be calculated after convergence. If, however, the current is specified by a reference current velocity, $u_{c,r}$, then the wave-current boundary layer thickness is needed to calculate the current shear velocity. In this case, equations (2.105) through (2.108) must be calculated for each iteration; then (2.109) gives the current shear velocity, and μ_{new} is then calculated with (2.110) as before.

The scaled wave boundary layer thickness, $\zeta_w = \delta_w/l$, is found from X_μ and α by solving the full wave-current model in section 2.1, or with the explicit approximations: (2.89) and (2.90) for the general case, or the pure-wave approximation, (2.85), if $\alpha = 0$.

$$\zeta_w = \mathcal{F}(X_\mu, \alpha) \tag{2.105}$$

The wave boundary layer thickness is then found using the wave boundary layer scale, l.

$$\delta_w = \zeta_w l = \zeta_w \frac{\kappa u_{*m}}{\omega} \tag{2.106}$$

The middle, constant viscosity layer begins at the transition level, δ_t, which is equal to 1/6 of the wave boundary layer thickness unless the bed is so rough that the bottom, linearly-varying viscosity layer disappears, and the middle layer extends all the way to z_0.

$$\delta_t = \max\left\{\frac{\delta_w}{6}, z_0\right\} \tag{2.107}$$

The wave-current boundary layer thickness, δ_{cw}, is the elevation at which the top and bottom current velocity profiles intersect, allowing the three layer current velocity profile to be simplified into a two layer profile composed of the original top and bottom layers.

$$\delta_{cw} = \frac{\delta_t}{e} \alpha^{\left(\frac{1}{\alpha-1}\right)} \tag{2.108}$$

If the current is specified by a reference velocity at an elevation in the top layer, $z_r > \delta_t/\alpha$, the current shear stress can be calculated from (Madsen, 2002)

$$u_{*c} = u_{*m} \frac{\ln\left(\frac{z_r}{\delta_{cw}}\right)}{\ln\left(\frac{\delta_{cw}}{z_0}\right)} \left(-\frac{1}{2} + \sqrt{\frac{1}{4} + \frac{\kappa u_{c,r}}{u_{*m}} \frac{\ln\left(\frac{\delta_{cw}}{z_0}\right)}{\ln^2\left(\frac{z_r}{\delta_{cw}}\right)}}\right) \tag{2.109}$$

The new value of μ, μ_{new}, is calculated with u_{*c}, which is either given by (2.109) or known a priori and used to specify the current, and u_{*wm}, given by (2.102),

$$\mu_{new} = \left(\frac{u_{*c}}{u_{*wm}}\right)^2 \tag{2.110}$$

The procedure, (2.98) through (2.110) (skipping (2.105) through (2.109) if the current shear velocity is known, as explained above), is repeated until the value of μ converges. Convergence can be defined, for example, as when the relative error is below a certain tolerance,

$$\text{error} = \frac{|\mu_{new} - \mu|}{\mu_{new}} < \text{tolerance} \tag{2.111}$$

In the model computations in the rest of this thesis, the tolerance was chosen to be 10^{-5}, and the functions in (2.101) and (2.105) were computed by solving the full model, and not the explicit approximations. However, recognizing the magnitude of the error expected in boundary layer problems, using a tolerance of 10^{-2} is sufficient.

The procedure given here solves the conceptual model for the turbulent combined wave-current boundary layer assuming the bed roughness is known. Therefore, to validate the model independent of any formulation for the bed roughness, the roughness of the experiments must be known. Methods for predicting the bed roughness are developed in Chapters 3 and 4.

2.3   Validation of the conceptual model

The three layer model developed in section 2.1 was validated by comparing the results with numerical and experimental results of current velocity profiles in combined wave-current flow in which the bed roughness is known a priori. The model was first tested against combined wave-current numerical results by Davies et al. (1988). Their numerical model uses a $k - \varepsilon$ turbulence closure model and thus does not assume a certain structure for the eddy viscosity. Every test used the same bottom roughness, current shear velocity, and wave period. For the first series, the waves and currents were collinear and three wave velocity amplitudes were used. For the second series, the wave velocity was kept constant and the angle between waves and currents was varied. They also tested a pure current case for comparison. Details of the experimental conditions are given in Table 2-1.

Table 2-1: Conditions for wave-current numerical experiments by Davies et al. (1988)

Series	z_0 (cm)	T (s)	u_{*c} (cm/s)	u_{bm} (cm/s)	ϕ_{cw} (rad)
Current alone	0.5	–	5.8	0	–
1	0.5	8	5.8	$[50, 100, 150]$	0
2	0.5	8	5.8	100	$[0, \pi/4, \pi/2]$

The current profile was calculated for the three tests in each series using the new three layer model with the current specified by the known current shear velocity, u_{*c}, using the

procedure described in section 2.2. Comparisons between the current velocity profiles predicted by their numerical model and with the new three layer model are shown in Figure 2-16 for the series 1 data and Figure 2-17 for the series 2 data.
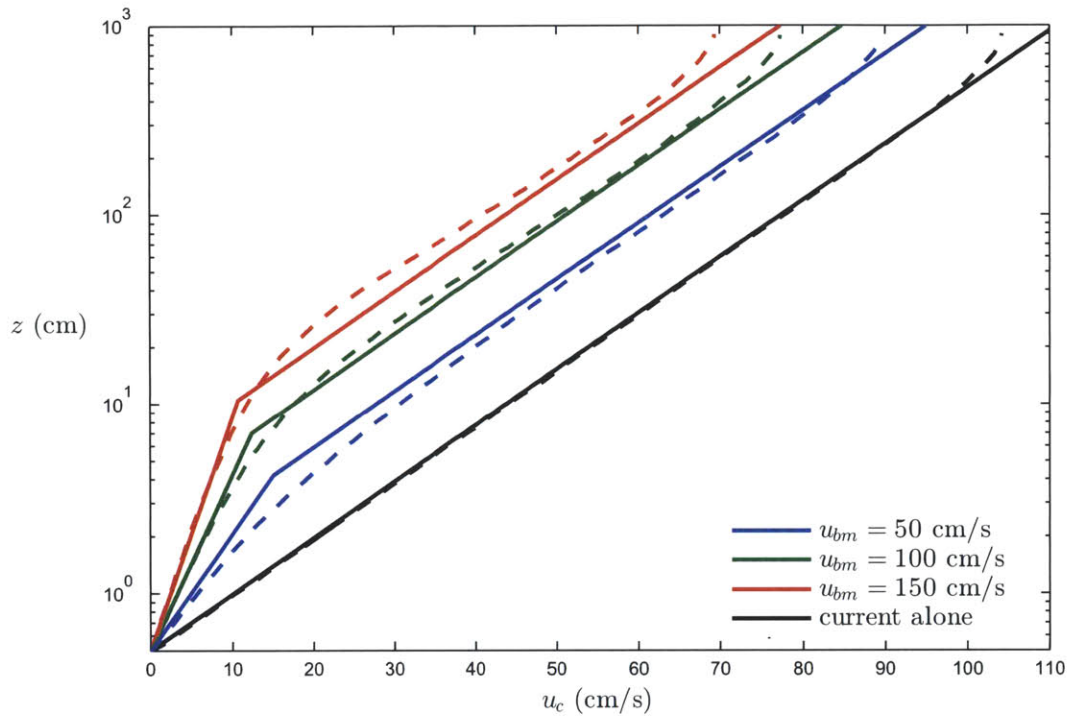
Figure 2-16: Comparison between the velocity profile predicted by the numerical model of Davies et al. (1988) (dashed) and with the new model (solid) for collinear waves and currents of varying wave orbital velocity amplitude.
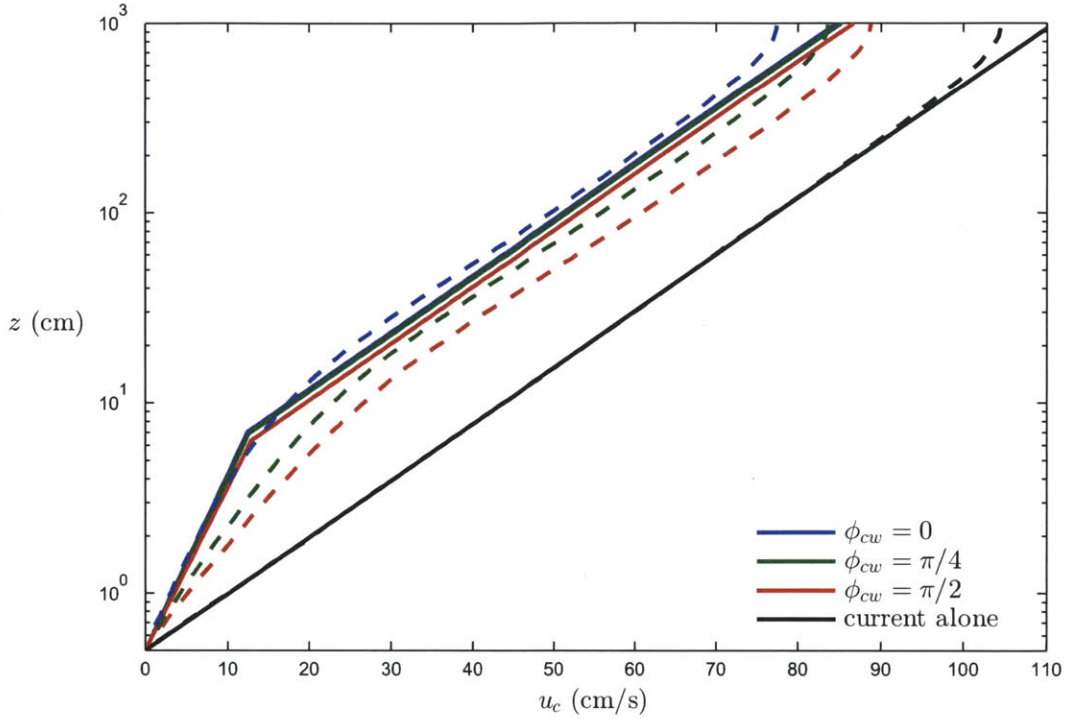
Figure 2-17: Comparison between the velocity profile predicted by the numerical model of Davies et al. (1988) (dashed) and with the new model (solid) for waves and currents at different angles.

The new model reproduces the numerical results well when the waves and currents are collinear (series 1, Figure 2-16), but the results are very different for the non-collinear cases, and the difference increases as the angle between waves and currents increases (series 2, Figure 2-17). Like the Grant-Madsen type wave-current models, the new model is very insensitive to the angle between waves and currents. It is expected that the angle between the waves and current would have a larger effect on the current velocity than is predicted with this model, and its failure to reproduce that effect is a definite weakness of the model. The wave-current angle is only accounted for in the parameter $C_\mu = \tau_m/\tau_{wm} = \sqrt{1 + 2\mu|\cos\phi_{cw}| + \mu^2}$, which is most sensitive to the angle when the current and wave are of similar magnitudes, or when $\mu = \tau_c/\tau_{wm} \approx 1$. When the current and wave shear stresses are of very different magnitudes, for $\mu \ll 1$ or $\mu \gg 1$, C_μ is very insensitive to the wave-current angle. For the series 2 tests, the new model gives $\mu \approx 0.1$ and the predicted maximum combined shear velocity for $\phi_{cw} = \pi/2$ is only

64

8% smaller than it is for $\phi_{cw} = 0$, whereas the numerical model predicts a much larger difference between the two cases.

The model was also tested against combined wave-current experiments conducted by Dohmen-Janssen (1999) in the Delft oscillating water tunnel. There were two cases with collinear sinusoidal waves with a current over fixed beds. The wave and sediment conditions are provided in Table 2-2.

Table 2-2: Conditions for wave-current experiments by Dohmen-Janssen (1999)

Case	d_{50} (mm)	T (s)	u_{bm} (cm/s)	u_r (cm/s)	z_r (cm)
G5	0.21	7.2	95	45	10
G6	0.21	7.2	150	45	10

The bed roughness, $k_N = 30z_0$, was taken to be equal to the roughness derived from the velocity profile for a pure current test, 0.029 cm, which is a factor of about 1.4 larger than the median sediment diameter, d_{50}. The current profile was predicted using the new three layer model with the current specified by the reference velocity, u_r, at an elevation z_r. Comparisons of the measured and predicted current velocity profiles are shown in Figure 2-18.
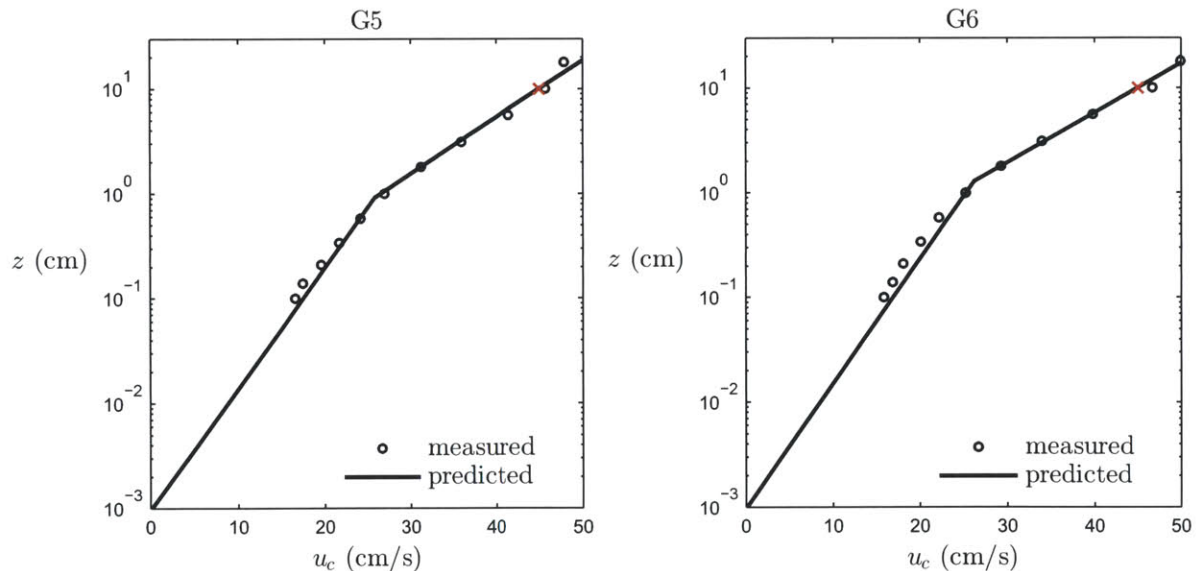
Figure 2-18: Measurements (circles) and predictions (lines) for near-bottom current velocities in Series G reported by Dohmen-Janssen (1999). The red crosses indicate the reference velocity and elevation used to predict the profiles.

The new model shows excellent agreement with the experimental results. The current shear velocity and apparent roughness are accurately predicted by the model, as seen by the close agreement between the predicted and observed velocities in the top portion of the velocity profile. In the bottom portion of the velocity profile the model slightly overpredicts the velocity, which implies that the bottom roughness, found from a pure current test, is slightly too small. Also, in test G6 with the larger wave velocity, the maximum combined shear velocity, u_{*m}, is slightly overpredicted by the model, but the error is well within the acceptable error for boundary layer processes.

2.4 Energy dissipation and friction factors

Although the wave friction factor is the parameter that is directly related to the shear stress, it is difficult to directly measure shear stress in experiments, so a different friction factor is often necessary. When wave attenuation is measured in laboratory experiments, the wave energy dissipation factor, f_e, can be directly calculated from energy conservation considerations. The time-averaged rate of energy dissipation per unit area, $\dot{E}_{diss}$, can be calculated based on linear wave theory from the measured wave height decay over the length of the flume by

$$\dot{E}_{diss} = \rho g c_g a \left| \frac{da}{dx} \right| \tag{2.112}$$

where c_g is the group velocity of the waves and a is the wave amplitude. The rate of energy dissipation is equal to the time-averaged product of the time-varying bottom shear stress, $\tau_b(t)$, and near-bottom wave orbital velocity, $u_b(t)$.

$$\dot{E}_{diss} = \overline{\tau_b(t) u_b(t)} \tag{2.113}$$

For sinusoidal waves, $u_b(t) = u_{bm} f(t) = u_{bm} \cos \omega t$. The temporal variation of the shear stress is typically taken as related to the square of or linearly related to the temporal variation of the instantaneous near-bottom velocity. Thus, for linear waves,

$$\tau_b(t_\tau) = \tau_{bm} \begin{cases} \dfrac{|f(t_\tau)|f(t_\tau)}{f(t_\tau)} = \dfrac{1}{2}\rho f_w u_{bm}^2 \begin{cases} |\cos(\omega t + \varphi_\tau)| \cos(\omega t + \varphi_\tau) \\ \cos(\omega t + \varphi_\tau) \end{cases} \end{cases} \qquad (2.114)$$

where φ_τ is the phase lead of the shear stress with respect to the near-bottom velocity.

Substituting these expressions into (2.113) and simplifying gives

$$\dot{E}_{diss} = \begin{Bmatrix} \dfrac{2}{3\pi} \\ \dfrac{1}{4} \end{Bmatrix} \rho f_w \cos \varphi_\tau \, u_{bm}^3 = \begin{Bmatrix} \dfrac{2}{3\pi} \\ \dfrac{1}{4} \end{Bmatrix} \rho f_e u_{bm}^3 \qquad (2.115)$$

which shows that the energy dissipation factor (also referred to as the energy friction factor) is related to the wave friction factor through a cosine of the phase angle,

$$f_e = f_w \cos \varphi_\tau \qquad (2.116)$$

By simply equating (2.112) and (2.115) the wave energy dissipation factor can be calculated directly from the measured wave height decay.

The new model uses a time-invariant eddy viscosity, thus, to be consistent we must use the simple harmonic time variation of the shear stress, corresponding to the second lines of (2.114) and (2.115) with the final factor of 1/4. Boundary layer models which use more complex, time-varying eddy viscosity models (e.g., Trowbridge and Madsen, 1984 and Gonzalez-Rodriguez, 2009) are able to account for more than just the first harmonic of the shear stress, and therefore these models can justify the use of a more complex temporal variation. However, the difference in the final factors for the two time variations, $2/(3\pi)$ and 1/4, is only about 15%, which is not very significant, so we are not concerned about the need to use the simpler model.

2.5   Comparison of wave friction factor theories

Many wave friction factor theories have been developed under different assumptions for the vertical structure of the eddy viscosity. All of the theories mentioned here were developed for pure waves, as opposed to the new model, which includes the effects of the current from the beginning. To approximately account for the effect of currents on the wave friction factor, the

67

approximate combined wave-current friction factor, f_{wc}, can be related to the pure wave friction factor, f_w, through

$$f_{wc} = C_\mu f_w \tag{2.117}$$

Note that the combined friction factor for the new model is also proportional to C_μ, but as it was developed accounting for the effect of currents, the expression given in (2.117) does not apply in the reverse, that is, for the new model $f_w \neq f_{wc}/C_\mu$, because f_w would depend on α, which includes the effect of the current. Instead, the pure wave friction factor for the new model is found by taking $C_\mu = 1$ and $\alpha = 0$, which gives a linear-constant eddy viscosity variation. Note that for pure waves, the inverse relative roughness is simply $X = A_{bm}/(30z_0)$, whereas with a current it is $X_\mu = C_\mu A_{bm}/(30z_0)$. The earliest friction factor models are only applicable for fully rough turbulent flow, in which case $X = A_{bm}/(30z_0) = A_{bm}/k_N$.

The earliest wave friction factor relationship that is still in wide use today is from Jonsson (1966) and Jonsson and Carlsen (1976). They used a semi-empirical approach to find an implicit relationship between the friction factor and the relative roughness, with the constant determined from velocity profile measurements,

$$\frac{1}{4\sqrt{f_w}} + \log_{10}\left(\frac{1}{4\sqrt{f_w}}\right) = -0.08 + \log_{10} X \tag{2.118}$$

(2.118) was derived by assuming rough turbulent conditions, which is satisfied when X is not too large. Jonsson proposed that f_w be considered constant when X is less than unity. Swart (1976) proposed an explicit approximation for Jonsson's wave friction factor model, including a constant region for small values of X,

$$f_w = \begin{cases} 0.3, & X < \dfrac{1}{0.63} \approx 1.6 \\ \exp\{5.213 X^{-0.194} - 5.977\}, & X \geq \dfrac{1}{0.63} \approx 1.6 \end{cases} \tag{2.119}$$

68

The next notable friction factor relationship was given by Kamphuis (1975), who took the same form as Jonsson (1966), but found different coefficients using his oscillating tray data. No common explicit relationship has been developed for the Kamphuis model.

$$\frac{1}{4\sqrt{f_w}} + \log_{10}\left(\frac{1}{4\sqrt{f_w}}\right) = -0.35 + \frac{4}{3}\log_{10}X \qquad (2.120)$$

Another popular friction factor relationship was given by Grant and Madsen (1986), based on a linear time-invariant eddy viscosity model, with the shear stress evaluated in the limit $z \to 0$.

$$\begin{cases} f_w = 0.23, & X < 1 \\ \frac{1}{4\sqrt{f_w}} + \log_{10}\left(\frac{1}{4\sqrt{f_w}}\right) = -0.17 + 0.24\left(4\sqrt{f_w}\right) + \log_{10}X, & X \geq 1 \end{cases} \qquad (2.121)$$

McLean (cited in Madsen, 1994, p. 392) suggested an explicit approximation to the Grant-Madsen model in a similar explicit form following Swart (1976),

$$f_w = \begin{cases} 0.23, & X < 1 \\ \exp\{5.5X^{-0.12} - 7.02\}, & X \geq 1 \end{cases} \qquad (2.122)$$

The most recent Grant-Madsen type friction factor model is Madsen (1994), which is very similar to the earlier Grant-Madsen models but with the shear stress evaluated at $z = z_0$ rather than as $z \to 0$. Explicit expressions for the friction factor are given by

$$f_w = \begin{cases} \exp\{7.02X^{-0.078} - 8.82\}, & 0.2 \leq X \leq 10^2 \\ \exp\{5.61X^{-0.109} - 7.30\}, & 10^2 < X \leq 10^4 \end{cases} \qquad (2.123)$$

In order to calculate the energy friction factor, Madsen (1994) also gave an explicit approximation for the phase angle, which is

$$\varphi_\tau = \frac{\pi}{60}[11 - 2.0\log_{10}X], \qquad 0.2 \leq X \leq 10^3 \qquad (2.124)$$

A relatively new friction factor model uses a time-varying eddy viscosity model with a linear-constant structure for both the wave and current boundary layers, for a total of four layers (Gonzalez-Rodriguez, 2009). This model also includes an expression for the phase angle. The

friction factor is given in terms of the first and third harmonics, and the maximum friction factor, which is comparable to the friction factors for the time-invariant models, is the maximum of the harmonics. Explicit expressions for the first and third harmonics of the friction factor are given by

$$f_1 = \begin{cases} \exp[17.59X^{-0.05} - 20.42], & 0.02 \le X \le 0.1 \\ \exp[10.17X^{-0.05} - 12.10], & 0.1 < X \le 10^2 \\ \exp[5.84X^{-0.11} - 7.54], & 10^2 < X \le 10^5 \end{cases}$$

$$f_3 = \begin{cases} \exp[-25.78X^{0.04} + 20.92], & 0.02 \le X \le 0.1 \\ \exp[10.23X^{-0.05} - 14.07], & 0.1 < X \le 10^2 \\ \exp[5.60X^{-0.11} - 9.32], & 10^2 < X \le 10^5 \end{cases}$$

(2.125)

Explicit expressions for first and third harmonics of the phase angle are given by

$$\varphi_1 = \begin{cases} 0.660 & 0.02 \le X \le 0.045 \\ -0.168 \log_{10}^2 X - 0.105 \log_{10} X + 0.825, & 0.045 < X \le 2 \\ 0.0202 \log_{10}^2 X - 0.228 \log_{10} X + 0.846, & 2 < X \le 10^5 \end{cases}$$

(2.126)

$$\varphi_3 = -7.19e\text{-}3 \log_{10}^3 X + 0.0967 \log_{10}^2 X - 0.474 \log_{10} X + 1.03$$

The maximum friction factor, which is the most comparable to the steady friction factor models, is found from

$$f_{w,max} = \max[f_1 \cos(\omega t + \varphi_1) + f_3 \cos 3(\omega t + \varphi_3)]$$

(2.127)

and the energy friction factor is found from the first harmonics

$$f_e = f_1 \cos(\varphi_1)$$

(2.128)

The new three layer model developed in section 2.1 is the only one of these models that depends on the current conditions, which it does through the parameter α. Therefore, to compare this new model to these other, pure wave models, the pure wave case of the new model is used, as explained above, with $C_\mu = 1$ and $\alpha = 0$. In that case, the explicit expression for the friction factor is given by (2.86), with $C_\mu = 1$,

$$f_w = \begin{cases} 2\left(\dfrac{30}{\kappa}X\right)^{-2/3}, & 0.05 \le X \le 0.342 \\ \exp\{-1.69X^{0.344} - 0.473\} + 0.0388, & 0.342 < X \le 10 \\ \exp\{5.70X^{-0.101} - 7.46\}, & 10 < X \le 10^5 \end{cases} \qquad (2.129)$$

and the phase shift is given by (2.87),

$$\varphi_\tau = \begin{cases} \dfrac{\pi}{4}, & 0.05 \le X \le 0.342 \\ -0.303X^{0.260} + 0.00967X + 1.02, & 0.342 < X \le 10 \\ 0.649X^{-0.160} + 0.118, & 10 < X \le 10^5 \end{cases} \qquad (2.130)$$

The wave friction factor

To compare the models, the six expressions for the wave friction factor, (2.119), (2.120), (2.122), (2.123), (2.127), and (2.129), are plotted together for a range of X values in Figure 2-19. For those expressions that explicitly give bounds for the relative roughness, the specified bounds are honored.
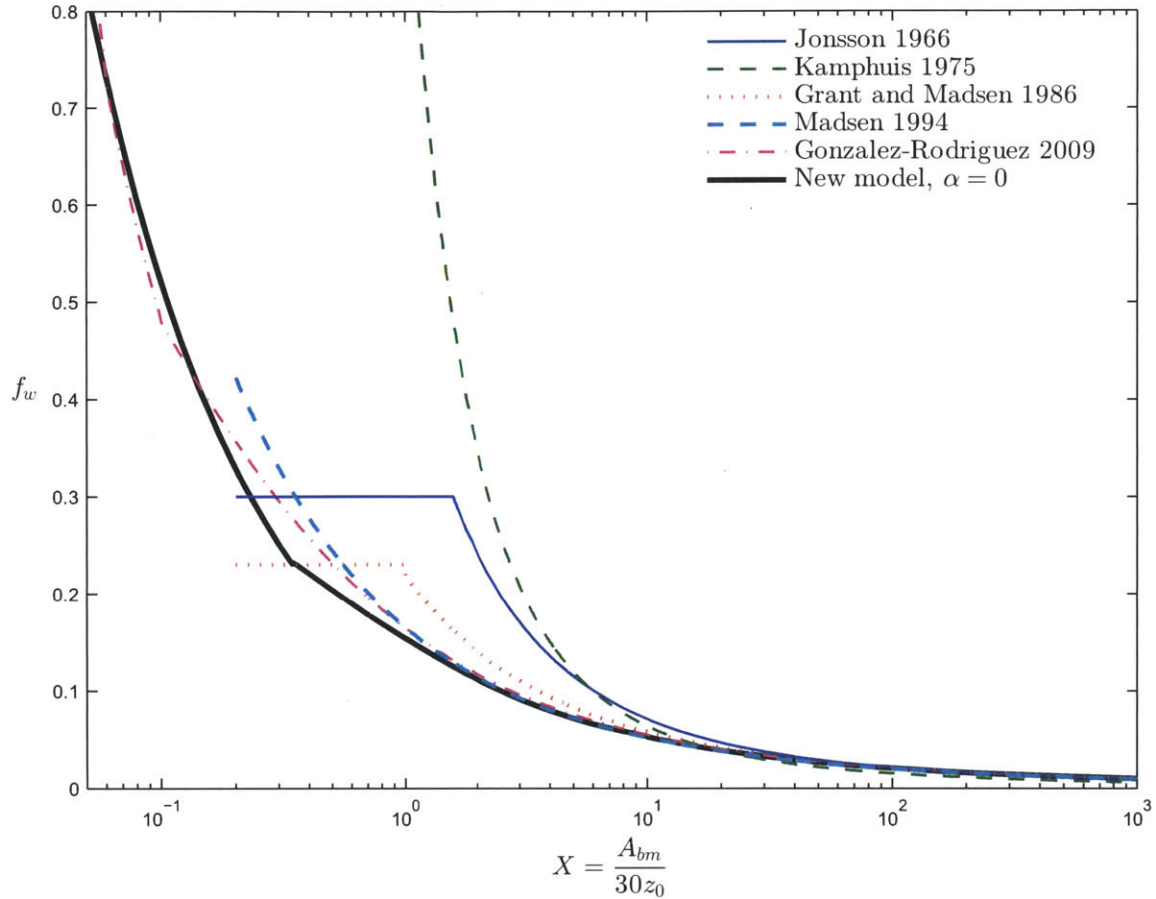
Figure 2-19: Comparison of the wave friction factor for the pure wave case of the new model ($\alpha = 0$, black) and several published models (colors).

It is gratifying that the new model, based on a time-invariant eddy viscosity, shows excellent agreement with the more complex model of Gonzalez-Rodriguez (Figure 2-19), which should be considered the most accurate model presented, as it uses a more elaborate time-varying eddy viscosity formulation. The two models show the largest difference around $X_\mu = 0.3$, but even for very large roughness (small values of X_μ), where the other models diverge, the two models are still quite similar.

The energy friction factor

As derived in section 2.4, the energy friction factor is related to the wave friction factor by a cosine of the phase angle (2.116), which, while sometimes large, is nevertheless often neglected (Wikramanayake and Madsen, 1994). Following this convention, a comparison of the energy

72

friction factors is given in Figure 2-20, where the energy friction factor is given by $f_e = f_w \cos \varphi_\tau$

for the three models that include the phase angle (Madsen, 1994; Gonzalez-Rodriguez, 2009;

and the new model), and for the models that do not, we take $f_e \approx f_w$.
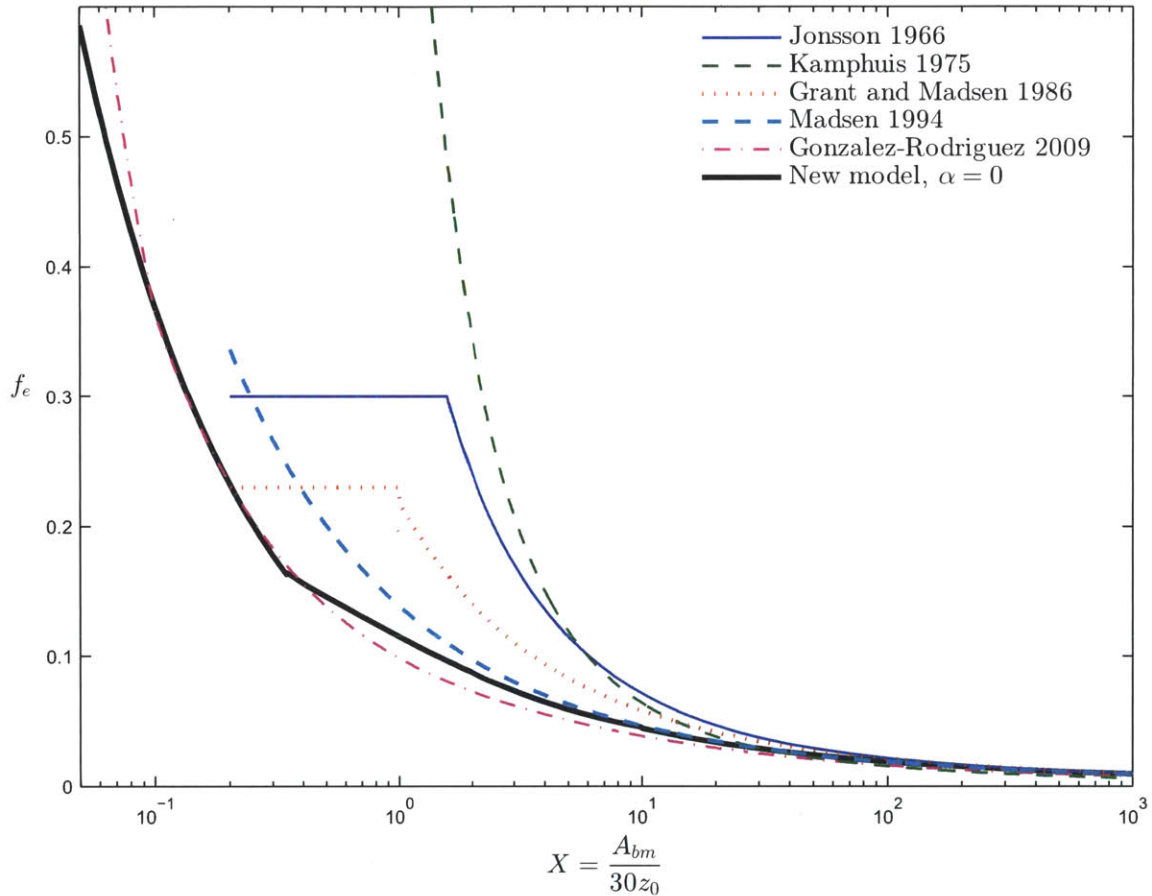
Figure 2-20: Comparison of the energy friction factor for the pure wave case of the new model ($\alpha = 0$, black) and several published models (colors).

As with the wave friction factor, the energy friction factor for the new model is very

similar to that of Gonzalez-Rodriguez, which is a more complicated model based on a time-

varying eddy viscosity (Figure 2-20). The two models do diverge for very small values of X_μ; this

is because while the phase angle in the new model is equal to the laminar value, $\pi/4$, for all

$X < X_{crit} = 0.342$, in Gonzalez-Rodriguez's model the phase angle rises to a value greater than

$\pi/4$ around $X = 0.5$ but then decreases as X continues to decrease.

In general, the friction factor models give quite different results for large roughnesses (small values of $X = A_{bm}/30z_0$, e.g., in the ripple regime), while for very small roughnesses (large values of X) they give nearly identical values (Figure 2-19 and Figure 2-20). At the small X end, for example, for a typical friction factor value of 0.2, the Madsen (1994) and Jonsson (1966) models give $X = 0.5$ and 2.5, respectively, a factor of 5 difference.

Chapter 3

Movable bed regimes

The theoretical combined wave-current model developed in Chapter 2 can be used to predict the near-bed hydrodynamics given an estimate of the bed roughness. In this chapter we discuss the coupling between flows and movable beds and how the hydrodynamic roughness, the quantity of interest, depends on what regime the movable bed is in. We then characterize the possible flow regimes for a movable bed: the lower flat-bed regime, the ripple regime, and the sheet flow or upper flat-bed regime. We give a sample of published relationships for the non-dimensional ripple height, and present new relationships, developed with laboratory data with periodic and random waves, for the ripple height and the energy friction factor for both the ripple and sheet flow regimes.

3.1   Coupling between flows and movable beds

Predicting hydrodynamic quantities in boundary layer flows requires estimates of the bed roughness, $k_N = 30z_0$ for fully rough turbulent flow, which depends on both the bottom sediment properties and the flow. The strength of the flow near the bed determines whether the sediment below it is stationary, saltating, or being transported in a thin layer near the bed. The bed configuration, in turn, whether it is flat, rippled, or in motion, affects the flow above it by determining the physical roughness of the bottom. In this way, the flow and the bed are intrinsically coupled, and one cannot apply the boundary layer model developed in Chapter 2 without quantifying the bed regime.

3.1.1 Relevant non-dimensional parameters

The two physically important non-dimensional parameters in this boundary layer problem are the Shields parameter, ψ, and the shear Reynolds number, Re_*. The Shields parameter is the ratio of the driving to the stabilizing forces acting on the sediment,

$$\psi = \frac{\tau_{bm}}{(s-1)\rho g d} = \frac{u_*^2}{(s-1)g d} \tag{3.1}$$

where s is the ratio of sediment to water density ($s = 2.65$ for quartz in freshwater), and $d = d_{50}$ is the median sediment grain diameter. The shear Reynolds number quantifies the turbulence in the flow, and is given by

$$Re_* = \frac{u_* d}{\nu} \tag{3.2}$$

where ν is the kinematic viscosity of the fluid. The shear Reynolds number determines whether the flow over a flat-bed is smooth or rough turbulent.

The Shields parameter and the shear Reynolds number are the two physically important parameters in the problem, and both of them are required, as the Shields parameter is an average quantity, and the shear Reynolds number gives information on the instantaneous turbulence statistics. However, to avoid having two parameters that both include the shear velocity, they can be combined into a new parameter, which then replaces Re_* as one of the two parameters. By equating the shear velocity, ψ and Re_* can be combined into the fluid-sediment parameter, S_*, which accounts for the influence of sediment and fluid characteristics

$$S_* = \frac{1}{4}\frac{Re_*}{\sqrt{\psi}} = \frac{d\sqrt{(s-1)g d}}{4\nu} \tag{3.3}$$

With S_* thus defined, instead of specifying ψ and Re_*, the problem is specified with ψ and S_*.

The Shields parameter can also be written in terms of the wave friction factor, f_w, as

$$\psi = \frac{\frac{1}{2}f_w u_{bm}^2}{(s-1)g d} \tag{3.4}$$

where f_w is a function of A_{bm}/k_N for fully rough turbulent flow. Because the Shields parameter includes the total shear stress, which is commonly not known a priori, finding it typically requires iteration. An alternative form of the Shields parameter is the skin-friction Shields parameter, ψ', which is only dependent on the skin-friction shear stress, $\tau'_{bm} = \rho u'^2_*$, and thus does not require iteration to calculate. It can also be written in terms of the skin-friction friction factor, $f'_w = f_w(k'_N = d)$, which is the wave friction factor for a flat sand bed,

$$\psi' = \frac{\frac{1}{2}f'_w u^2_{bm}}{(s-1)gd} \tag{3.5}$$

Note that if the bed is flat, the total Shields parameter is equivalent to the skin-friction Shields parameter.

Other researchers have used a variety of non-dimensional parameters to describe the flow. One of the most popular, M, termed the mobility number, is closely related to the skin-friction Shields parameter

$$M = \frac{u^2_{bm}}{(s-1)gd} = \frac{\psi'}{\frac{1}{2}f'_w} \tag{3.6}$$

Ratios of these parameters have also been used; the most common are termed Y and Z:

$$Y = \frac{M}{S_*} \tag{3.7}$$

and

$$Z = \frac{\psi'}{S_*} \tag{3.8}$$

It seems that many researchers prefer to use the mobility number, M, rather than the skin-friction Shields parameter, ψ', because the latter requires a friction factor, which makes this parameter dependent on which friction factor theory is used to calculate the friction factor. While this may be a legitimate concern for the total Shields parameter, ψ, the skin-friction Shields parameter is very insensitive to the chosen friction factor theory. This is because the

skin-friction Shields parameter uses the skin-friction wave friction factor, f'_w, based on the relative roughness defined by the sediment diameter, $X' = A_{bm}/d$, which is very large in most cases. From the comparison of the different friction factor theories, Figure 2-19, it can be seen that the different models give nearly identical results for very large relative roughness values. In fact, over the typical range of A_{bm}/d values the models differ on average by less than 10% (excluding the anomalous Kamphuis 1975 model). It follows that the skin-friction Shields parameter is fairly insensitive to the choice of friction factor theory, and as it is more physically based than M, since it includes the shear stress and not just the velocity, it should be the preferred parameter choice.

The relationships developed here will all be given in terms of the skin-friction Shields parameter, ψ', and the fluid-sediment parameter, S_*. The other parameters are necessary to compare previously published relationships.

3.1.2   Characterizing random waves

For random waves, the corresponding wave parameters are found by defining a representative periodic wave that is equivalent to the random wave spectrum. As mentioned in section 2.1, Madsen (1994) showed that the near-bottom orbital velocity amplitude of the representative periodic wave is the root-mean-square (rms) velocity amplitude, $u_{b,rms}$ (2.81), and the representative radian frequency, ω_r, is the mean frequency of the spectrum. Another option for the representative near-bottom velocity for random waves is the significant velocity. Assuming the random waves are Rayleigh distributed, the significant velocity is a factor of $\sqrt{2}$ larger than the rms velocity,

$$u_{b,sig} = \sqrt{2}u_{b,rms} \tag{3.9}$$

The skin-friction Shields parameter for random waves can be defined using either the rms or significant near-bottom velocity, which are a factor of 2 different,

$$\psi'_{random,rms} = \psi'(u_{b,rms}) = \psi'_{rms} \qquad (3.10)$$

or

$$\psi'_{random,sig} = \psi'(u_{b,sig} = \sqrt{2}u_{b,rms}) = 2\psi'_{rms} \qquad (3.11)$$

In addition to the significant near-bottom velocity, some researchers use an even larger representative velocity, the 1/10 velocity, given by the mean of the highest 1/10 near-bottom velocities from a random-wave time series. It follows that the 1/10 skin-friction Shields parameter, $\psi'_{1/10}$ is defined using the 1/10 velocity. Assuming the waves are Rayleigh distributed, the 1/10 velocity is related to the rms velocity by $u_{b,1/10} = 1.8u_{b,rms}$.

Note that we choose to always define the wave excursion amplitude using the rms value, $A_{bm,random} = A_{b,rms}$, so that the skin-friction wave friction factor $f'_w = f'_w(X' = A_{bm}/d = A_{b,rms}/d)$, does not change for the various Shields parameter definitions, even when a larger near-bottom velocity is used. Therefore, the only difference between the rms, significant, and 1/10 Shields parameter is in the formulation of the near-bottom orbital velocity. As the skin-friction relative roughness uses the sediment diameter as the roughness, the value of $X' = A_{bm}/d$ is very large, and is well in the region where the friction factor varies very little with the relative roughness, and as a result the skin-friction friction factor is very insensitive to the definition of A_{bm}. Therefore, while our definition of ψ'_{sig} or $\psi'_{1/10}$ is inconsistent, since it uses the significant or 1/10 near-bottom velocity but the rms excursion amplitude to find f'_w, because f'_w is very insensitive to the definition of A_{bm} this inconsistency is justified as it greatly simplifies conversions between the different Shields parameters.

The other non-dimensional parameters, such as M, can be defined in the same way for random waves, that is, M_{rms}, M_{sig}, and $M_{1/10}$ can be calculated from the rms, significant, and 1/10 near-bottom velocities.

3.2   Initiation of motion

When there is little or no wave motion above a sediment bed, the sediment is unaffected by the flow, and as a result the bed will remain in its initial state, typically a fairly flat bed. Once the flow reaches a certain magnitude, the sediment particles will begin to be transported by the flow in short jumps. The relationship between the flow and sediment characteristics when movement is initiated was originally given by Shields (1936) in what is now known as the Shields curve. The original Shields curve plotted the Shields parameter, ψ, against the shear Reynolds number, Re_*, which requires iteration to solve as u_* appears on both axes. To circumvent this difficulty, a modified Shields diagram has been developed which relates the skin-friction Shields parameter, ψ', to the fluid-sediment parameter, S_* (Madsen and Grant, 1976). When the skin-friction Shields parameter is above the critical value, ψ'_{crit}, predicted by initiation of motion using the modified Shields diagram, then it can be expected that the sediment is in motion.

The Shields diagram was developed for steady flow, but it has been shown that it is also successful when used for oscillatory flows (Madsen and Grant, 1976). To apply the modified Shields diagram to random waves, the significant near-bottom velocity should be used, as shown in Madsen (2002).

3.3   Ripple regime: ripple geometry

For certain flow conditions, once the sediment is in motion, as predicted by the modified Shields diagram, a regular pattern of bedforms develops on the bed. Under oscillatory flow, these relatively small bedforms are symmetric ripples. When the bed is flat, the hydrodynamic roughness, given by the equivalent Nikuradse sand grain roughness, k_N, scales with the sediment size. Extending this principle to the ripple regime, it follows that when ripples cover the bottom, the bed roughness can be expected to scale with the ripple dimensions. Therefore, the common method of predicting bed roughness begins by predicting the ripple height, η, and

possibly the length, λ, and then takes the roughness as a function of these dimensions. It has been shown (e.g., Wikramanayake and Madsen, 1994; Styles and Glenn, 2002) that the roughness may be well represented as a constant multiple of the ripple height, i.e., $k_N = \gamma\eta$, where γ denotes the proportionality constant. Therefore, for simplicity we will concentrate on predicting the ripple height, and not attempt to predict the ripple length, as the small potential improvement in the roughness prediction does not warrant the large increase in complexity.

With the correlation between ripple dimensions and roughness in mind, much research has been conducted on predicting ripple dimensions in oscillatory flow. There is an abundance of published empirical relationships from laboratory and field measurements relating ripple dimensions to flow and sediment characteristics (e.g., Miller and Komar, 1980; Nielsen, 1981; Grant and Madsen, 1982; Kos'yan, 1988; Wikramanayake and Madsen, 1994; Wiberg and Harris, 1994; Mogridge et al., 1994; Faraci and Foti, 2002; Williams et al., 2004; O'Donoghue et al., 2006). Each formula performs well against the data used in its formulation, as expected, but generally much less successfully under reasonably different conditions. Thus, instead of choosing a published relationship, we developed our own from all of the laboratory data we could acquire, including most of the data used to develop those expressions.

3.3.1   Available data

In order to develop a relationship for ripple geometry, data must be simultaneously collected on both the ripple dimensions and the flow conditions, and the sediment properties must be known. Many studies have been conducted in which ripple geometry is measured in the laboratory, most often under periodic waves, but with a fraction under random waves. In the past, most of these tests were conducted in small-scale laboratory facilities, but recently data from a number of full-scale experiments have been made available (e.g., van der Werf et al., 2009). A sizable number of researchers have also conducted studies on ripple geometry in the field, but unfortunately much of the data are not tabulated but presented solely in figures, which

makes it much harder to use. Therefore, the field data sets presented here are limited to those which included tables of data points. As we restricted ourselves to wave alone data from the laboratory, we also excluded field data for which a substantial current was present. The following tables summarize the datasets used to compare the published relationships and to develop our own relationship for the ripple height. The periodic and random laboratory wave data sets are listed in Table 3-1, the wave alone field data sets are in Table 3-2, and finally a summary of all three types of data is found in Table 3-3.

Table 3-1: Periodic and random wave laboratory datasets used in ripple height analysis

Set	Source	d (mm)	No. data points Periodic waves	No. data points Random waves
1	Inman & Bowen (1963)	0.20	2	
2	Kennedy & Falcon (1965)	0.095	4	
		0.32	6	
3	Carstens et al. (1969)	0.19	6	
		0.297	17	
		0.585	19	
4	Mogridge & Kamphuis (1972)	0.36	21	
		0.36	50	
5	Lofquist (1978)	0.18	6	
		0.55	23	
6	Nielsen (1979)	0.082	24	
		0.17	10	
		0.36	10	
7	Miller & Komar (1980)	0.178	4	
8	Lambie (1984)	0.09	19	
		0.15	27	
9	Lofquist (1986)	0.18	20	
		0.55	62	
10	Rosengaus (1987)	0.20	9	8
11	Sato (1987)	0.18	16	7
12	Sato (1988)	0.18	12	21
		0.56	10	13
13	Mathisen (1989)	0.12	6	9
		0.20	–	3
14	Ribberink & Al-Salem (1994), Series B	0.21	10	10
15	Rankin & Hires (2000)	0.23	10	
16	O'Donoghue & Clubb (2001)	0.18	2	
		0.26	3	
		0.34	28	
		0.44	2	
17	Faraci & Foti (2002)	0.25	27	11
18	Thorne et al. (2002 & 2003)	0.33	11	4
19	O'Donoghue et al. (2006)	0.22	5	8
		0.35	10	2
		0.44	5	5
20	Van der Werf et al. (2007)	0.44	14	

Table 3-2: Wave alone field datasets used in ripple height analysis

Set	Source	d (mm)	No. data points
1	Inman (1957)	0.081–0.635	54
2	Nielsen (1984)	0.11 –0.62	38
3	Dingler (1974)	0.128–0.616	24
4	Hanes et al. (2001)	0.121–1.662	201

Table 3-3: Overview of laboratory and field datasets used in ripple height analysis

Flow type	No. datasets	No. data points	No. diameters	d (mm)	ψ', ψ'_{rms}	η/A_{bm}
Periodic waves	20	510	25	0.082–0.585	0.02 –1.47	0–0.50
Random waves	8	101	10	0.12 –0.56	0.05 –1.02	0–0.36
Field	4	317	92	0.081–1.662	0.0022–1.30	0–0.616

3.3.2 Published relationships

The current consensus among researchers is that the ripple height is scaled by the maximum near-bottom semi-excursion amplitude, A_{bm}. For sinusoidal wave motion, as stated above, $A_{bm} = u_{bm}/\omega$. For random waves, the near-bottom semi-excursion amplitude is defined with the rms near-bottom velocity, $A_{bm,random} = u_{b,rms}/\omega_r$. Some authors use the significant near-bottom velocity to represent random waves in every parameter, and therefore they define the excursion amplitude as $A_{b,sig} = u_{b,sig}/\omega$, and their relationships for the ripple height reflect this choice. However, we choose to use the rms velocity to define the excursion amplitude, even when the other parameters use the significant velocity. The difference in the definitions of A_{bm} should have a negligible effect on the calculated skin-friction Shields parameter, as explained above, but it would have a much larger effect on the non-dimensional ripple height, η/A_{bm}.

A number of the most widely used ripple height relationships are given in Table 3-4 for those developed with laboratory data, and Table 3-5 for relationships developed with field data. A few other relationships of historical note are those by Kos'yan (1988), Mogridge et al. (1994), and Wiberg and Harris (1994). These relationships are not included in the table as they scale the ripple height by the sediment diameter, neglect the effect of the near-bottom orbital velocity (Kos'yan, 1988 and Mogridge et al., 1994), and/or are implicit (Wiberg and Harris, 1994). Also, some researchers have developed expressions for just the ripple length (Traykovski et al., 1999); as we will assume the roughness scales with the ripple height we are not interested in predicting the length and have therefore not included those expressions.

Table 3-4: A sample of ripple height relationships for waves in the laboratory

Authors	Wave type	Relationship
Nielsen (1981)	Periodic	$\dfrac{\eta}{A_{bm}} = 0.275 - 0.022\sqrt{M}$
Grant & Madsen (1982)	Periodic	$\dfrac{\eta}{A_{bm}} = \begin{cases} 0.22(\psi'/\psi_{cr})^{-0.16}, & \psi'/\psi_{cr} < 1.8S_*^{0.6} \\ 0.48S_*^{0.6}(\psi'/\psi_{cr})^{-1.5}, & \psi'/\psi_{cr} > 1.8S_*^{0.6} \end{cases}$
van Rijn (1989)	Random: sig	$\dfrac{\eta}{A_{bm}} = \begin{cases} 0.22, & M \leq 10 \\ 2.8 \times 10^{-13}(250 - M)^5, & M > 10 \end{cases}$
Wikramanayake & Madsen (1990)	Periodic	$\dfrac{\eta}{A_{bm}} = 0.27 - 0.33\psi'^{0.5}$
Faraci & Foti (2002)	Periodic Random: sig	$\dfrac{\eta}{A_{bm}} = \left[1 - \frac{0.022}{0.275}\sqrt{M}\right] \exp\left\{-0.0076\left(\frac{u_{bm}A_{bm}}{\nu}\right)^{0.5} - 0.168\right\}$
Williams et al. (2004)	Periodic Random: sig	$\dfrac{\eta}{A_{bm}} = \exp\{-0.315 \ln^2 M + 2.12 \ln M - 6.09\}$
O'Donoghue et al. (2006)	Periodic Random: 1/10	$\dfrac{\eta}{A_{bm}} = [0.275 - 0.022M^{0.42}] \cdot \begin{cases} 0.55, & d \leq 0.22 \text{ mm} \\ 1, & d > 0.30 \text{ mm} \end{cases}$

Table 3-5: A sample of ripple height relationships for waves alone in the field

Authors	Wave type	Relationship
Nielsen (1981)	Field: sig	$\dfrac{\eta}{A_{bm}} = \begin{cases} 0.275 - 0.022\sqrt{M}, & M < 10 \\ 21M^{-1.85}, & M > 10 \end{cases}$
Wikramanayake & Madsen (1994)	Field: rms	$\dfrac{\eta}{A_{bm}} = \begin{cases} 0.27Y^{-0.5}, & Y < 3 \\ 0.47Y^{-1.0}, & Y > 3 \end{cases}$
Wikramanayake & Madsen (1990)	Field: rms	$\dfrac{\eta}{A_{bm}} = \begin{cases} 0.018Z^{-0.5}, & Z < 0.012 \\ 0.0007Z^{-1.23}, & Z > 0.012 \end{cases}$
Grasmeijer & Kleinhans (2004)	Field: sig	$\dfrac{\eta}{A_{bm}} = \begin{cases} 0.275 - 0.022\sqrt{M}, & M < 10 \\ 2M^{-1}, & M > 10 \end{cases}$

In Table 3-4 and Table 3-5, the second column specifies the wave type (either periodic, random, or both) used in the development of the relationship; for those with random waves, the random wave specification, either the root mean square (rms), significant (sig), or 1/10 near-bottom velocity (1/10), is also listed. Some of the researchers have found relationships that are applicable to both periodic and random waves if the random waves are represented by a larger near-bottom velocity; in this case, both waves types are listed in the table, along with the specification for random waves. Since most of the random wave relationships are also valid for periodic waves, in the relationship expressions the parameters are given in general form, e.g., M,

and it is understood that when applied to random waves the appropriate near-bottom velocity definition would be used, e.g., $M = M_{sig}$.

Of the eleven relationships given in Table 3-4 and Table 3-5, seven of the previously published relationships use the mobility parameter, M, to predict the non-dimensional ripple height, and the other four use four different parameters or combinations of parameters. To compare the methods which use the M parameter, all of the data given in section 3.3.1 (Table 3-3) is plotted with all seven relationships in Figure 3-1. Out of the five relationships which use the M parameter for random waves in the laboratory or the field, four use the significant near-bottom velocity to define M and A_{bm}, and the last, O'Donoghue et al. (2006), uses the 1/10 near-bottom velocity for M and the rms velocity for A_{bm}. Because most of the relationships were developed with the significant velocity, the random wave data is plotted with M_{sig} and $\eta/A_{b,sig}$ to compare the relationships. The relationships by O'Donoghue et al. were developed using larger definitions of M and η/A_{bm} for random waves than are used to plot the random wave data. When these effects are combined, the O'Donoghue et al. relationships give erroneously large estimates for the ripple height for the random wave data. It is not possible to change the expressions to account for the different random wave definitions because the expressions would no longer be correct for the periodic wave data, since the same expressions are used for both periodic and random waves. We have therefore plotted the O'Donoghue et al. relationships as they are given, with the caveat that we realize they will appear to overpredict the random wave data.
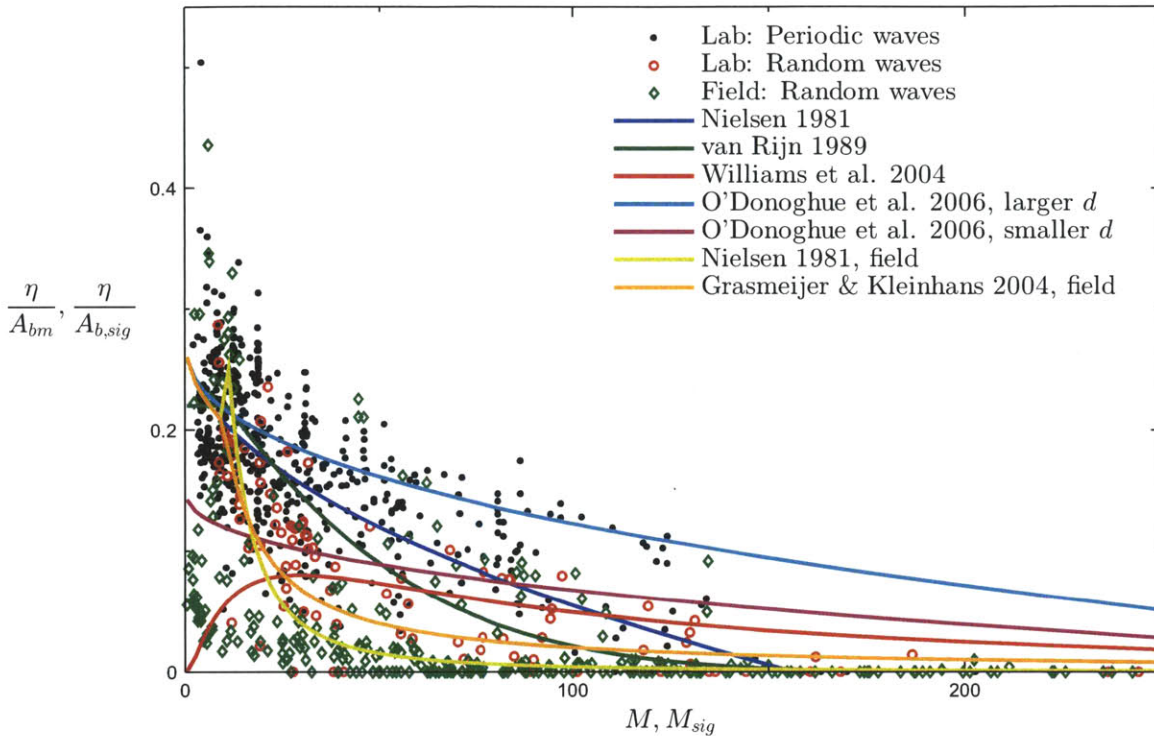
Figure 3-1: Comparison of the seven ripple height relationships in Table 3-4 and Table 3-5 using the M parameter (lines), along with laboratory data under periodic (black dots) and random waves (red circles), and field data (green diamonds), from Table 3-1 and Table 3-2.

Although these relationships were developed using some of the same datasets, they give vastly different predictions for the ripple height over the whole M range. Also, no one relationship performs much better than all of the others. Because these relationships are so different, none is clearly superior, and all of them were developed using less data than we currently have access to, we decided to continue in the tradition of ripple dimension research and develop our own expression.

3.3.3 New ripple height relationship for laboratory data

Several movable bed data sets from laboratory experiments with periodic and random waves (Table 3-1) were analyzed to obtain a relationship for the ripple height. While many other authors choose to use the mobility parameter M to predict the non-dimensional ripple height,

η/A_{bm}, we choose to use the skin-friction Shields parameter, ψ', which correlates the ripple height data at least as well as M and is physically based.

Some researchers (e.g., Nielsen, 1981, Wikramanayake and Madsen, 1994, Kos'yan, 1988) have concluded that ripple geometry relationships developed from laboratory data are not applicable to field conditions. However, these conclusions were formed after comparing field data to relatively small scale laboratory data under periodic waves and did not consider laboratory data on random waves. Now that we have access to large scale laboratory tests under periodic and random waves, we can test whether the field data are truly different and unable to be consolidated with the laboratory data. The data on ripple heights from the laboratory and field are compared in Figure 3-2. The rms near-bottom velocity was used for the random wave data from the laboratory and field for both the skin-friction Shields parameter and the non-dimensional ripple height.
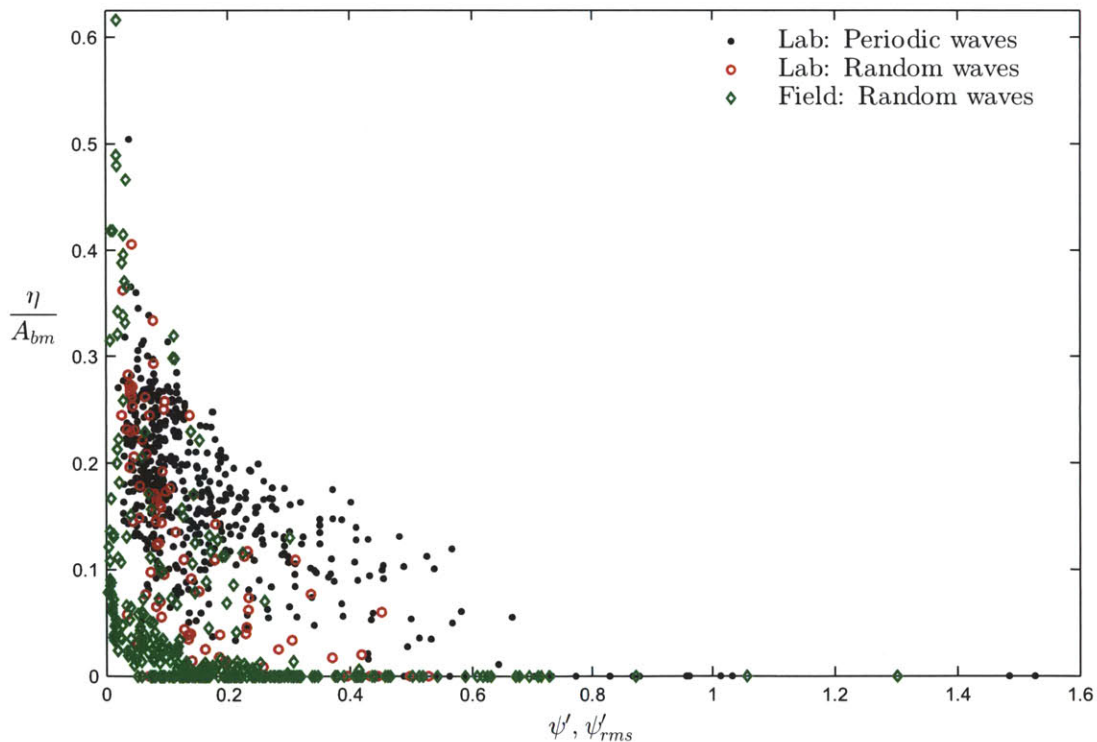
Figure 3-2: Ripple height variation with the skin-friction Shields parameter, ψ', for periodic (black dots) and random (red circles) waves in the laboratory and random waves in the field (green diamonds).

The field data have much wider scatter than the laboratory data, as would be expected, since ripple dimensions are much harder to accurately measure in the field, and researchers use different techniques to determine the representative ripple height in an area. Also, in some of the field data there may have been currents present which impacted the results. However, even accounting for the scatter, the field data show a different trend than the laboratory data: the ripple heights in the field drop off much faster than in the lab, making the curvature of the field data much sharper. The ripples in the field wash out as the bed transitions to sheet flow for much smaller values of ψ'. Note that these trends are still evident even if the significant near-bottom velocity is used for the random wave data, which is not shown. Based on these results, we have decided not to include field data in our relationship for the ripple height. Also, we are ultimately interested in comparing the results of predicting the roughness using the predicted ripple height and using the predicted energy friction factor. Since all of the energy dissipation data are from the lab, by restricting ourselves to laboratory data for the ripple height we ensure that we are consistent in the development of both methods.

While the ripples under periodic and random waves follow the same general trend, the ripples under random waves decay much faster as the Shields parameter increases. The upper flat-bed (sheet flow) state is reached under random waves at about $\psi' = 0.4$, while the ripples under periodic waves do not disappear until $\psi' = 0.8$, suggesting a difference in the skin-friction Shields parameter of order 2. This difference is seen when the rms near-bottom orbital velocity is used in the Shields parameter for the random waves, i.e., $\psi'_{random} = \psi'_{rms} = \psi'(u_{bm} = u_{b,rms})$. However, if the significant near-bottom velocity is used for the random waves, i.e., $\psi'_{random} = \psi'(u_{bm} = u_{b,sig} = \sqrt{2}u_{b,rms}) = 2\psi'_{rms}$, the Shields parameter is essentially doubled and the transition to flat-bed occurs around $\psi' = 0.8$ for both wave conditions. Figure 3-3 and Figure 3-4 show the non-dimensional ripple height against the skin-friction Shields parameter, using the rms and the significant near-bottom orbital velocity, respectively, for the random waves. Note that even though the significant near-bottom velocity is used in the skin-friction Shields

parameter for the random waves, the rms excursion amplitude is used for both periodic and random waves.

Figure 3-3: Ripple height variation with the skin-friction Shields parameter, ψ', for periodic (black dots) and random (red circles) waves using the rms near-bottom orbital velocity for the random waves.

Figure 3-4: Ripple height variation with the skin-friction Shields parameter, ψ', for periodic (black dots) and random (red circles) waves using the significant near-bottom orbital velocity for the random waves.

It is physically reasonable to expect the larger waves in a random wave train to have a greater effect on the ripple dimensions than the smaller waves, which suggests that a near-bottom velocity greater than the rms velocity is necessary to represent random waves. Faraci and Foti (2002) and Williams et al. (2004) similarly found that a single relationship could be used to represent ripple geometry under both types of waves if the significant wave height was used for the random waves. Furthermore, representing random waves with the significant near-bottom velocity has been used to successfully consolidate data in other boundary layer processes, such as initiation of motion and ripple wash-out (Madsen, 2002). O'Donoghue et al. (2006) found that using the mean of the highest 1/10 near-bottom velocities for the random waves more effectively merged their periodic and random wave data than using the significant velocity; however, using the 1/10 velocity gave a worse fit for our data. It should be noted that the difference between the fits found using the significant and 1/10 near-bottom velocity is minimal since the random-wave data make up only about 20% of the full data set. We have

91

therefore decided to use the significant near-bottom velocity in the skin-friction Shields

parameter for the random waves as this consolidates the transition to upper flat-bed and gives a

better overall fit to our data. By defining the skin-friction Shields parameter as

$$\psi' = \frac{\frac{1}{2}f'_w}{(s-1)gd} \cdot \begin{cases} u^2_{bm}, & \text{for periodic waves} \\ \left(\sqrt{2}u_{b,rms}\right)^2, & \text{for random waves} \end{cases} \tag{3.12}$$

the ripple heights under both types of waves are effectively merged. The near-bottom wave

orbital amplitude, however, is defined with the rms near-bottom velocity for random waves,

$$A_{bm} = \begin{cases} \dfrac{u_{bm}}{\omega}, & \text{for periodic waves} \\ \dfrac{u_{b,rms}}{\omega}, & \text{for random waves} \end{cases} \tag{3.13}$$

when calculating the skin-friction friction factor, f'_w, for the skin-friction Shields parameter, and

in the non-dimensional ripple height, η/A_{bm}.

While using the significant velocity in the Shields parameter consolidated the periodic

and random wave data, the data were still stratified according to sediment size, with the larger

diameters creating larger ripples for the same value of the Shields parameter (Figure 3-5).

O'Donoghue et al. (2006) noticed a similar trend in their field-scale experiments. They classified

the ripples as either 2D or 3D; the 2D ripples nearly always corresponded to diameters of 0.30

mm or larger while the 3D ripples were only found with diameters of 0.22 mm or smaller. The

dimensions of the 3D ripples, from the smaller sands, were reasonably well represented as a

constant fraction of the 2D ripple dimensions, given by multiplying the empirical 2D-ripple fit

by a factor smaller than one (e.g., 0.55 for the ripple height prediction). While our data showed a

distinct stratification according to sediment size, we did not have information on the bedform

type for all of the experiments, so we cannot comment on whether the stratification is related to

different ripple patterns. Van Rijn (2007) claims that bed roughness is proportional to sediment

diameter fro sand; since he took the roughness as proportional to ripple height, it follows that

ripple height is also proportional to sediment size. Similar to van Rijn, we did not see a clear

division between the ripple heights for sediments above or below a certain size as O'Donoghue et al. did, rather we saw a gradual decrease in ripple height with decreasing sediment diameter. In light of this continuous variation, we included a factor of $S_*^{-0.25}$, with the power found by a least squares fitting to the data, with the non-dimensional ripple height to lessen the sediment size stratification (Figure 3-6).
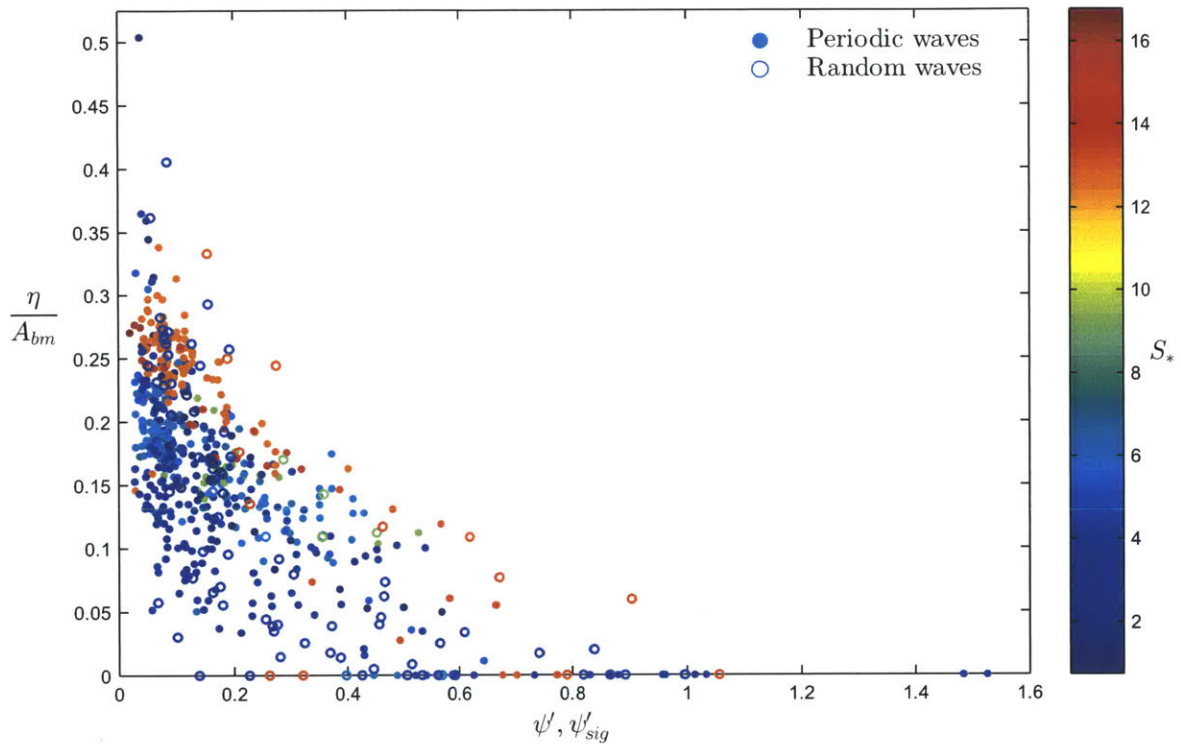
Figure 3-5: Ripple height variation with the skin-friction Shields parameter, ψ', for periodic (dots) and random (open circles) waves colored by the fluid-sediment parameter, S_*, to show sediment size stratification.
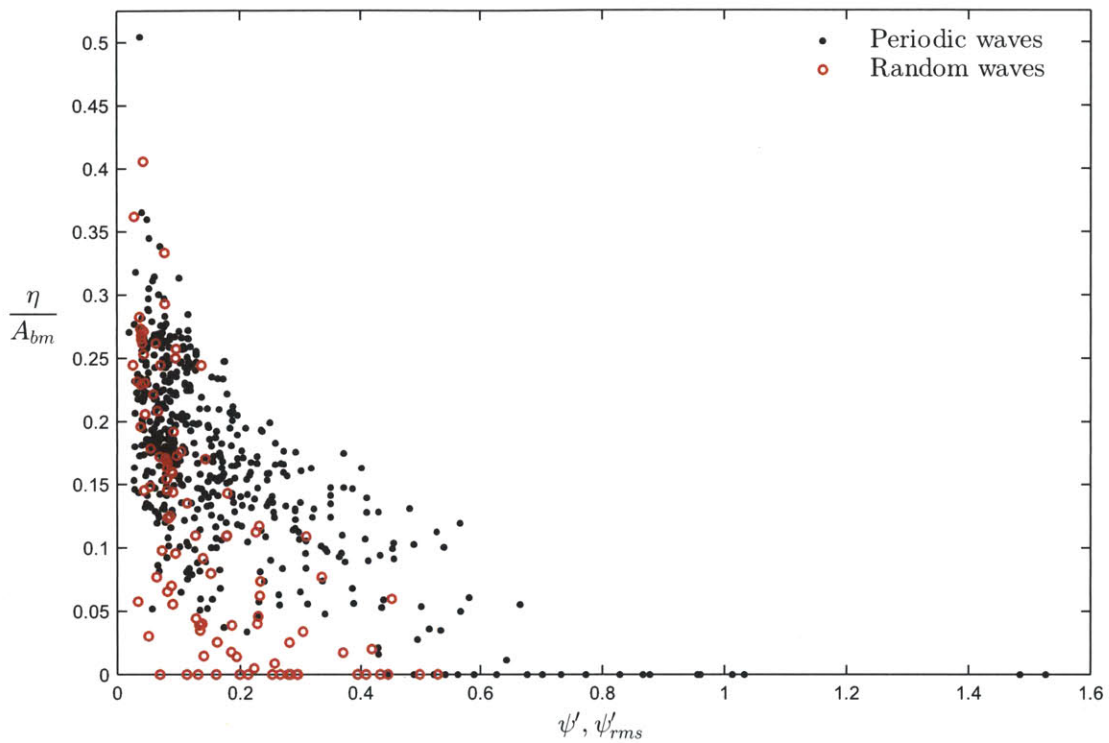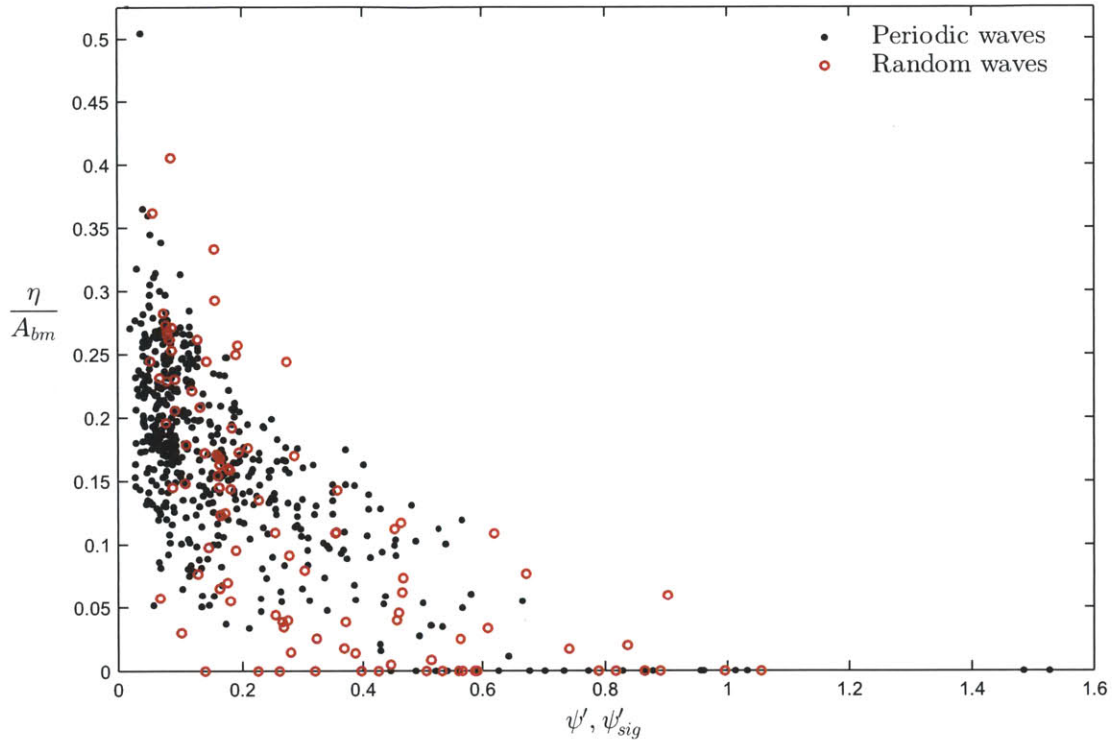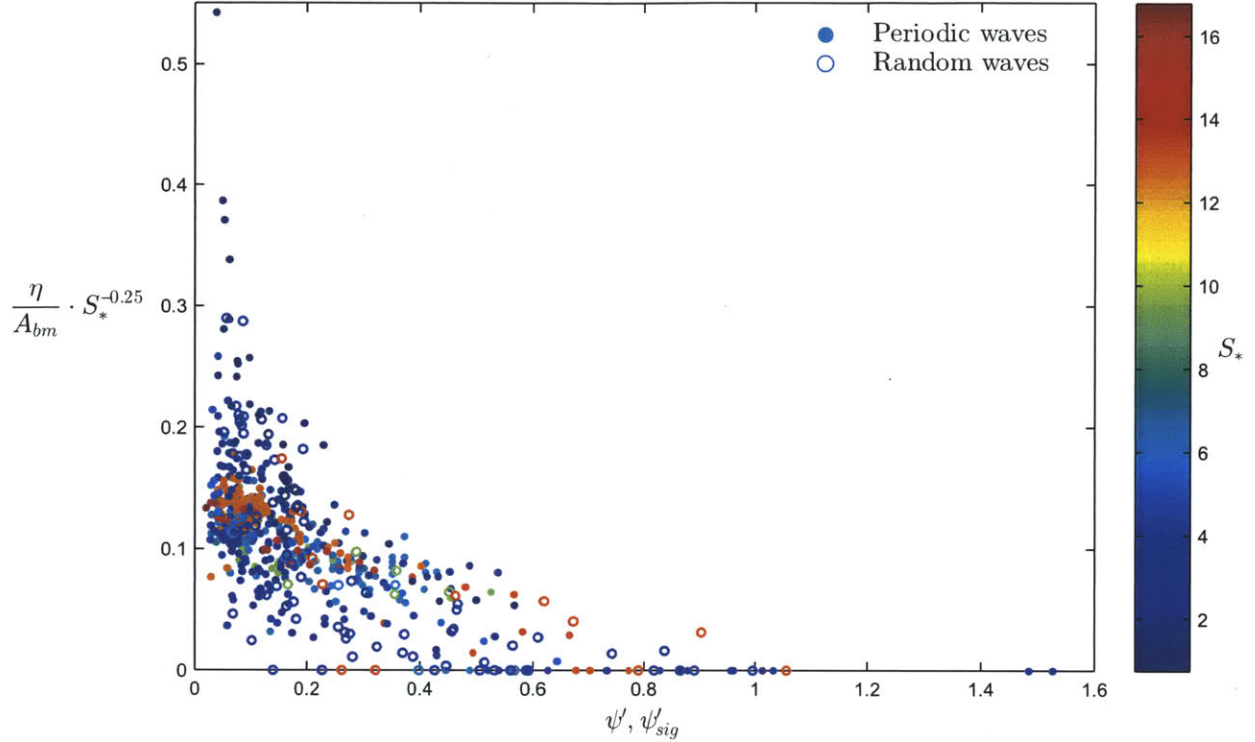
Figure 3-6: Ripple height variation with the skin-friction Shields parameter, ψ', for periodic (dots) and random (open circles) waves colored by the fluid-sediment parameter, S_*, with an S_* factor to lessen the sediment size stratification.

While including an S_* factor worked well with these data, whether it is the optimal method to destratify the data is unknown; however, there does appear to be an emerging consensus that, overall, ripple height, and thus bed roughness, increases with sediment size. Including this S_* factor and using the significant near-bottom velocity for the random waves, such that ψ' is defined by (3.12), a single relationship can be found that fairly well represents ripple heights under both types of waves and for a wide range of sediment sizes:

$$\frac{\eta}{A_{bm}} = 0.16 \exp\{-2.55\psi'\} S_*^{0.25} \tag{3.14}$$

This equation, found by a least squares fitting, does a reasonable job representing both the periodic and random wave data, despite the inherent scatter: 59% of the data lie within ±25% of the best-fit line, and 80% of the data lie within ±50% of the best-fit line (Figure 3-7).
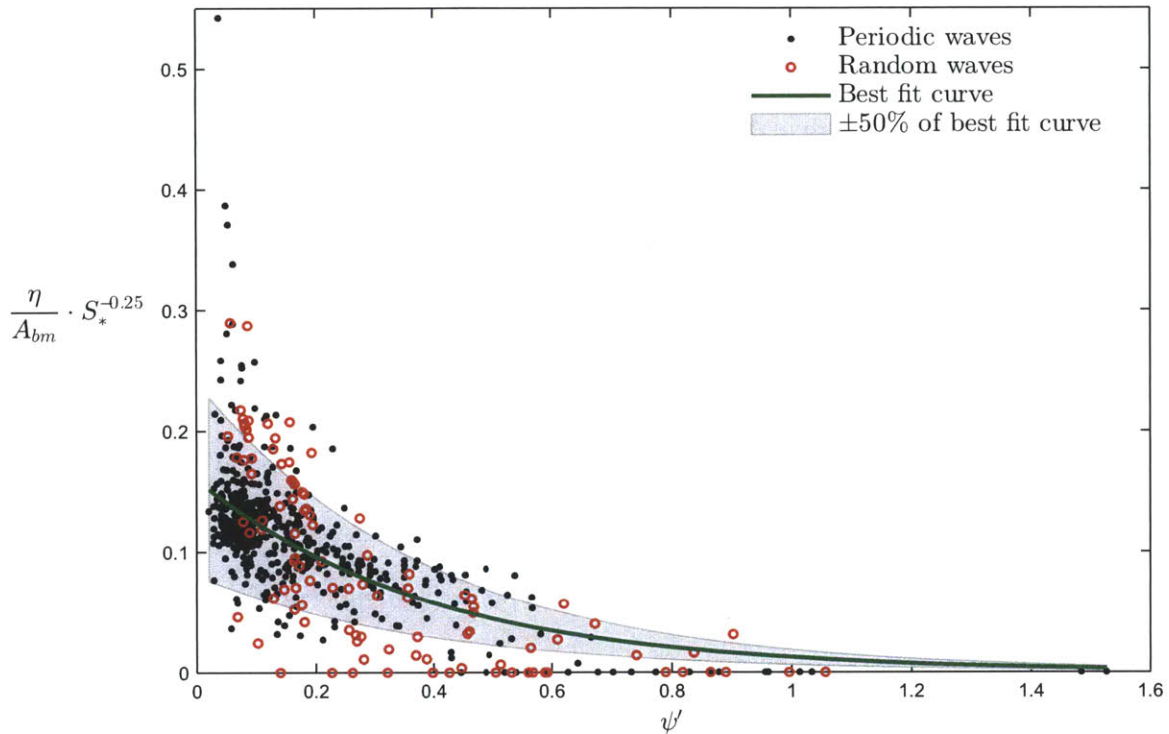
Figure 3-7: The new best-fit relationship for the ripple height (green line) well represents ripples under both periodic (black dots) and random (red circles) laboratory waves, with 80% of the data found within ±50% of the best-fit curve (gray area).

After the ripple height is predicted with (3.14), the roughness may be assumed to be a constant multiple of the ripple height. How to determine the proportionality constant, which depends on the chosen friction factor model, is detailed in Chapter 4.

3.4 Ripple regime: energy friction factor

As the ripple dimensions are not otherwise needed, predicting them is an unnecessary step in estimating the bed roughness and may introduce unnecessary error. If the energy friction factor is predicted instead, the roughness can be back-calculated using any desired theoretical friction factor model without the need for a model-dependent constant. Using an empirical relationship for the energy friction factor allows the roughness to be determined entirely from wave, sediment, and fluid information.

3.4.1 Available data

As explained in section 2.3, by measuring the wave height decay along a wave flume the energy dissipation factor can be directly calculated from measurements without using any theoretical model. To isolate the dissipation due to the bed roughness, the wave height decay is measured over a smooth bed, and this quantity is subtracted out of the total measured energy dissipation. Four of the five data sets used in the energy friction factor analysis use this method, including the two data sets which measured dissipation under random waves.

Another experimental technique directly measures the shear stress on the bed via a shear plate installed in the bottom of a wave tank. Shear plates have been used with fixed beds in the past, but recently the technology has improved to the point that tests can be run with a movable bed. While a few researchers are using shear plates to calculate the stress with fixed or flat beds, only one study, conducted by Rankin and Hires (2000), could be found that used a shear plate with a movable bed in the ripple regime.

Rankin and Hires ran each test twice: once with sand (and they waited until the ripples were at equilibrium) and once without sand, to isolate the force on the plate due to the rippled bed. They also estimated the force on the plate due to the free-stream pressure gradient. To find the force on the plate due only to the rippled sand bed, the force on the smooth bed and the estimated force due to the free-stream pressure gradient were subtracted from the total force measured over the sand bed. After calculating the shear stress using the residual force on the plate and the area, the wave friction factor was found with

$$f_w = \frac{2\tau_{bm}}{\rho u_{bm}^2}$$

(3.15)

where u_{bm} was calculated from the wave height and period according to linear theory.

Due to the difference in experimental setup, for these data f_w is directly calculated from the measurements, whereas for the energy dissipation experiments, f_e is indirectly calculated from measurements. Although it is possible to convert values of f_w into equivalent values of f_e

using a friction factor model, one of the main benefits of developing a relationship for the friction factor instead of the ripple geometry is that this method is independent of the choice of friction factor model. Therefore, to keep the relationship free of any friction factor theory, because the two friction factors are expected to be quite similar, and since many models neglect the phase shift anyway, for this shear plate data, we assume $f_e \approx f_w$, and use the f_w values calculated directly from the measurements.

A list of the five data sets used in the energy friction factor analysis under periodic and random waves in the laboratory is provided in Table 3-6, and an overview of the datasets is found in Table 3-7.

Table 3-6: Laboratory datasets used in friction factor analysis

Set	Source	d (mm)	Periodic waves	Random waves
1	Carstens et al. (1969)	0.19	5	
		0.297	15	
		0.585	20	
2	Lofquist (1986)	0.18	20	
		0.55	62	
3	Rosengaus (1987)	0.20	17	10
4	Mathisen (1989)	0.12	6	11
		0.20	–	5
5	Rankin & Hires (2000)	0.23	10	

Table 3-7: Overview of laboratory datasets used in energy friction factor analysis

Flow type	No. datasets	No. data points	No. diameters	d (mm)	ψ', ψ'_{rms}	f_e
Periodic waves	5	155	8	0.12–0.585	0.02–0.64	0.06–0.47
Random waves	2	26	2	0.12–0.20	0.03–0.10	0.05–0.40

Attempts have been made to quantify energy dissipation in the field by measuring wave height decay (e.g., Treloar and Abernethy, 1978). However, there are multiple reasons to distrust this data: there are many sources of energy dissipation in the field and it is impossible to account for all of them accurately, wave refraction makes it difficult to accurately measure the decay, and near the coast, where these studies are typically conducted, some level of current

97

activity is to be expected, and it is not accounted for. Therefore, the data used in the energy dissipation analysis will be restricted to laboratory data, where the experiments can be better controlled and the results are more trustworthy.

3.4.2   Energy friction factor relationship for the ripple regime

Using the energy dissipation data in Table 3-7 we found a relationship to directly predict the energy dissipation factor from fluid, flow, and sediment characteristics. As in the case of ripple height, we found that the energy friction factor correlates well with the skin-friction Shields parameter, using, as before, the significant near-bottom velocity in the Shields parameter for the random wave data. The energy friction factor data were also stratified according to their sediment sizes, so we again included the factor of $S_*^{-0.25}$ to consolidate the different sediment sizes, where the best-fit power of S_* happened to be the same as for the ripple height analysis. Comparing Figure 3-8 and Figure 3-9 shows the effect of including the S_* factor: in Figure 3-8, without S_*, the data are clearly stratified by size, with the larger sediments dissipating much more energy for the same ψ', while in Figure 3-9, with the exception of a few outliers, the different sediment sizes follow the same curve.
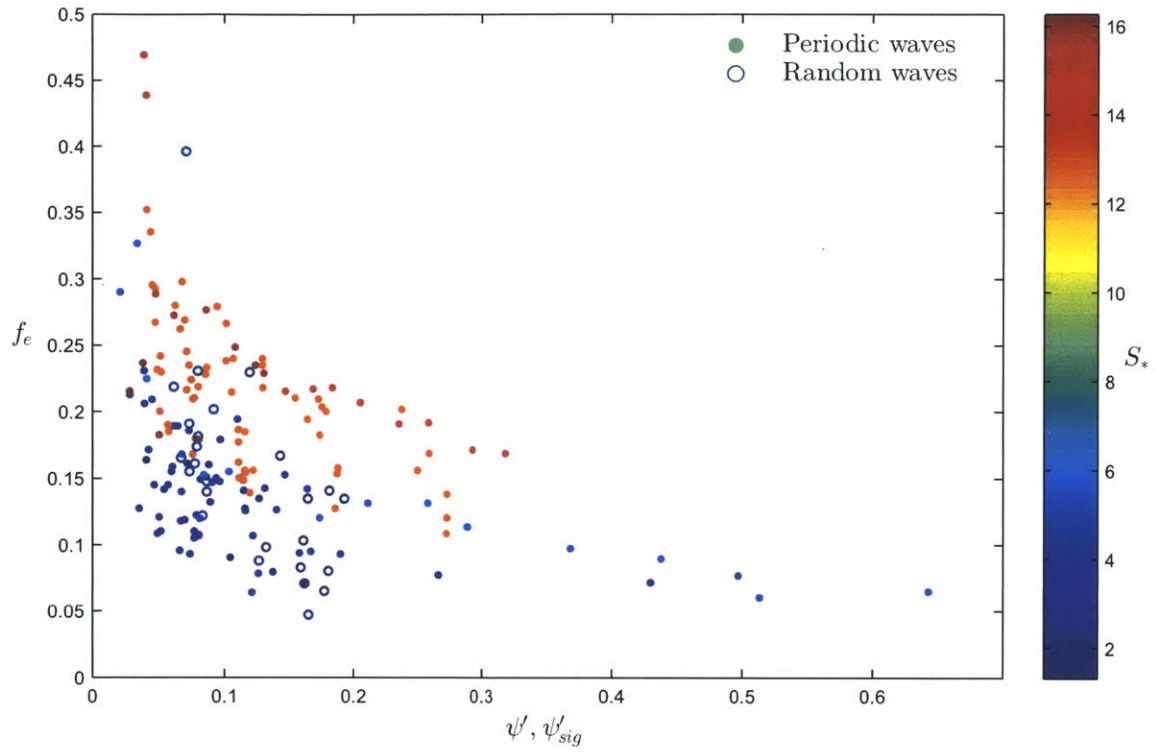
Figure 3-8: Energy friction factor variation with the skin-friction Shields parameter, ψ', for periodic (dots) and random (open circles) waves colored by the fluid-sediment parameter, S_*, to show sediment size stratification.
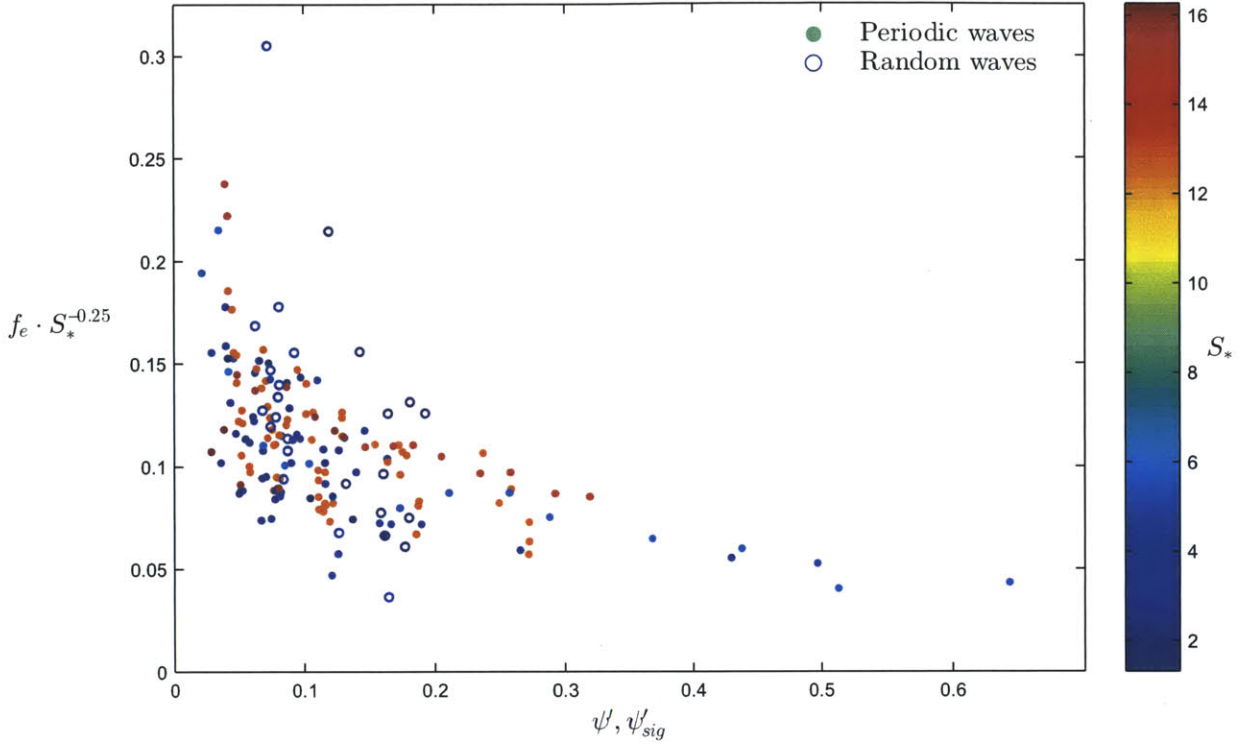
Figure 3-9: Energy friction factor variation with the skin-friction Shields parameter, ψ', for periodic (dots) and random (open circles) waves, colored by the fluid-sediment parameter, S_*, with an S_* factor to lessen the sediment size stratification.

Using the definition of the skin-friction Shields parameter given by (3.12), the energy friction factor can be predicted with (3.16), which was found by a least squares fit to the data.

$$f_e = 0.14 \exp\{-2.37\psi'\} S_*^{0.25} \tag{3.16}$$

This expression for the energy dissipation factor was developed solely from measurements over rippled beds and therefore is only applicable to the ripple regime, i.e., for $\psi' \lesssim 0.8$. The best-fit equation (3.16) fits the data well: 72% of the data are contained within ±25% of the best-fit line, and 95% of the data are contained within ±50% of the best-fit line (Figure 3-10).
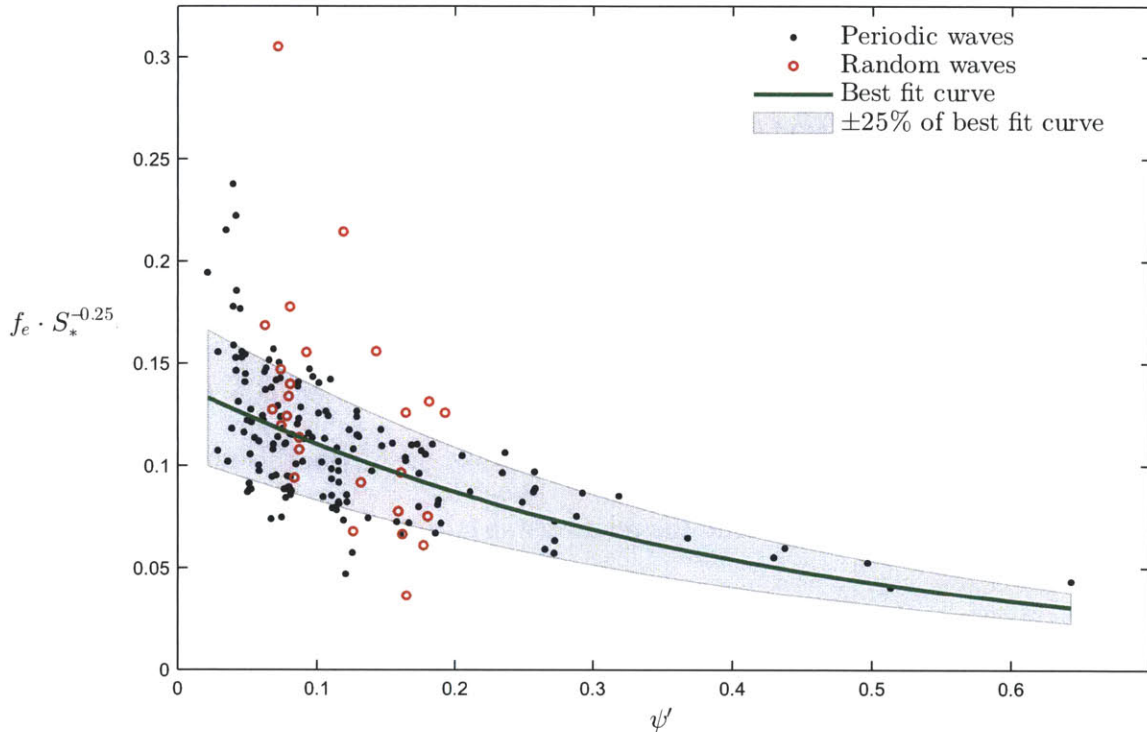
Figure 3-10: The best-fit relationship for the energy friction factor (green line) well represents ripples under both periodic (black dots) and random (red circles) laboratory waves, with 72% of the data found within ±25% of the best-fit curve (gray area).

3.5 Sheet flow regime

When the flow becomes strong enough, the ripples covering the bed are washed out and the bed transitions into the sheet flow regime, where the sediment is transported along the bed in a relatively thin layer. From Figure 3-7 of the ripple height relationship, it appears that the ripples wash out around $\psi' = 0.8$ and the sheet flow regime can be expected to start around $\psi' = 1$, and these values are applicable to random waves as well if the significant near-bottom velocity is used. While in the ripple regime the roughness is expected to scale with the ripple height, in the sheet flow regime there is no single fundamental vertical scaling for the roughness. Some researchers have proposed that the roughness scales with the sheet flow layer thickness or the erosion depth, but these quantities are not consistently defined and are difficult to measure accurately, especially in the field. If one of these length scales is measured or predicted by an

empirical expression, a friction factor model is generally then used to relate the roughness to the length scale, possibly including a model-dependent proportionality factor.

Having an energy friction factor relationship for the sheet flow regime would provide an appealing alternative to relating the roughness to a quantity which is difficult to measure and has not been proven to provide the correct scaling. As in the ripple regime, once an energy friction factor relationship is developed for the sheet flow regime, any friction factor model can be used to back-calculate the roughness, making the relationship independent of the choice of theoretical model. Therefore, we will find an empirical relationship for the energy friction factor using sheet flow data, which will extend the relationship for the ripple regime into the sheet flow regime.

3.5.1   Available data

In order to relate the flow conditions to the energy friction factor, measurements must be taken which allow the friction factor to be calculated. In the ripple regime, wave height decay was measured and used to calculate energy dissipation. This method works well in the ripple regime, when energy dissipation is so large that the wave height decay is easily measured, but in the sheet flow regime the energy dissipated by the bed is smaller, and this method becomes less reliable. It may be possible to measure the shear stress under sheet flow using a shear plate like Ranking and Hires (2000) used under ripples, but measurements of this type could not be found. Although many experiments are conducted in the sheet flow regime, the vast majority measure only transport rates and occasionally the sheet flow layer thickness, but not quantities which allow the friction factor to be calculated.

Dick and Sleath (1991) and Wijetunge and Sleath (1998) measured instantaneous velocity profiles under periodic waves in the sheet flow regime. They then analyzed the profiles to obtain estimates of the shear stress at the bed using the momentum integral method. Dick and Sleath conducted tests on two types of sediments: acrylic beads of median diameter 0.7 mm

and density 1.141 kg/m^3 and nylon granules of median diameter 4.0 mm and density 1.137 kg/m^3; Wijetunge and Sleath used only the larger nylon sediment. All of the experiments were conducted under periodic waves. An overview of the laboratory data is given in Table 3-8.

Table 3-8: Laboratory datasets used in sheet flow friction factor analysis

Set	Source	Material	d (mm)	$s = \rho_s/\rho$	No. data points
1	Dick & Sleath (1991)	Acrylic	0.7	1.141	17
		Nylon	4.0	1.137	8
2	Wijetunge & Sleath (1998)	Nylon	4.0	1.137	7

In the momentum integral method, the time derivative of the deficit velocity at each vertical level is vertically integrated to find the shear stress,

$$\tau(z) = \int_z^\infty \frac{\partial}{\partial t}\left(\rho u_\infty - \rho_m u(z)\right)dz \qquad (3.17)$$

where $\tau(z)$ is the shear stress at a vertical elevation z, u_∞ is the free stream velocity, and ρ_m is the density of the fluid-sediment mixture. Due to the presence of the sheet flow layer, the elevation of the bed, where τ_{bm} is located, is not clear, and must be defined. The authors decided to use the initial bed level to define τ_b, which is the elevation of the bed in still fluid, before transport begins. For these tests, the initial bed level was located 3-12 cm above the still bed level, which is the highest elevation for which there was no observable sediment motion throughout the wave cycle. Dick and Sleath also measured the thickness of the moving layer, the minimum elevation of the top of the moving layer over the wave cycle, relative to the still bed level. The elevation of the top of the moving layer was overall found to be very close to the initial bed level, which gives further credence to using the initial bed level to define the bed shear stress. With τ_{bm} known, the wave friction factor is found directly from its definition,

$$f_w = \frac{2\tau_{bm}}{\rho u_{bm}^2} \qquad (3.18)$$

As in the Rankin and Hires (2000) data, this method directly gives the wave friction factor, f_w, but not the energy friction factor, f_e, which are related by a cosine of the phase angle.

A friction factor model could be used to convert the values of f_w found directly from the data to values of f_e, which would be slightly smaller. However, because the relative roughness is so large in the sheet flow regime, $X \approx 20 - 500$ for these data points, the phase angle is small, and the cosine of the phase angle is close to unity. Compared to the uncertainty in the momentum integral method, the difference between the wave friction factor and the energy friction factor is negligible, and $f_e \approx f_w$ is assumed here. Because no friction factor model was used to alter the measured values, this method is independent of the choice of friction factor model.

3.5.2 Energy friction factor relationship for the sheet flow regime

In the ripple regime, we found that both the ripple height and the energy friction factor relationships were improved when the data was scaled by $S_*^{-0.25}$. Because there are so few data for the sheet flow regime, and they are composed of only two relatively large diameters, it is difficult to examine whether this trend continues for the sheet flow regime, but we will blindly assume that it still holds. Therefore, as an extension of the energy friction factor relationship for the ripple regime, we examined the variation of the scaled energy friction factor, $f_e \cdot S_*^{-0.25}$, with the skin-friction Shields parameter, ψ', for the sheet flow data (Figure 3-11).
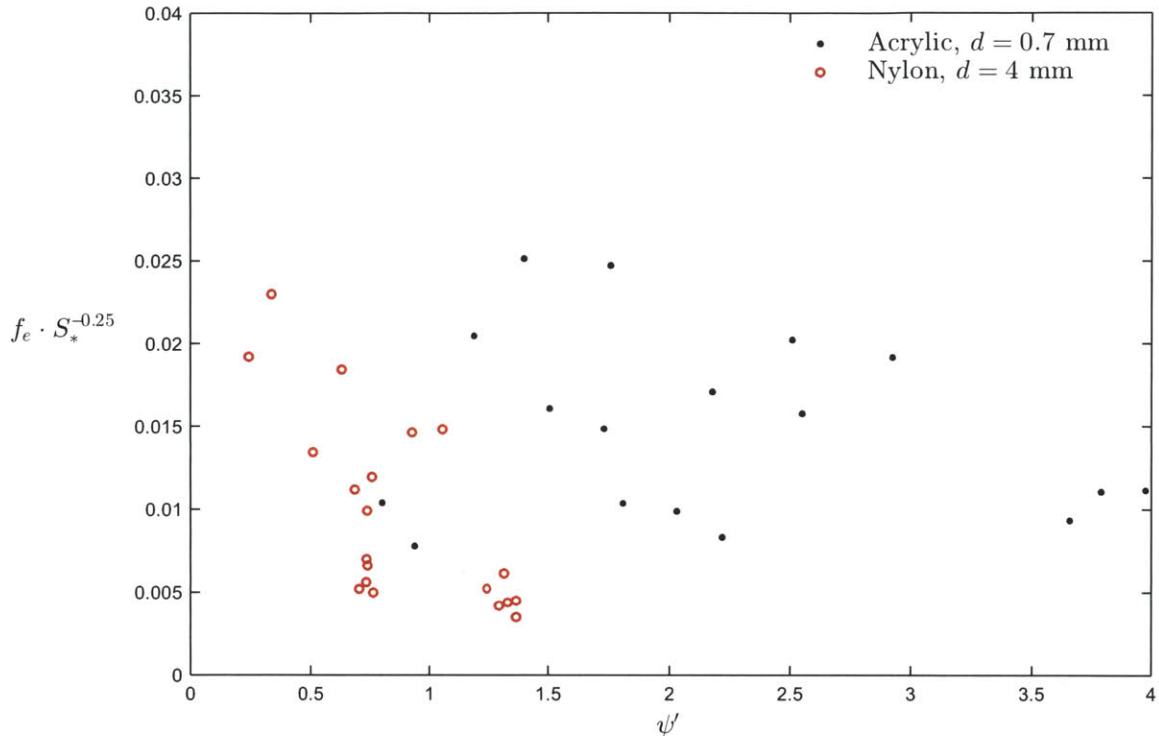
Figure 3-11: Energy friction factor variation with the skin-friction Shields parameter, ψ', for the sheet flow laboratory data (black dots: acrylic sediment, $d = 0.7$ mm, red circles: nylon sediment, $d = 4$ mm).

Dick and Sleath found that most of the runs with the nylon sediment ($d = 4$ mm, red circles in Figure 3-11) were in the ripple regime and some were in the transition regime between ripples and sheet flow, while all of the runs with the acrylic sediment ($d = 0.7$ mm, black dots in Figure 3-11) were in the sheet flow or transition regime. Of the Wijetunge and Sleath data, all of which used the nylon sediment, 5 runs had large enough ripples that the steepness was reported. Because we want to find a relationship which is valid for the sheet flow regime, we want to exclude those points which are in the ripple regime, as they do not fit in with the friction factor relationship for ripples. Dick and Sleath did not specify which data points were in the ripple regime, so we decided to exclude the three points with $\psi' < 0.6$ (Figure 3-11), since points with such low Shields parameter values are definitely expected to be in the ripple regime, as we found that ripples wash out around $\psi' = 0.8$. We also excluded the five points which Wijetunge and Sleath identified as having a rippled bed, for a total of 8 data points excluded due to being in the ripple regime, all of which used the nylon sediment.

105

Some of the data have such small values of the energy friction factor that they do not appear to fit in with the rest of the data points (Figure 3-11). Using the new friction factor model, the movable bed roughness, k_N, of the data points were computed from the reported values of the wave friction factor, f_w. For eight data points, the ratio of the computed roughness to the sediment diameter, k_N/d, was found to be less than or about equal to 0.5. The minimum roughness in any movable bed regime should be the sediment diameter, so the fact that these points gave roughness values smaller than the diameter by a factor of two shows that there is some unexplained experimental error for these points, and they were therefore excluded from the analysis. The cut-off was set at $k_N/d \leq 0.5$ instead of $k_N/d \leq 1$ to err on the side of including poor data rather than excluding reasonable data. Note that the same eight points would still have been excluded according to the criteria $k_N/d \leq 0.5$ if the Jonsson (1966) or Madsen (1994) friction factor models were used to calculate the roughness.

Of the 37 reported data points, a total of 14 points were excluded because they were in the ripple regime or had $k_N/d \leq 0.5$ (two data points met both exclusion criteria). The remaining 23 data points were analyzed to find the best-fit line for the energy friction factor. Due to the large scatter and the relatively small number of points, it seemed unreasonable to fit the data using a model more complex than a line:

$$f_e = [-0.0012\psi' + 0.016]S_*^{0.25} \tag{3.19}$$

The best-fit line (3.19) represents the data as well as can be expected, with 39% of the data points found within ±25% of the fit (Figure 3-12). The slope of the best-fit line is -0.0012, with 95% confidence bounds of $[-0.0036, 0.0012]$. Thus, the best-fit line for this data decreases slightly as ψ' increases, but accounting for the scatter and the few number of points, it is possible that the true relationship is horizontal, corresponding to a constant energy friction factor, or the slope may even be slightly positive. The only way to determine whether this best-fit relationship is valid is to analyze much more laboratory data.
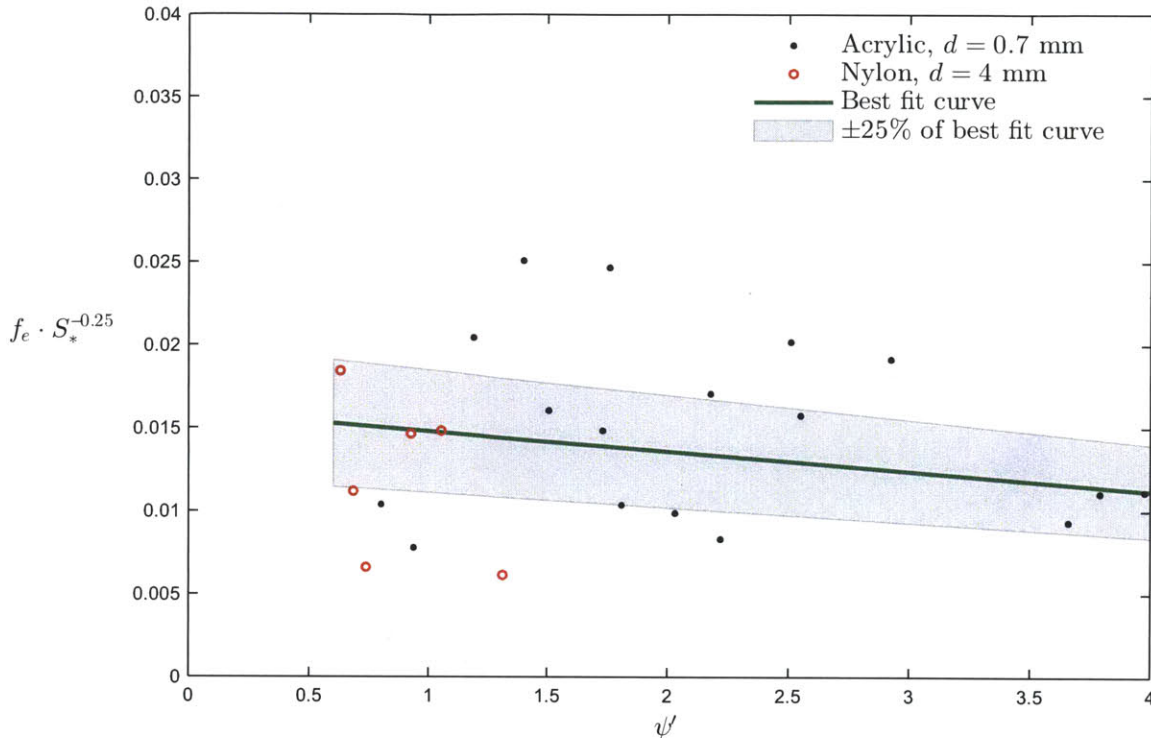
Figure 3-12: The best-fit relationship for the energy friction factor (green line) well represents sheet flow for both acrylic (black dots) and nylon (red circles) sediment under periodic laboratory waves, with 39% of the data found within ±25% of the best-fit line (gray area).

Because all of the sheet flow data is with periodic waves, it is not possible to test whether the rms or significant near-bottom velocity should be used to calculate ψ' for random waves; therefore, we will simply assume without proof that the significant near-bottom velocity should be used for random waves as was found for the ripple regime.

This new friction factor relationship can be combined with the relationship for the ripple regime (3.16) to provide a continuous expression over the entire range of ψ' values. The two expressions intersect at about $\psi' = 0.95$, which compares very well with our observation that ripples are washed out around $\psi' = 0.8$, and with other research that found that the sheet flow regime begins at $\psi' = 1$ (Nielsen, 1981). The smooth transition of the friction factor relationships between the ripple and sheet flow regimes (Figure 3-13) is another advantage of using the friction factor method to find the roughness, as opposed to using a method which requires predicting ripple dimensions or the sheet flow layer thickness first.
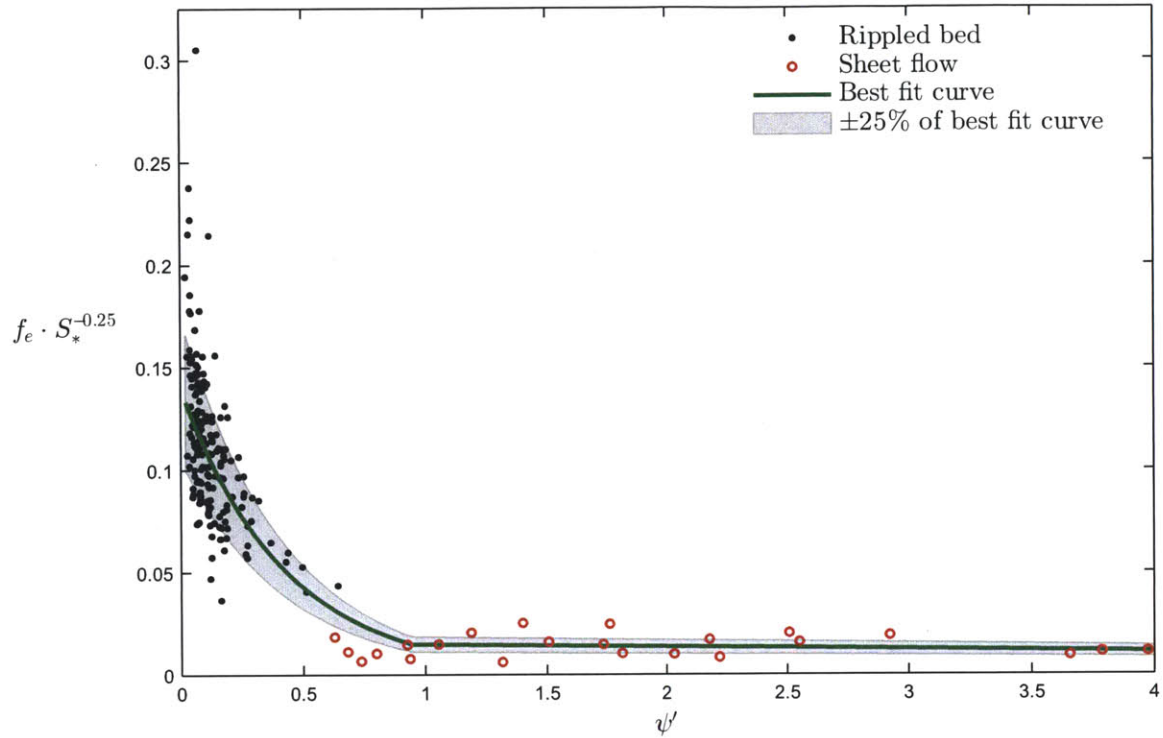
Figure 3-13: The best-fit relationship for the energy friction factor (green line) gives a continuous transition from the ripple to the sheet flow regime and well represents both ripples under periodic and random waves (black dots) and sheet flow under periodic waves (red circles), with 69% of the data found within ±25% of the best-fit curve (gray area).

Chapter 4

Movable bed roughness

In this chapter we explore ways to estimate the bed roughness in the movable bed regimes defined in Chapter 3. In the lower flat-bed regime, it is well understood that the roughness scales with the sediment size, and there is no reason to consider any other method of finding the roughness. In the ripple and sheet flow regimes, however, two methods are considered for estimating the roughness. The first method relies on a ripple height relationship or a relationship for the sheet flow layer thickness, and relates the roughness to these predicted length scales. The second method uses the new relationships for the energy friction factor developed in Chapter 3. Both methods rely on the energy friction factor data given in Chapter 3 and the new friction factor model derived in Chapter 2.

4.1   Lower flat-bed regime

In the lower flat-bed regime, the roughness scales with the grain size, as

$$k_N = \gamma_{fb} d \qquad (4.1)$$

where γ_{fb} is a proportionality constant for the flat-bed regime, and d is a characteristic diameter of the sediment. Common values of the constant γ_{fb} range from 1 to 2.5 when the median diameter is used. Some authors choose to use a larger diameter, often the 84th percentile diameter, $d = d_{84}$, in which case $\gamma_{fb} = 1$ is generally used. Because in many cases only the

median diameter is reported, we choose to use that diameter, $d = d_{50}$, and for simplicity take $\gamma_{fb} = 1$.

4.2   Ripple regime

In the ripple regime we consider two methods of predicting the roughness, corresponding to the two ripple regime expressions developed in Chapter 3. In the common method, the ripple dimensions are predicted, and the roughness is then estimated from the dimensions using a friction factor model-dependent constant. In the proposed method, the energy friction factor is predicted, and the roughness is back-calculated using any friction factor method.

4.2.1   Roughness from predicted ripple dimensions

As explained in section 3.3, in analogy with the flat-bed case, the roughness in the ripple regime can be expected to scale with the ripple size. Therefore, the common method of predicting bed roughness begins by predicting the ripple height, η, and possibly the length, λ, and the roughness is then taken as a function of these dimensions. The two most common relationships take the roughness as a constant multiple of the ripple height,

$$k_N = \gamma\eta \tag{4.2}$$

or as a constant multiple of the product of the height and the ripple steepness,

$$k_N = \beta\eta\frac{\eta}{\lambda} \tag{4.3}$$

where γ and β are the respective proportionality constants.

The difficulty with the common method thus comes in choosing the appropriate values for γ or β, which are not physically determined parameters. In fact, the correct value depends on the choice of theoretical friction factor model to be used in further computations and must be determined empirically for each model, for example by fitting experimentally observed energy dissipation rates. The chosen theoretical friction factor model is used to back-calculate the

roughness from the energy friction factor information, and the best-fit γ or β-value is determined by relating the roughness to the measured ripple dimensions. Once γ or β is known for a given model, the roughness is easily predicted from estimates of the ripple dimensions, usually predicted with an empirical relationship, such as those given in section 3.3.2 or the new relationship given in section 3.3.3.

Unfortunately, the published proportionality constants are often blindly applied without consideration to which friction factor model was used to determine them. This is especially disconcerting as the constants vary over a wide range. Some of the common values used for γ range from 1 (van Rijn, 2007) to 11 (Sleath, 2004), and β ranges from 8 (Nielsen, 1983) to 37 (Kim, 2004). Some of the quoted values for β are, in chronological order, $\beta = 25, 28, 8, 16, 20$, and 37, respectively, for Swart (1976), Grant and Madsen (1982), Nielsen (1983), Raudkivi (1988), van Rijn (1993), and Kim (2004). Clearly, blindly choosing a constant from a range this wide can lead to large errors in the roughness estimate.

The benefit of this method is that once the ripple dimensions are predicted, the roughness can be easily estimated as a function of those dimensions. Following Wikramanayake and Madsen (1994), Styles and Glenn (2002), and others, we choose to take the roughness as a function of the ripple height only, $k_N = \gamma_{rb}\eta$, where the subscript rb has been added to emphasize that this constant is for the rippled bed regime. As mentioned above, γ_{rb} varies with the choice of theoretical friction factor model and is determined from observed energy dissipation rates or shear stresses. The laboratory data of the energy friction factor under both periodic and random waves over movable beds used in the energy friction factor analysis (Table 3-6) were used to determine γ_{rb} for a few theoretical friction factor models. The best-fit γ_{rb}-value for a certain friction factor model is taken to be the whole-number value which yields the smallest mean absolute error between the measured energy friction factor and that predicted using $f_e = \mathcal{F}(k_N/A_{bm} = \gamma_{rb} \cdot \eta/A_{bm})$, with η/A_{bm} predicted by (3.14) from measured values of ψ' and S_*,

$$\frac{\eta}{A_{bm}} = 0.16 \exp\{-2.55\psi'\} S_*^{0.25} \tag{3.14}$$

The best-fit γ_{rb}-value was found to be 16 for the new friction factor model, 8 when the Madsen (1994) model is used, and only 2 for the Jonsson (1966) model. Thus, using the same expression for the ripple dimensions, (3.14), and the same energy friction factor data, the best-fit constant γ_{rb} varies by a factor of eight. A comparison of the predicted energy friction factor variation using the new model and the Jonsson model with their respective best-fit γ_{rb}-values is shown in Figure 4-1 along with the periodic and random wave friction factor data that was used to determine the best-fit γ_{rb}-values. To allow a single curve to represent all of the data for each model, the curves in Figure 4-1 use the approximate median sediment size, corresponding to $S_* = 8$; in reality each sediment size would generate a separate curve. Naturally, neither of the curves given by these models fits the data as well as the best-fit curve directly fit to the data, given by (3.16). The kink in the line for the new model, at $\psi' \approx 0.15$ for $S_* = 8$, corresponds to the critical value of X, which is where the model transitions from $\delta_t = \delta_w/6$ to $\delta_t = z_0 > \delta_w/6$ for small values of ψ'.
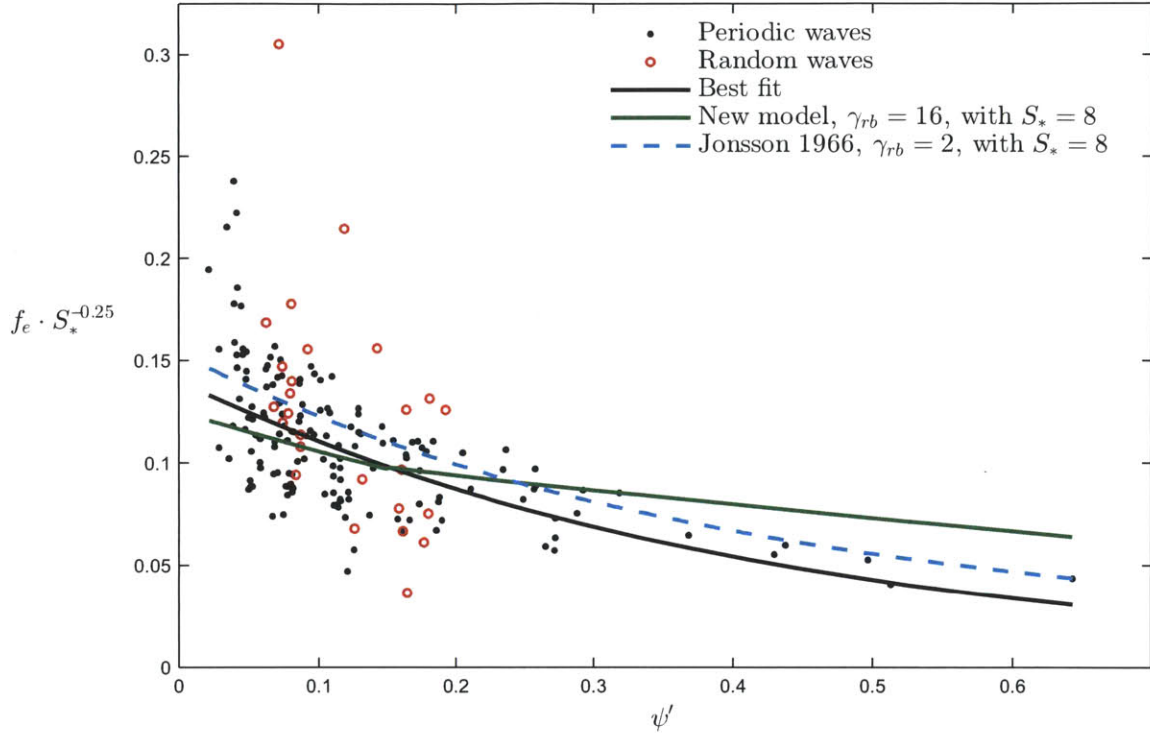
Figure 4-1: The energy friction factor data for periodic (black dots) and random (red circles) waves are used with the predicted ripple height to find the best-fit γ_{rb}-values for each friction factor model. For the new model (solid green line), $\gamma_{rb} = 16$, while for the Jonsson 1966 model (dashed blue line), $\gamma_{rb} = 2$, and both are plotted with $S_* = 8$. Neither of these models represents the data as well as the best-fit curve (black line).

The variability in γ_{rb} is a major shortcoming of the common method. Even if the ripple dimensions are predicted perfectly, the accuracy of the roughness prediction is nevertheless tied to the precision of this constant, which in turn relies wholly on the energy friction factor data. Because this method is ultimately constrained by the energy friction factor data, it makes sense to skip predicting the ripple height altogether and work with the energy friction factor data directly.

4.2.2   Roughness from predicted energy friction factor

The proposed method for determining the roughness in the ripple regime uses the empirical expression developed in section 3.4 to predict the energy friction factor, and skips predicting the ripple dimensions, which are not otherwise needed. Once the energy friction factor is

determined, any desired theoretical friction factor model can be used to calculate the roughness. To illustrate how the roughness can be back-calculated, the energy friction factor relationship for the ripple regime and the friction factor model developed in Chapter 2 were used to construct typical curves relating the relative roughness to the skin-friction Shields parameter, ψ', for a few sediments, specified by S_*. The relative roughness was found for three values of S_*, $S_* = 1, 8, 16$ (corresponding to $d = 0.1, 0.4, 0.7$ mm, respectively, for quartz in seawater), using the friction factor relationship,

$$f_e = 0.14 \exp\{-2.37\psi'\} S_*^{0.25} \tag{3.16}$$

and the relationship between the wave friction factor and energy friction factor,

$$f_e = f_w \cos \phi_\tau \tag{2.116}$$

where f_w and ϕ_τ were found from the explicit approximations for the pure-wave case, (2.86) and (2.87), respectively (Figure 4-2). Unfortunately, due to the complex form of the expressions for f_w and ϕ_τ, it is not possible to formulate a closed-form expression for the relative roughness as a function of the skin-friction Shields parameter and the fluid-sediment parameter. Again, kinks in the plot occur at the critical case, when the model transitions from $\delta_t = \delta_w/6$ to $\delta_t = z_0 > \delta_w/6$.
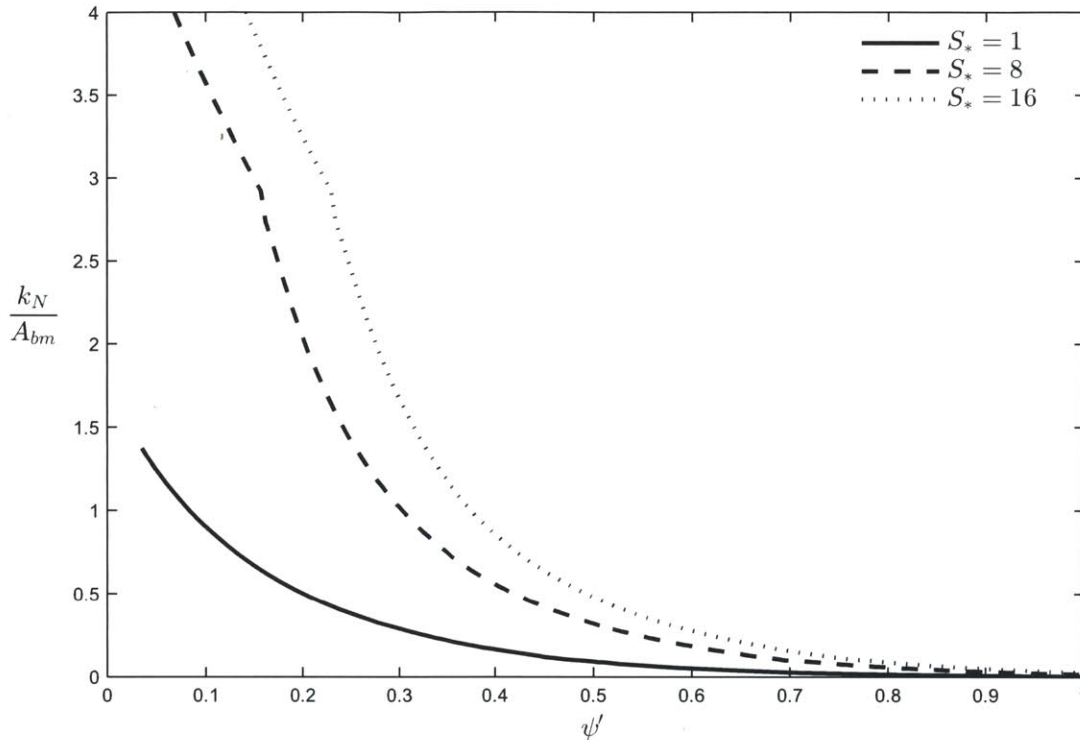
Figure 4-2: Using the new friction factor relationship for the ripple regime and the new friction factor model, the relative roughness can be back-calculated. The relative roughness thus depends on the skin-friction Shields parameter, ψ', and the fluid-sediment parameter, S_*.

The curves in Figure 4-2 were found using the new friction factor model, and using other models would generate somewhat different curves. As the friction factor models are very similar for small values of the relative roughness (large values of $X = A_{bm}/k_N$, Figure 2-20), the curves would merge for large values of ψ'.

4.3   Sheet flow regime

In the sheet flow regime, unlike the ripple regime, there is no single common approach to predicting the bed roughness. Some authors have found empirical relationships for the erosion depth or the thickness of the sheet flow layer and assumed the roughness scales with these lengths, sometimes using a theoretical model to determine proportionality constants as in the ripple regime. Less commonly, the roughness is determined for a set of combined wave-current data using a theoretical wave-current model, and then an empirical relationship is found for the

115

roughness as a function of the observed flow. As an alternative to these direct approaches, which require model-dependent constants, we can use the energy friction factor relationship developed in section 3.5 and back-calculate the roughness using any friction factor model.

4.3.1 Directly predicting the roughness in the sheet flow regime

From an extension of the idea that the bed roughness scales with the sediment size in the lower flat-bed regime and with the ripple dimensions in the ripple regime, some researchers have related the roughness in the sheet flow regime to a vertical scale of the sediment motion. Wilson (1989) proposed, as an extension of steady flow results, that the roughness in the sheet flow regime is proportional to the sheet flow layer thickness, measured from the top of the moving bed level to the still bed level. He found that the sheet flow layer thickness was proportional to the product of the Shields parameter and the sediment diameter, yielding

$$k_N = b\psi d \tag{4.4}$$

and he determined the constant to be $b = 5$ for his data.

From experimental data of sheet flow under steady flow, Herrmann and Madsen (2007) found the following empirical expression for the sheet flow roughness,

$$k_N = [4.5(\psi - \psi_{cr}) + 1.7]d_n \tag{4.5}$$

where d_n is the nominal diameter ($d_n \approx 1.1d_{50}$). Note that as these models use the total Shields parameter instead of the skin-friction Shields parameter, these expressions require iteration with a friction factor model to solve.

Other researchers have instead taken the roughness to be exactly equal to the erosion depth, which is the depth from the initial bed level (in still fluid) to the still bed level (during sheet flow). They have found, similar to Wilson, that the erosion depth is proportional to the product of the Shields parameter and the sediment diameter. These models generally use the skin-friction Shields parameter, calculated with Swart's (1976) model using $k_N' = 2.5d$, and as

the data analyzed for these models is mostly if not entirely comprised of periodic waves, it is not clear whether the rms or significant near-bottom velocity would be used for random waves. With a proportionality constant γ_{sf} (with the subscript sf referring to sheet flow conditions), this roughness model takes the form

$$k_N = \gamma_{sf}\psi'd \qquad (4.6)$$

and some reported values for the constant γ_{sf} are: 3 (Zala Flores and Sleath, 1998), 8.5 (Asano, 1992), and 7.8 and 3.5 for sediment of diameter smaller and larger than 0.2 mm, respectively (Dohmen-Janssen, 1999). Sawamoto and Yamashita (1986) found a better fit when the skin-friction Shields parameter was raised to the ¾ power, in which case their best-fit value for γ_{sf} was 3. The reported values for this constant show less variation than the γ_{rb} value used in the ripple regime, which may be due to the fact that the different theoretical friction factor models converge for the sheet flow regime or simply due to the authors using the same theoretical models when finding γ_{sf}.

From an analysis of wave-current field data in the sheet flow regime, Madsen et al. (1993) found that the roughness was approximately 15 times larger than the sediment diameter, where the Grant and Madsen (1986) boundary layer model was used. As all of these data were with $\psi' \approx 1$, Madsen (2002) proposed that the sheet flow roughness be represented in the same form as (4.6) with $\gamma_{sf} = 15$.

The sheet flow layer thickness is a difficult quantity to work with as it is difficult to measure, especially in the field, and is defined differently by different authors. Therefore, it did not seem worthwhile to develop an empirical relationship for the sheet flow layer thickness, as was done for the ripple height in the ripple regime. Instead, because it is the most widely used relationship, we will simply assume the roughness in the sheet flow regime can be represented by an expression of the form of (4.6), where the constant γ_{sf} can be determined from laboratory data just as γ_{rb} was found for the ripple regime. With this choice, it is inconsequential whether

this expression accurately predicts the sheet flow layer thickness, which, like the ripple height, is not otherwise needed. The best-fit constant γ is found by comparing the measured energy dissipation factor to the predicted values, $f_{e,pred}$, for different values of γ, where $f_{e,pred} = \mathcal{F}(k_N/A_{bm})_{pred}$. In the ripple regime, the best-fit γ_{rb}-value for each data point is found for a certain model from knowledge of ψ' and S_* only, since $(k_N/A_{bm})_{pred} = \gamma_{rb}(\eta/A_{bm})_{pred}$, and $(\eta/A_{bm})_{pred}$ is a function of ψ' and S_*. As we expect f_e to vary with ψ' and S_*, it is not a problem that $f_{e,pred}$ is also a function of these parameters, and as a result it is reasonable to expect γ_{rb} to be a constant. However, in the sheet flow regime the process is more complicated due to the form of the roughness expression (4.6). In the sheet flow regime, $(k_N/A_{bm})_{pred} = \gamma_{sf}(\psi'd/A_{bm})_{pred}$, and $(\psi'd/A_{bm})_{pred}$ is a function of ψ', S_*, ω, $s = \rho_s/\rho$, and ν. Thus, in the sheet flow regime, $f_{e,pred}$ depends not only on ψ' and S_*, as expected, but also on ω, s, and ν, and as a result γ_{sf} may not be a constant, but may depend on these parameters.

Assuming the roughness can be represented by (4.6), the energy friction factor sheet flow data used in the friction factor analysis (Figure 3-12) were used to determine the best-fit γ_{sf}-value for a few theoretical models. Since there is very limited laboratory data, it was not possible to determine if the factor γ_{sf} is in fact a constant for a given theoretical model, but it will be treated as a constant here for lack of a better option. The best-fit γ_{sf}-value was found to be 4 for the new friction factor model and the Madsen (1994) model, while it is 3 for the Jonsson (1966) model. The best-fit γ_{sf}-values for the different models are much closer than the γ_{rb}-values for the ripple regime, where the constant varies by a factor of eight between the different models. This is because in the sheet flow regime the relative roughness is smaller ($X = A_{bm}/k_N$ is larger), and the different friction factor models converge to similar values as the relative roughness decreases, as shown in section 2.5. Also, for large values of A_{bm}/k_N the wave friction factor is less sensitive to the roughness, so variations in k_N give relatively small variations in the friction factor.

Since the best-fit values for γ_{sf} are very similar in the sheet flow regime for different friction factor models, it would appear that there is not as strong of an argument against directly predicting the roughness as there is for the ripple regime. However, while γ_{sf} may not vary widely with the different friction factor models, it is actually far less reliable than γ_{rb} for the ripple regime, as it may depend on the values of ω, s, and ν of the data used to determine it. Unfortunately, there is very little laboratory data available in the sheet flow regime, and the datasets used here had very small values of s ($s \approx 1$) and large values of ω compared to what would be expected for quartz sediment in the field. We are therefore suspicious of the best-fit value of γ_{sf} found here with this limited data, $\gamma_{sf} = 4$ for the new model, and recognize that it may not be a general constant. Laboratory data of quartz sediment in sheet flow would be expected to give a more trustworthy estimate of γ_{sf} than was found for this data.

Directly predicting the roughness with a relationship of the form of (4.6) predicts that the roughness and therefore the energy friction factor increases with ψ', while the data shows that the energy friction factor decreases slightly on average (Figure 3-12). However, many researchers have found that the roughness increases as ψ' increases, and even for this data set the confidence interval on the predicted slope of the best-fit line for the friction factor shows that the energy friction factor may increase slightly with ψ'. Also, the momentum integral method is very sensitive to the level chosen to evaluate the shear stress, which was taken to be the initial still water bed-level for these experiments. As the skin-friction Shields parameter increases, the thickness of the moving layer and thus the distance between the top of the no-motion layer and the initial still water bed-level increases. If the no-motion depth was used to evaluate the shear stress instead, the shear stress and therefore the friction factor may have shown an increase with ψ'. On the other hand, the momentum integral method includes stresses between grains in calculating the shear stress, which could lead to overpredicting the shear

stress. Overall, the measurements with high ψ' are less trustworthy using this method, and therefore this data should not be used to disprove that the roughness increases with ψ'.

4.3.2   Roughness from predicted energy friction factor

As was done for the energy friction factor in the ripple regime, once the energy friction factor is predicted with the relationship developed for the sheet flow regime, any model can be used to back-calculate the roughness, which thus depends on both ψ' and S_*. This was done for three values of S_*, $S_* = 1,8,16$, using the sheet flow friction factor relationship (3.19),

$$f_e = [-0.0012\psi' + 0.016]S_*^{0.25} \tag{3.19}$$

and the new friction factor model, to see the relationship between the relative roughness for a range of ψ' values (Figure 4-3).
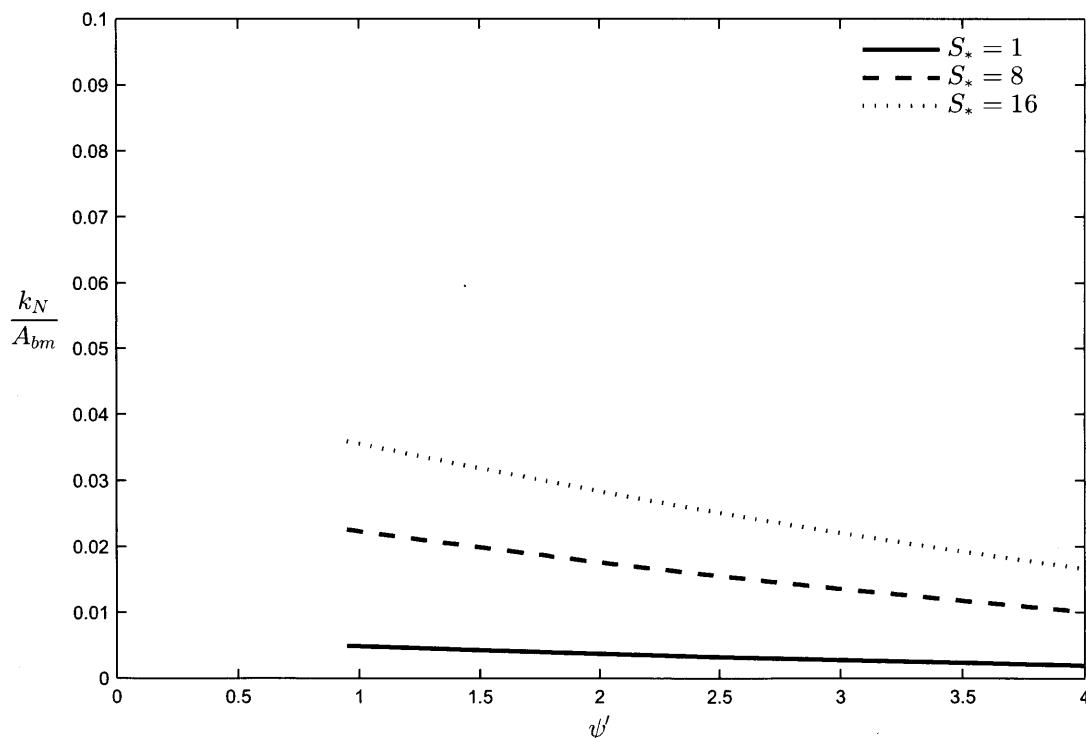
Figure 4-3: Using the new energy friction factor relationship and the new friction factor model, the relative roughness can be back-calculated for the sheet flow regime. The relative roughness thus depends on the skin-friction Shields parameter, ψ', and the fluid-sediment parameter, S_*.

Note that while the relative roughness decreases as ψ' increases, this does not imply that the roughness decreases with ψ', which would be contrary to expectations and previous observations. This is because as ψ' increases for the same sediment, A_{bm} would also increase (unless the wave period shortened considerably, which is unlikely). Therefore, while the relative roughness, k_N/A_{bm}, decreases as ψ' increases, as long as A_{bm} increases faster, the roughness, k_N, would increase with ψ' for a given sediment. For example, if ψ' increases from $\psi' = 1$ to $\psi' = 3$ while the wave period remains constant, the roughness increases by about 15% for quartz sediment with $S_* = 8$.

Again, a major benefit of the friction factor method is that it provides a continuous variation from the ripple to the sheet flow regime. Because the energy friction factor relationships vary smoothly between the two regimes, the relative roughness also has a continuous variation (Figure 4-4).
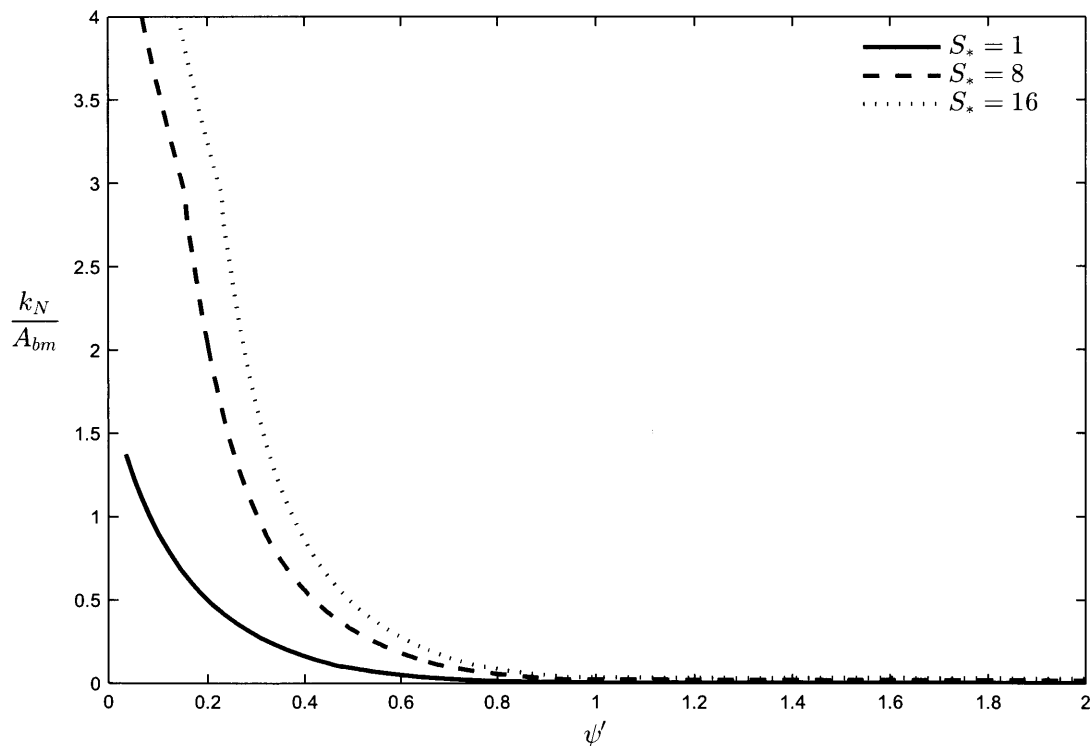
Figure 4-4: Using the new energy friction factor relationships for the ripple and sheet flow regimes and the new friction factor model, the relative roughness can be back-calculated. The relative roughness thus depends on the skin-friction Shields parameter, ψ', and the fluid-sediment parameter, S_*, and has a continuous smooth transition between the ripple and sheet flow regimes.

Validation of the sheet flow friction factor method with laboratory data

In the ripple regime, it is difficult to test the roughness methods with the new wave-current model using measured current velocity profiles because when the bed is rippled the near-bottom profiles over crests and troughs are different and it is unclear which should be used. However, as the bed is homogenous in the sheet flow regime, it is possible to test the roughness method by comparing the results with measured current profiles. The proposed sheet flow roughness method, using the predicted energy friction factor, was tested against two combined wave-current experiments under sheet flow conducted by Dohmen-Janssen (1999) in the Delft oscillating water tunnel (Table 4-1).

Table 4-1: Conditions for wave-current sheet flow experiments by Dohmen-Janssen (1999)

Case	d_{50} (mm)	T (s)	u_{bm} (cm/s)	u_r (cm/s)	z_r (cm)	ψ'
T1	0.13	4	104	25	5	1.64
T2	0.13	12	107	21	5	1.34

The energy friction factor was calculated with the new sheet flow relationship (3.19) with the measured ψ' and S_* values, and the bed roughness was back-calculated using the new expressions for the wave friction factor and phase shift developed in Chapter 2. The current profile was calculated using the new three layer model with the current specified by the reference velocity, u_r, at an elevation z_r, as detailed in section 2.2, where the two layer simplification of the current velocity profile was used. The current velocity profiles predicted by the new model agree well with the experimental results (Figure 4-5). These results help to verify both the theoretical wave-current boundary layer model and the proposed energy friction factor method for the sheet flow regime.
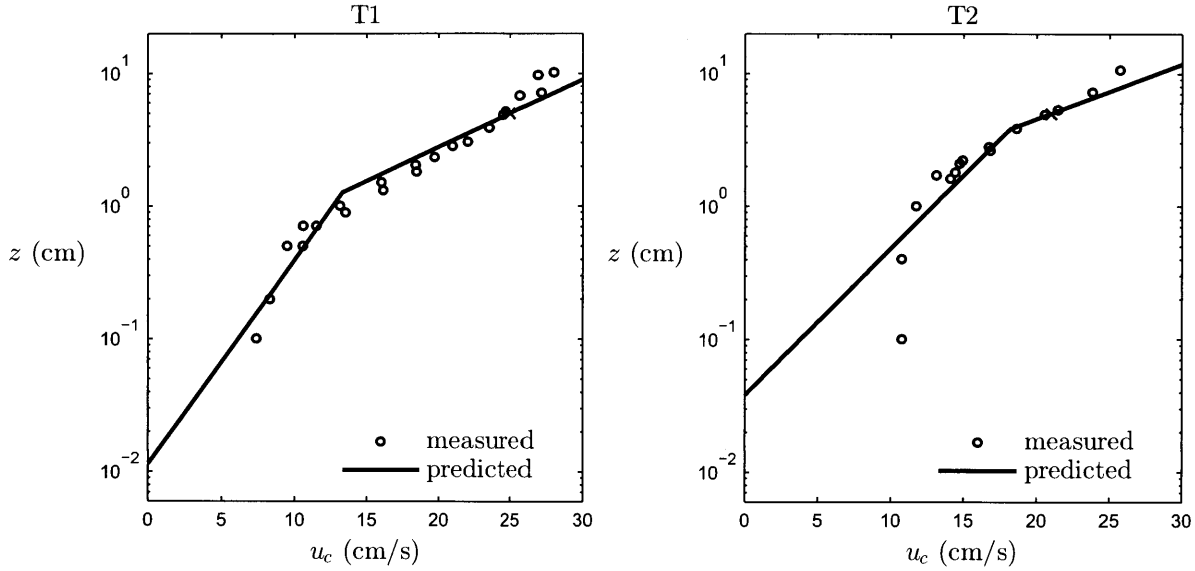
Figure 4-5: Comparison of predicted (lines) and measured (circles) current velocity profiles for two tests by Dohmen-Janssen (1999) of wave-current flows in the sheet flow regime. The red crosses indicate the reference velocity and elevation used to predict the profiles.

4.4 Roughness prediction procedure

The roughness is predicted from knowledge of the sediment size and the wave conditions using the methods described in this chapter, with some of the relationships developed in Chapter 3, which are repeated here for convenience. In the lower flat-bed regime, when $\psi' < \psi_{cr}$, there is only one method, and the roughness is taken to be equal to the median sediment diameter,

$$k_N = d = d_{50} \tag{4.7}$$

For the ripple and sheet flow regimes, there are two methods considered, the common method, which is direct but requires a model-dependent constant, and the proposed method, with which any friction factor model can be used. For the common method, the roughness is proportional to the ripple height in the ripple regime or to $\psi'd$ in the sheet flow regime,

$$k_N = \begin{cases} 16\eta, & \psi' < 0.8 \\ 4\psi'd, & \psi' \geq 0.8 \end{cases} \tag{4.8}$$

where the constants $\gamma_{rb} = 16$ and $\gamma_{sf} = 4$ for the ripple and sheet flow regimes, respectively, are the best-fit constants for the new friction factor model, found by fitting energy friction factor laboratory data. The ripple height relationship was found by fitting laboratory data,

123

$$\frac{\eta}{A_{bm}} = 0.16 \exp\{-2.55\psi'\} S_*^{0.25} \tag{4.9}$$

Since there is not a smooth transition between the two regimes for this method, the expressions are assumed to switch at $\psi' = 0.8$, as this was when the ripples were seen to wash out.

For the proposed method, the energy friction factor relationships for the ripple and sheet flow regimes, found by fitting laboratory data of the measured energy dissipation rates or the shear stress, are given by

$$f_e = S_*^{0.25} \cdot \begin{cases} 0.14 \exp\{-2.37\psi'\}, & \psi' < 0.95 \\ -0.0012\psi' + 0.016, & \psi' \geq 0.95 \end{cases} \tag{4.10}$$

and the roughness can be back-calculated from f_e using the new model,

$$f_e = f_w \cos\varphi_\tau = \mathcal{F}\left(X = \frac{A_{bm}}{k_N}\right) \tag{4.11}$$

where the wave friction factor and the phase shift are found from X by solving the full model in section 2.1 with $\alpha = 0$ and $C_\mu = 1$, or with the explicit approximations, (2.86) and (2.87), respectively.

Chapter 5

Predictions of combined wave-current field flows

It is ultimately of interest to predict boundary layer hydrodynamics in the field, not the lab, and the theoretical model and empirical roughness methods are therefore rather useless if they do not perform well for field conditions. The methods were developed entirely with laboratory data, and there is no reason to believe that the relationships are applicable to field scale. For example, we found that the ripple height variation was different for field and laboratory data (Figure 3-2), and it seems reasonable that the γ-values and energy dissipation friction factor, f_e, could likewise be different under field conditions. Nevertheless, since the expressions would be used to make predictions in the field, it is prudent to evaluate the methods with field data.

Since both waves and currents, to varying degrees, are typically found together in the field, a wave-current model must be applied to make predictions under these conditions. After the roughness is predicted using either method from measured wave and sediment information, a wave-current model can be applied with measured wave, sediment, and current information, along with the predicted bed roughness, to predict the combined flow parameters.

In this chapter we review the procedure to predict the current shear stress from measured wave, sediment, and current information, along with the predicted bed roughness using the new three layer wave-current model developed in Chapter 2, where the bed roughness is predicted with the methods developed in Chapters 3 and 4. The theoretical model and the

empirical roughness methods are then evaluated using field data on combined wave-current flow in the three bed regimes: lower flat-bed, ripple, and sheet flow.

This thesis is concerned only with the hydrodynamics of combined wave-current boundary layer flows, and therefore the quantities of interest are the shear stress and/ or the current velocity profile. The hydrodynamics can then be used to predict other processes. For example, if the shear velocity is estimated from the wind stress, the current velocity profile predicted by the model can be used in coastal circulation models. If the current velocity is known instead, the shear stress at the bottom predicted by the model can then be used to predict sediment transport. Note that the shear stress predicted by the model is the total shear stress, which in the ripple regime is not the appropriate shear stress to use for sediment transport, as it includes the effect of form drag over the ripples. To predict sediment transport in the ripple regime, the total shear stress must be converted into an effective sediment transport shear stress, which is the shear stress that acts directly on the sediment grains.

5.1   Wave-current prediction procedure

The theoretical combined wave-current boundary layer model developed in Chapter 2 and the roughness methods developed for the different movable bed regimes in Chapters 3 and 4 can be evaluated with combined wave-current field data. The roughness methods were developed solely with laboratory data, and these data sets are dominated by periodic wave data. Nevertheless, since the methods would be applied to field conditions, they must be verified with field measurements.

As explained in the wave-current solution procedure in section 2.2, along with wave, sediment, and roughness information, the current direction and either the current shear velocity or a reference current velocity must be used to specify the current in the model, which then predicts the other quantity. We will specify the current by a reference current velocity and predict the current shear velocity, which is the process that would typically be used if current

velocities were known, either from current meter measurements or from a circulation model, and sediment transport predictions were desired.

While we choose to evaluate the predicted current shear velocity using a reference velocity, the reverse process, evaluating the predicted reference velocity using the current shear velocity, is equally valid and would give similar results for the accuracy of the model. If the shear velocity is overpredicted by a certain percentage by the model, by employing the reverse procedure the reference velocity would be underpredicted by a similar percentage.

To predict the shear velocity, the environment is specified by the water density and kinematic viscosity, ρ and ν, respectively, the sediment is described by the median sediment diameter, $d = d_{50}$, and relative density, $s = \rho_s/\rho$, the waves are specified by their near-bottom orbital velocity, u_{bm}, and radian frequency, ω, and the current is specified by a reference current velocity at a reference elevation z_r, $u_{c,r} = u_c(z = z_r)$, and its direction relative to the wave motion, ϕ_{cw}. To be consistent across all of the field data, the reference current velocity is specified at an elevation of $z_r = 100$ cm above the bottom (cmab); when the current velocity was not directly measured at this elevation, the value was interpolated from the measured profile.

First, the wave and sediment information were used to predict the physical roughness height of the bed, k_N, by different empirical methods depending on the flow regime, as detailed in section 4.4. Then, the bed roughness was used with the current and wave information to predict the current shear velocity, u_{*c}, using the procedure described in section 2.2. The predicted current shear velocity, $u_{*c,pred}$, was then compared to the observed current shear velocity, $u_{*c,obs}$, found by the study authors by fitting a logarithmic profile to measurements of the current velocity profile.

Note that the wave-current model used to predict the current shear velocity should be consistent with the friction factor model either used to determine the γ-values for the common method of predicting the roughness, or used to calculate the roughness from the energy friction

factor for the proposed method. The new three layer wave-current model is employed consistently throughout this chapter. As waves in the field are certainly random, the significant near-bottom velocity is used to calculate the skin-friction Shields parameter for the roughness relationships, while the wave-current model requires the rms near-bottom orbital velocity.

5.2 Available data

Many researchers have conducted field studies on boundary layer processes in which wave and current information was recorded. However, testing the new model and roughness methods requires the observed current shear velocity, found by fitting measured current velocity profiles, which greatly limits the published data that can be used, as this analysis is not often conducted. By fitting logarithmic profiles to measurements of current velocity profiles, the current shear velocity, apparent roughness, and the elevation of the bed, if the researcher chooses to keep that parameter free, can be determined. Therefore, at least three current meters are required to find the two unknown parameters and to have a measure of the goodness of the logarithmic fit (at least four current meters are required if the elevation of the bed is also found). As a result, studies which only measured the current velocity at two elevations were not accepted, as it is not possible to gauge how logarithmic the profiles are with only two data points. With these constraints, nine data sets were found of current profiles in combined wave-current flows in the lower flat-bed, ripple, and sheet flow regimes in the field, yielding a total of 185 current shear velocities determined by the authors from the current profiles (Table 5-1 and Table 5-2).

Table 5-1: Wave-current field datasets used to evaluate the model and roughness methods

Set	Source	Depth (m)	d (mm)	No. data points Flat-bed	Ripple	Sheet flow
1	Grant, Williams, & Glenn (1984)	90	0.016		15	
2	Lambrakos, Myrhaug, & Slaattelid (1988)[1]	18	50	21	–	
3	Green, Rees, & Pearson (1990)	24	0.1	8	27	
4	Drake, Cacchione, & Grant (1992)	35	0.25		23	
5	Drake & Cacchione (1992)	145	0.04		28	
6	Madsen et al. (1993)	13	0.1		–	5
7	Green et al. (1995)	25	0.1		1	6
8	Xu & Wright (1995)[2]	14	0.12		4	
9	Styles & Glenn (2002)	12	0.4		47	

[1] Data are provided in Myrhaug and Slaattelid (1989)
[2] Subset only: the 4 sheet flow data points were excluded, as they are part of the Madsen et al. (1993) dataset

Table 5-2: Overview of combined wave-current field datasets used to evaluate methods

Regime	No. datasets	No. data points	No. diameters	d (mm)	ψ'_{sig}	$\mu = (u_{*c}/u_{*wm})^2$
Flat-bed	2	29	2	0.1 – 50	0.008 – 0.035	0.049 – 5.85
Ripple	7	145	5	0.1 – 0.4	0.003 – 0.57	0.010 – 4.33
Sheet flow	2	11	1	0.1	0.990 – 2.83	0.075 – 0.53

The movable bed regimes of the data were in general determined by the significant skin-friction Shields parameter, using the critical Shields parameter value for the separation between lower flat-bed and the ripple regime, and $\psi' = 0.9$ for the separation between the ripple regime and the sheet flow regime. However, for a few datasets (Drake et al., 1992; Drake & Cacchione, 1992; Green et al., 1990; and Grant et al., 1984), some of the data points were in the ripple regime and some appeared to be in the flat-bed regime judging by ψ', and visual inspection of the bottom showed that there were indeed bedforms on the bed. As it is not expected that when the flow drops below the critical value the ripples will instantly wash away, all of the data points in these sets were assumed to be in the ripple regime. The only exception to this was for the Green et al. (1990) data set, where measurements were taken after a large storm. The wave energy decreased continually while the tidal current remained strong, and by 20 hours after the beginning of the measurements, all signs point to the bed being flat, so the last eight data points in this set were assumed to be in the flat-bed regime, while the earlier data points were in the ripple regime.

The dataset of Green et al. (1995) was gathered just before and during a large storm; as a result the first data point is in the ripple regime and the others are in the sheet flow regime. The last reported data point was excluded from the analysis because it was recorded just before the tripod fell over and the measured current velocity profile from this burst yields an apparent roughness nearly 50 times larger than the next highest value.

For the Grant et al. (1984) dataset, the median diameter was 0.016 mm (10% clay, 20% sand, 70% silt), but the sediment size distribution was bimodal, with one peak for silt and the other for fine sand, at $d = 0.1$ mm (Drake and Cacchione, 1989). Because the silt goes into suspension easily, Cacchione et al. (1987) decided for a nearby site with very similar sediment to use a sediment size representative of the sand, which is expected to stay near the bed and control the bed roughness when the bed becomes armored. Following the same reasoning, the sediment for the Grant et al. (1984) dataset was assumed to be better represented by a diameter much larger than the median value, namely $d = 0.1$ mm, which is the same size used by Cacchione et al. (1987).

In most cases, the authors only reported values for the current shear velocity when the profiles were highly logarithmic, as determined by having a high R^2 value (Gross and Nowell, 1983). In these cases, all of the reported values were used. Green et al. (1990), however, reported many profiles along with their R^2 values, and to be consistent with the other authors, the profiles with R^2 less than 0.985 were excluded from the analysis.

A few of the datasets (Green et al., 1990; Green et al., 1995; Drake and Cacchione, 1992) do not provide the relative directions of the wave and current motion. For these datasets, because the model is not very sensitive to the angle between the waves and currents (Figure 2-17), it was decided to assume they were collinear, with $\phi_{cw} = 0$. Many of the datasets only gave the significant or 1/10 near-bottom velocity, but the wave-current model requires the rms velocity for random waves. The larger velocities were converted to rms values assuming the

wave spectrums were Rayleigh distributed, in which case the rms velocity is related to the significant velocity by $u_{b,rms} = u_{b,sig}/\sqrt{2}$, and to the 1/10 velocity by $u_{b,rms} = u_{b,1/10}/1.8$.

5.3 Lower flat-bed regime

In the lower flat-bed regime, there is a general consensus that the roughness is proportional to the sediment size by a factor of between one and 2.5, and we choose to take the roughness as equal to the median grain diameter. Because there is little debate about the roughness, applying the model to the flat-bed regime tests the wave-current model alone, without the effect of the roughness method. Note that while k_N was taken as equal to the sediment diameter, if the model showed the flow to be smooth turbulent, the smooth turbulent roughness was used for z_0, such that

$$z_0 = \max\left\{\frac{k_N}{30} = \frac{d}{30}, \frac{\nu}{9u_{*m}}\right\} \tag{5.1}$$

All eight data points from Green et al. (1990) were found to be smooth turbulent, while all of the data points from Lambrakos et al. (1988) were rough turbulent.

The new model does an excellent job predicting the flat-bed field data: the predictions are biased by a factor of 0.99±0.14 (Figure 5-1). The bias is taken as the average slope of the data points, that is, the average of the ratio of the predicted over the observed current shear velocities, equal to 0.99 in this case, and is given as plus or minus one standard deviation, 0.14 here, corresponding to an underprediction of 1±14% on average. With this definition, the line of the average slope can be expressed as $u_{*c,pred} = 0.99u_{*c,obs}$, where u_{*c} is the current shear velocity and the subscripts *pred* and *obs* refer to the predicted and observed values, respectively. For these data, with 29 points, 20 points (69%) are within one standard deviation of the average slope, shown by the gray area in the figure.
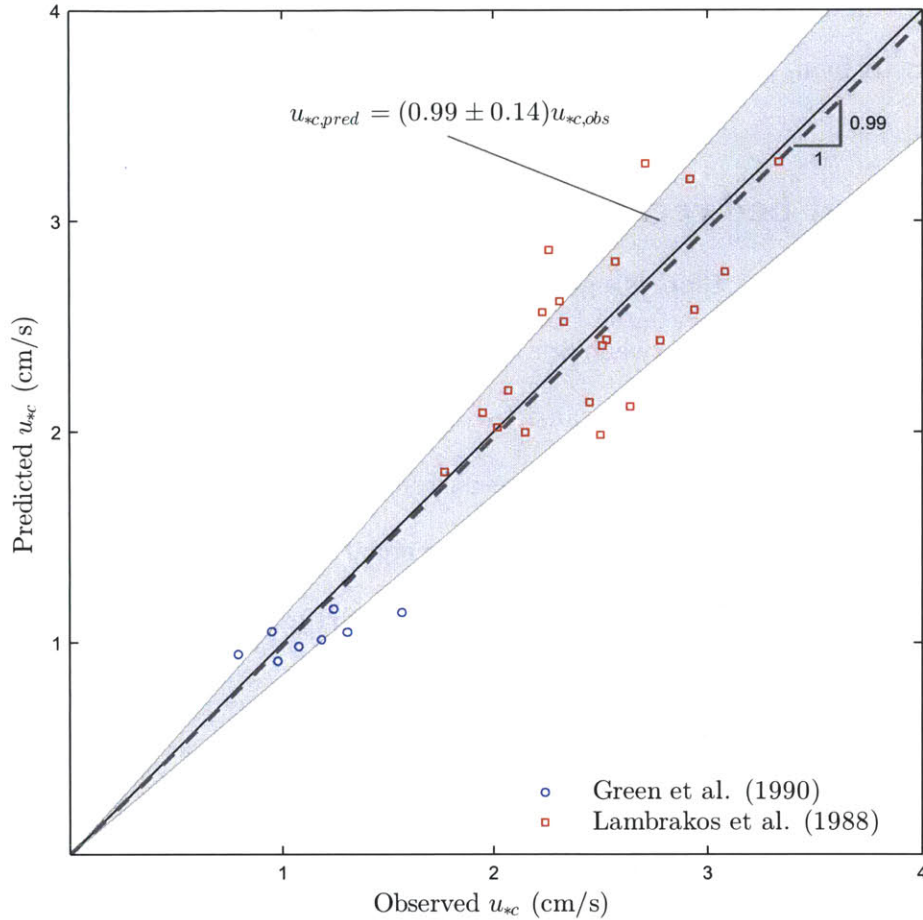
Figure 5-1: Comparison between predicted and observed current shear velocities in the flat-bed regime. The solid line denotes perfect agreement while the dashed line shows the average slope of the data points and the gray band covers ±1 standard deviation of the average slope, corresponding to an underprediction of 1±14%.

As noted in section 5.1, while we choose to compare the shear velocity using the reference velocity at 100 cm above the bottom as the current specification, if we instead went the other way and predicted the current velocity using the shear velocity as the specification, the error would be of similar relative magnitude, but opposite in direction. For this flat-bed data, if the reverse procedure is used, the current velocity at 100 cm above the bottom is overpredicted by 4% on average, with a bias of 1.04±0.18.

5.4 Ripple regime

In the ripple regime, the roughness is no longer a simple function of the sediment size, and therefore when comparing the results with field data, both the wave-current model and the roughness method are being tested. To evaluate the model and methods in the ripple regime, the roughness was predicted with the skin-friction Shields parameter for the waves alone using the relationships developed from laboratory data, and then the new wave-current model was used with the measured current and wave parameters to predict the current shear velocity.

For the common method of predicting the roughness, the ripple height was predicted with (4.9) and the bottom roughness was taken as 16 times the height, where $\gamma_{rb} = 16$ is the best-fit factor for the new model. The common method does a reasonable job predicting the field data: the predictions are biased by a factor of 1.20±0.22, so on average the predictions are 20% larger than the observations (Figure 5-2). For the proposed method of predicting the roughness, the energy dissipation factor was predicted with (4.10) and the new energy friction factor model was used to calculate the bed roughness. This approach predicts the current shear velocity somewhat better than the common method, giving a smaller and more tightly bounded bias of 1.12±0.19 (Figure 5-3).
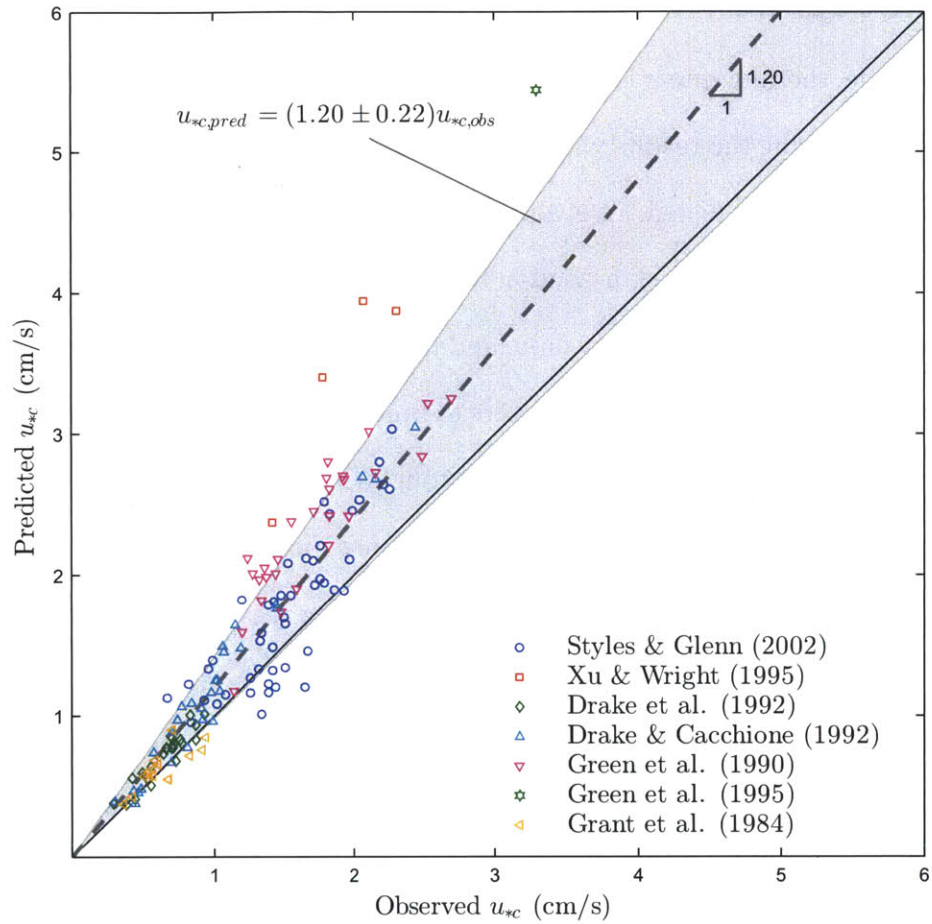
Figure 5-2: Comparison between predicted and observed current shear velocities in the ripple regime using the common method to predict the roughness. The solid line denotes perfect agreement while the dashed line shows the average slope of the data points and the gray band covers ±1 standard deviation of the average slope, corresponding to an overprediction of 20±22%.
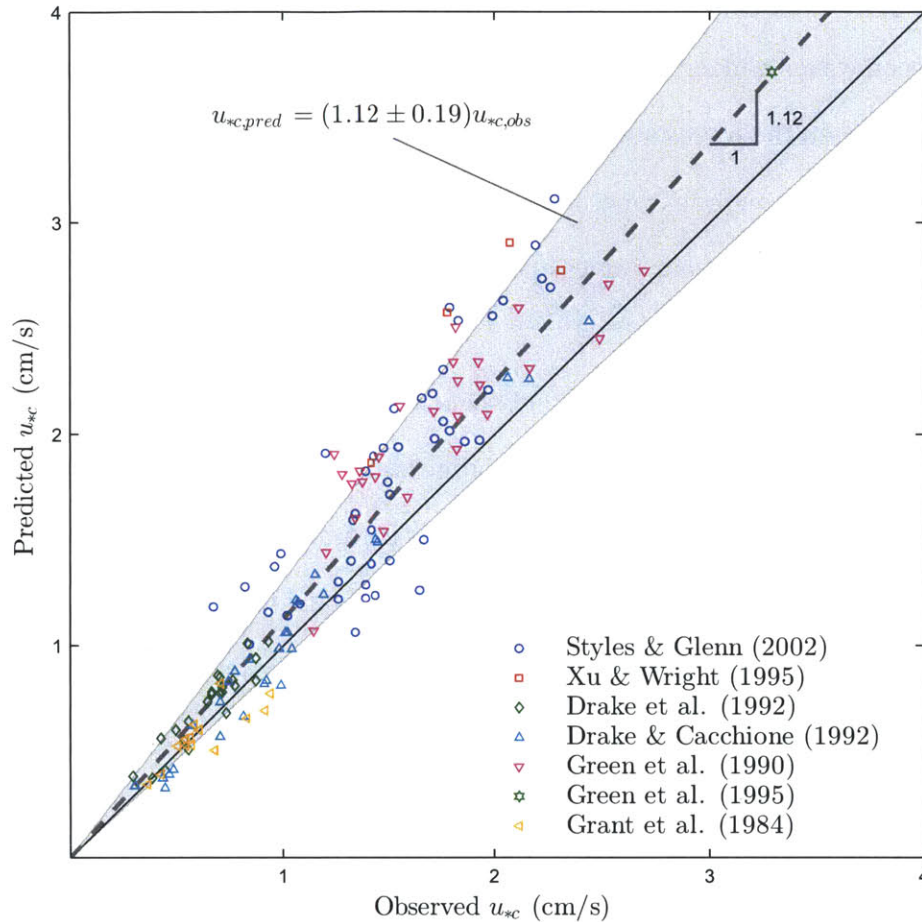
Figure 5-3: Comparison between predicted and observed current shear velocities in the ripple regime using the proposed method to predict the roughness. The solid line denotes perfect agreement while the dashed line shows the average slope of the data points and the gray band covers ±1 standard deviation of the average slope, corresponding to an overprediction of 12±19%.

If the current velocity at 100 cm above the bottom is predicted using the current shear velocity as the current specification, the current velocity is underpredicted by 15% and 10% on average with biases of 0.85±0.19 and 0.90±0.19 for the common (direct) and proposed methods, respectively, while the results above show that the current shear velocity is overpredicted by about 15% for both methods. The reverse procedure was employed with some of the data in this dataset using very similar expressions for the friction factor and ripple height and using the Madsen (1994) friction factor model in Humbyrd and Madsen (2011), who found that the current velocity 100 cm above the bottom was underpredicted by 6% and 8% for the common and proposed methods, respectively, in good agreement with these results.

A small part of the overprediction of the current shear velocity may be due to neglecting the angle between waves and currents when the value was not provided. If the maximum possible angle between the waves and currents, $\phi_{cw} = \pi/2$, was assumed for these cases, the bias using the proposed roughness method is 1.11±0.19, a reduction of 1%. Clearly, the model is so insensitive to the angle between waves and currents that assuming they are collinear when the angle is not provided is well justified.

Both methods overpredict the current shear velocity by more than 10% on average, resulting from an overprediction of the bed roughness. To predict a smaller, and presumably more correct, roughness, a larger value of the Shields parameter is required, which corresponds to a larger near-bottom velocity. This is true for both methods: for the common method, a larger Shields parameter predicts a smaller ripple height and by $k_N = \gamma_{rb}\eta$ a smaller roughness; for the proposed method, a larger Shields parameter predicts a smaller energy friction factor, which in turn gives a larger value of A_b/k_N, or a smaller roughness.

As mentioned in section 3.3, O'Donoghue et al. (2006) had success consolidating data from periodic and random waves by using the mean of the 1/10 highest near-bottom velocities for the random waves. Li and Amos (1999) found that the onset of sheet flow under combined wave-current flow in the field was well represented by the expression for waves alone (developed from mostly laboratory data) if the significant near-bottom velocity was used for the wave alone data and the 1/10 velocity was used for the combined wave-current data. Drake and Cacchione (1992) compared the predictions of a wave-current model using both the significant and 1/10 near-bottom velocities to describe their field data and found that while the current velocity profile was well predicted during non-storm conditions using either velocity, using the 1/10 near-bottom velocity gave better predictions of the current velocity and sediment response during storm periods.

In light of this evidence that the 1/10 near-bottom velocity may better characterize wave-current field flows, we also tested the methods using this larger velocity in the Shields parameter

to predict the roughness. Assuming the waves are Rayleigh distributed, the 1/10 velocity is related to the rms velocity by $u_{b,1/10} = 1.8u_{b,rms}$, whereas the significant velocity is related by $u_{b,sig} = \sqrt{2}u_{b,rms}$. Using the 1/10 velocity somewhat improves the predictions of both methods: the common method overpredicts the velocities by 17±20% and the proposed method overpredicts the velocities by 8±17% (Figure 5-4 and Figure 5-5, respectively), an improvement of about 3% in both cases. Note that while the 1/10 near-bottom velocity was used in the roughness prediction, the wave-current model requires the rms velocity.

Figure 5-4: Comparison between predicted and observed current shear velocities in the ripple regime using the common method to predict the roughness with the 1/10 near-bottom velocity. The solid line denotes perfect agreement while the dashed line shows the average slope of the data points and the gray band covers ±1 standard deviation of the average slope, corresponding to an overprediction of 17±20%.
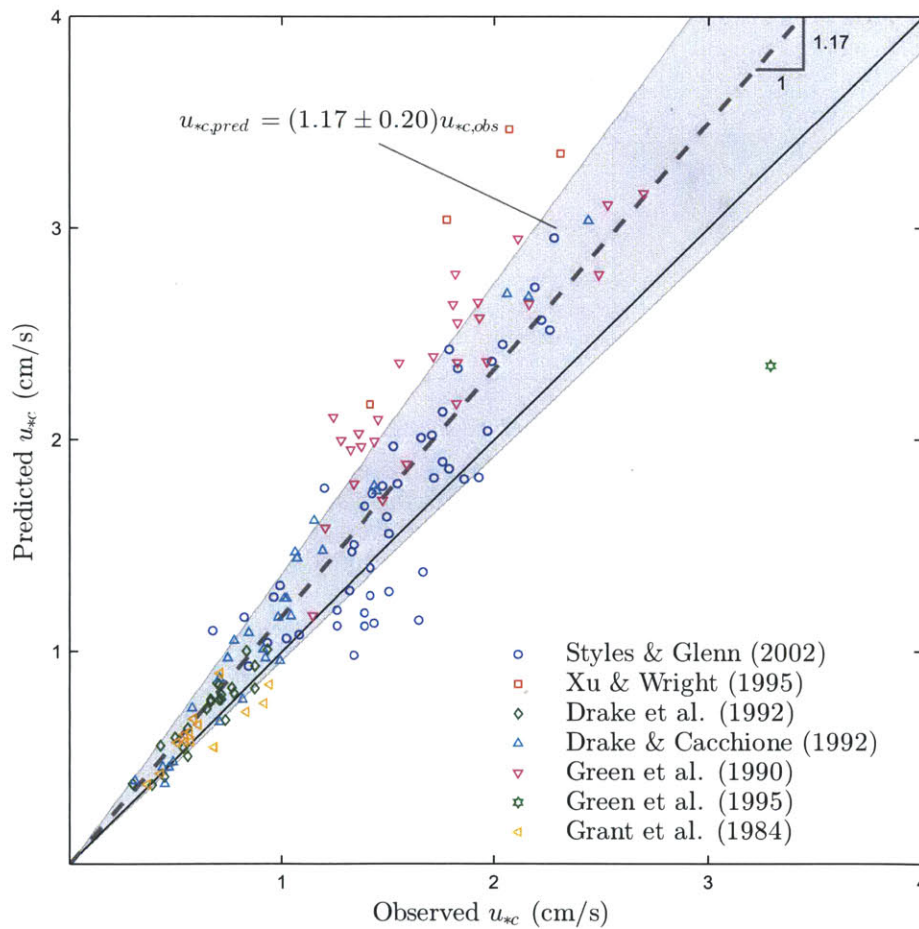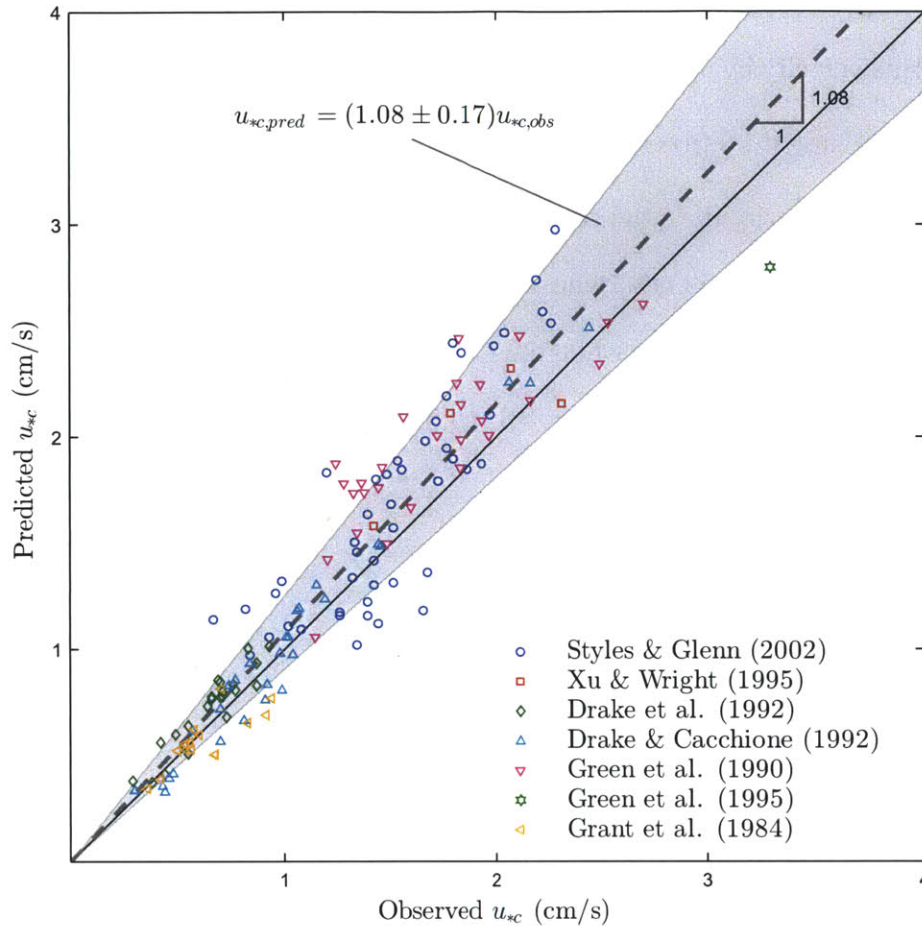
Figure 5-5: Comparison between predicted and observed current shear velocities in the ripple regime using the proposed method to predict the roughness with the 1/10 near-bottom velocity. The solid line denotes perfect agreement while the dashed line shows the average slope of the data points and the gray band covers ±1 standard deviation of the average slope, corresponding to an overprediction of 8±17%.

Although the 1/10 near-bottom velocity was used for the field data with success in Figure 5-4 and Figure 5-5, the roughness was still calculated with the equations developed using the significant near-bottom velocity for the random wave laboratory data. Clearly, to be consistent the same near-bottom velocity should be used in both cases, but the laboratory relationships were tested during development with the 1/10 velocity and gave worse fits. Also, as mentioned previously, there are so few data under random waves relative to periodic waves that the fits found using the significant and 1/10 velocity are quite similar. While the 1/10 velocity gives better results for this limited set of field data, much more field data are required before any conclusion can be made regarding the appropriate near-bottom velocity for these flows.

5.5 Sheet flow regime

As in the ripple regime, the roughness in the sheet flow regime is not easily characterized, so the accuracy of both the roughness method and the theoretical model are being tested simultaneously when the results are compared with field data. To evaluate the model and methods in the sheet flow regime, the roughness was predicted with the skin-friction Shields parameter for the waves alone using the relationships developed from laboratory data, and then the new wave-current model was used with the measured current and wave parameters to predict the current shear velocity.

For the proposed method of predicting the roughness, the energy dissipation factor was predicted with (4.10) and the new energy friction factor model was used to back-calculate the bed roughness. This approach does an excellent job predicting the current shear velocity, giving a bias of 1.05±0.17 (Figure 5-6). If the reverse procedure is used, such that current shear velocity is used to specify the current, the current velocity at 100 cm above the bottom is underpredicted by 3% on average, with a bias of 0.97±0.18.

Since there are only 11 data points in the sheet flow regime, it is difficult to conclude that the proposed roughness method and the new boundary layer model work well in this regime. However, considering that the friction factor relationship was developed with a very small number of laboratory data points under periodic waves with very low density sediment, it is impressive that applying the relationship to combined wave-current flows in the field gives a bias of only 5% for the proposed method.

Figure 5-6: Comparison between predicted and observed current shear velocities in the sheet flow regime using the proposed method to predict the roughness. The solid line denotes perfect agreement while the dashed line shows the average slope of the data points and the gray band covers ±1 standard deviation of the average slope, corresponding to an overprediction of 5±17%.

For the common method, the roughness was predicted with (4.8) where $\gamma_{sf} = 4$ is the best-fit factor for the new model based on the limited laboratory data. The common method with $\gamma_{sf} = 4$ does a reasonably good job predicting the field data: the predictions are biased by a factor of 0.89±0.14 (Figure 5-7).
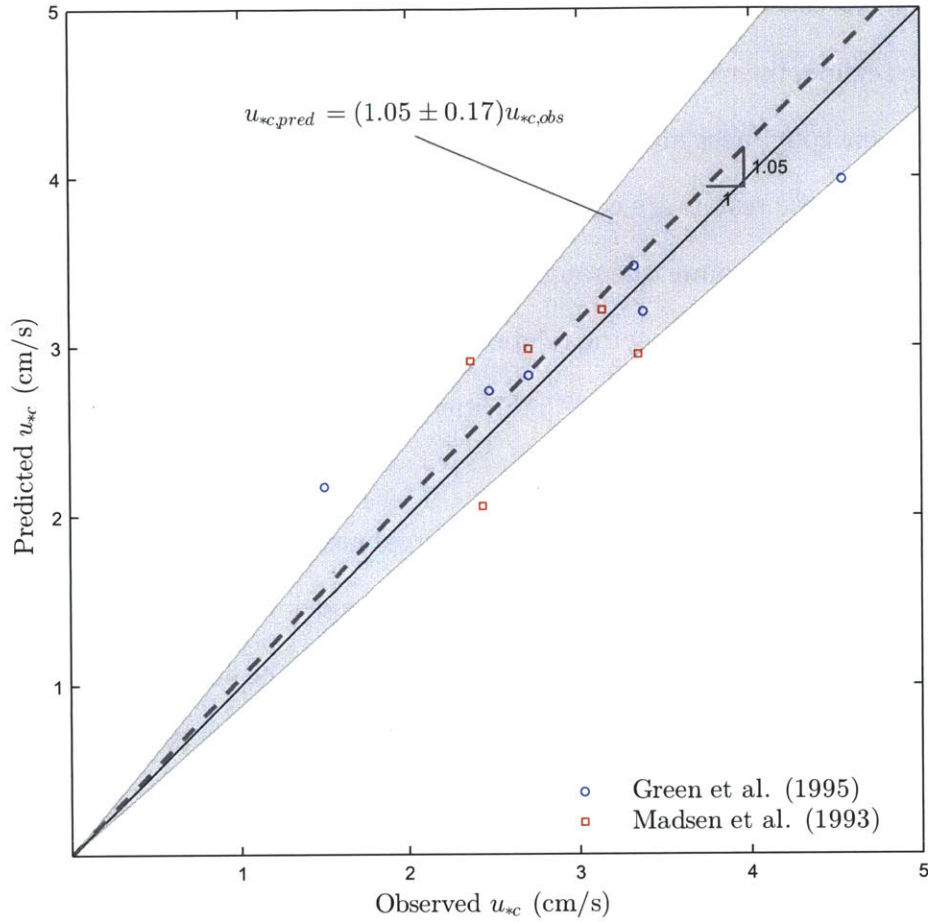
Figure 5-7: Comparison between predicted and observed current shear velocities in the sheet flow regime using the common method with $\gamma_{sf} = 4$ to predict the roughness. The solid line denotes perfect agreement while the dashed line shows the average slope of the data points and the gray band covers ±1 standard deviation of the average slope, corresponding to an underprediction of 11±14%.

Although the two roughness methods were developed with the same set of laboratory data, where the data was used to get the best-fit energy friction factor relationship for the proposed method and to find the best-fit γ_{sf} value for the common method, the common method performs much worse when applied to the field data. In the proposed method, starting from the friction factor, the roughness is found from ψ', S_*, and A_{bm}, whereas in the direct method, the roughness is simply equal to $\gamma_{sf}\psi'd$. Because the direct method has such a simplified form, the constant γ_{sf} is likely not a constant at all, but a function of s, ω, and ν, all of which are accounted for in the proposed method. Therefore, the increased error in the direct method stems from assuming the γ_{sf} value found for laboratory data with very low density

141

sediment ($s \sim 1$), $\gamma_{sf} = 4$, was universally applicable. One solution to this dilemma would be to find an expression for the roughness which depends on ψ' and S_*, as does the roughness relationship in the ripple regime.

If one insists on using the form $k_N = \gamma_{sf}\psi'd$, then it may be possible to find a value of γ_{sf} which is at least more applicable to quartz sediment. While other authors have found similarly small values for γ_{sf}, these were also based on laboratory data with light sediment, while Madsen et al. (1993) found $\gamma_{sf} = 15$ using some of the wave-current field data included in this data set. By fitting the wave-current sheet flow field data in this data set, the least bias is found with $\gamma_{sf} = 14$ when ψ'_{sig} is used, which is a factor of 3.5 larger than the laboratory value. Using this data's best-fit factor of $\gamma_{sf} = 14$ naturally fits the data nearly perfectly, with no bias and a standard deviation of 0.16 (Figure 5-8). While the best-fit factor should be determined from energy dissipation or shear stress measurements in the laboratory, this example at least shows that a single value of γ_{sf} is able to represent all of the sheet flow field data.

The wide variation in γ_{sf} between the laboratory and field data suggests that the factor is not a constant at all, but depends on s and possibly ω and ν. While it may be possible to find a better direct relationship for the roughness in the sheet flow regime, the difficulty with γ_{sf} gives strong support for using the proposed method with the energy friction factor.
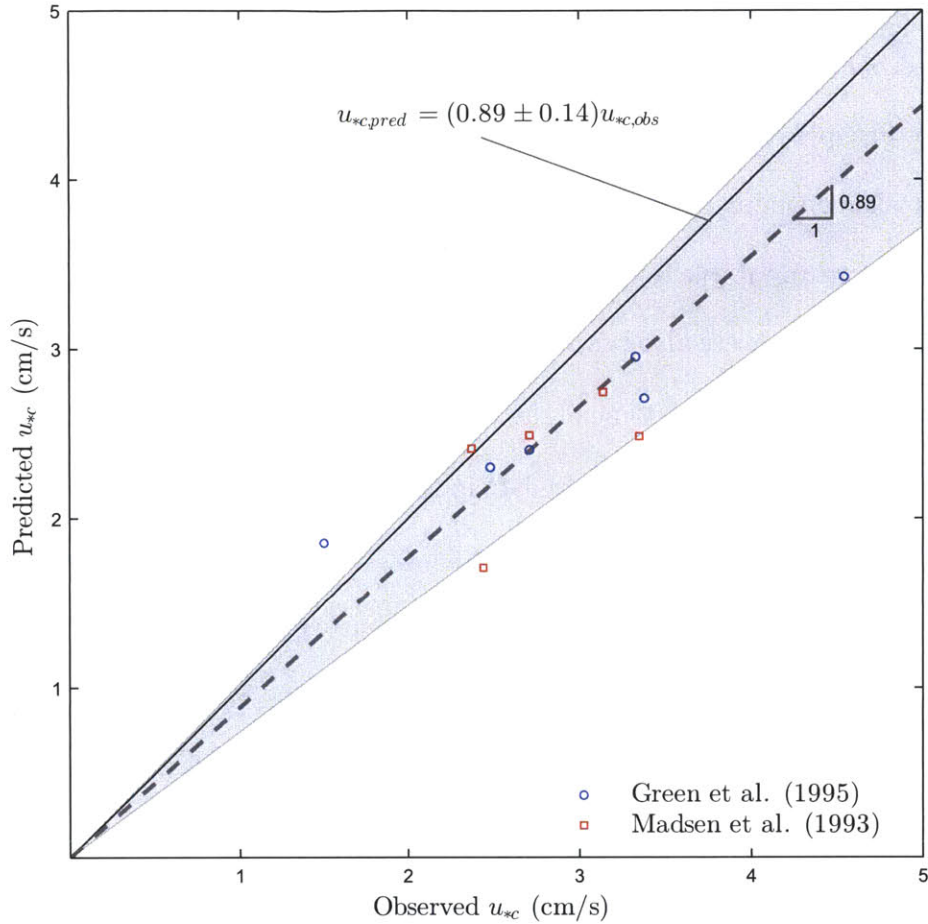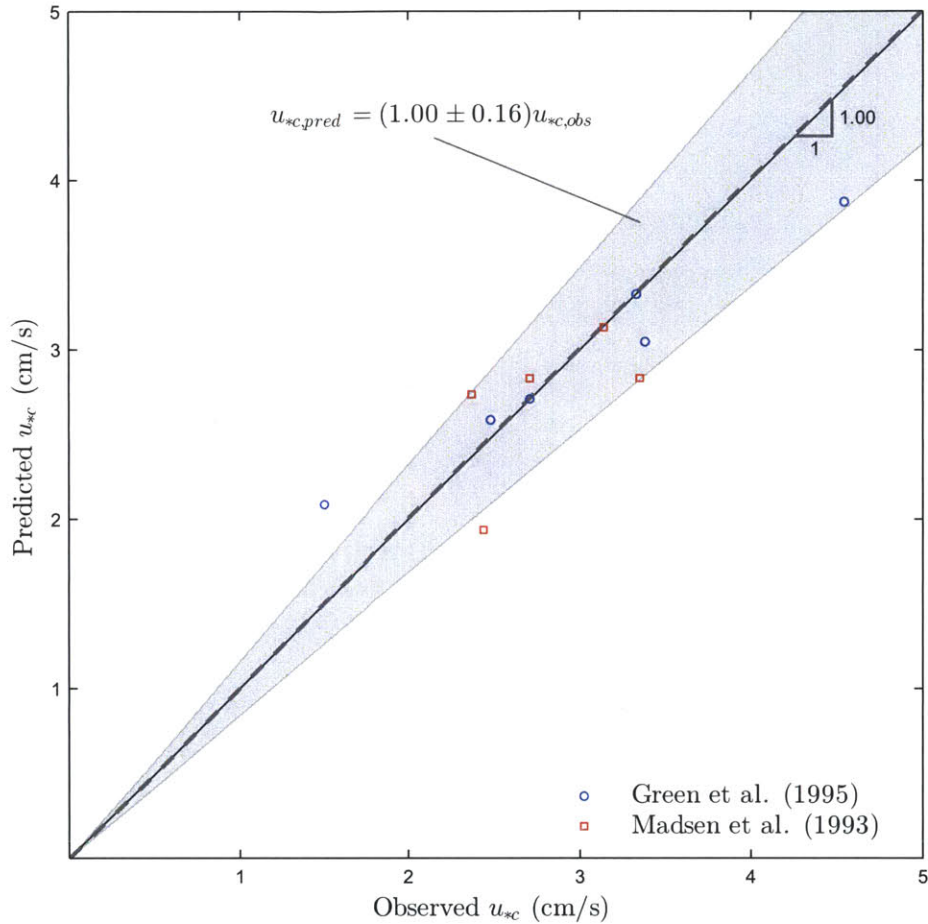
Figure 5-8: Comparison between predicted and observed current shear velocities in the sheet flow regime using the common method with $\gamma_{sf} = 14$ to predict the roughness. The solid line denotes perfect agreement while the dashed line shows the average slope of the data points and the gray band covers ±1 standard deviation of the average slope, corresponding to an overprediction of 0±16%.

As explained in the ripple regime results, there is some evidence that the appropriate near-bottom velocity for field flows may be the 1/10 velocity, and not the significant velocity, as was used in the previous comparison. As with the ripple data, the sheet flow data was also tested with the 1/10 velocity, even though the sheet flow results using the significant velocity were already quite good. Using the 1/10 velocity improves the predictions: the proposed method overpredicts the velocities by 1±17% (Figure 5-9), an improvement of about 4%. Of course, as there are only 11 data points in the sheet flow regime, general conclusions concerning the appropriate velocity are impossible to make.

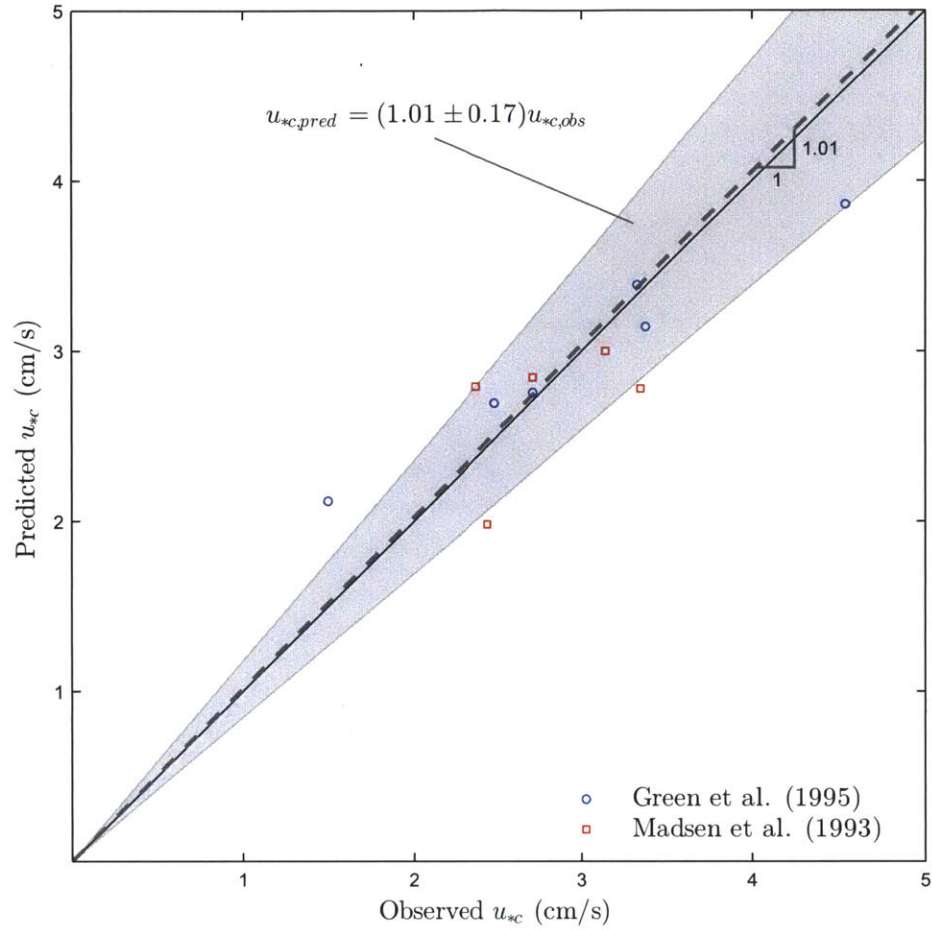Figure 5-9: Comparison between predicted and observed current shear velocities in the sheet flow regime using the proposed method to predict the roughness with the 1/10 near-bottom velocity. The solid line denotes perfect agreement while the dashed line shows the average slope of the data points and the gray band covers ±1 standard deviation of the average slope, corresponding to an overprediction of 1±17%.

Chapter 6

Conclusion

We have developed a turbulent wave-current boundary layer model, in line with the Grant-Madsen type models, which utilizes a three layer time-invariant eddy viscosity structure and consistently applies all three layers to both the current and wave problems. We have also proposed a new method of predicting movable bed roughness in the ripple and sheet flow regimes which, unlike the common method, does not include any model dependent factors and is based on the energy dissipation factor, which can be directly calculated from laboratory measurements. This thesis outlined the derivation of the new wave-current boundary layer theory and the development of the common and proposed empirical roughness methods with laboratory data, and described the initial testing of the theory and methods with combined wave-current field data.

The new three layer wave-current boundary layer theory employs a linear-constant-linear continuous eddy viscosity model, and this same model is used in both the wave and current solutions. The previous Grant-Madsen models used a two layer eddy viscosity structure for the current problem, but inconsistently assumed a linear model for the wave problem. Since solving wave-current problems with the three layer model is rather cumbersome, a simplified two layer model was developed for the current velocity profile. Because the two layer current profile is composed of the outer layers of the three layer profile and the wave model still uses the full three layer model, the results for the simplified two layer profile are equivalent except very near the transition level, which is of negligible importance (Figure 2-3). The simplified two layer

profile is effectively based on a two layer discontinuous eddy viscosity model, like the original Grant-Madsen formulation, and produces a similar current velocity profile with a kink at the transition. The solution procedure is thus similar to the other Grant-Madsen models, but with the wave parameters, such as the friction factor, wave boundary layer thickness, and phase shift, given by the new model. For ease of computation, explicit expressions have been provided for these parameters over a range of the relative roughness. The full coupling of the wave and current problems in this model can be seen in the presence of the parameter $\alpha = u_{*c}/u_{*m}$ in all of the wave parameters, whereas the old models only depended on the relative roughness.

The current velocity profiles predicted by the model compare well with numerical results and with experiments over fixed flat beds. The comparison with the numerical results of Davies et al. (1988) shows that a major weakness of this model, like the previous Grant-Madsen models, is its insensitivity to the wave-current angle (Figure 2-17). The predicted current velocity profiles and the experimental data of Dohmen-Janssen (1999) shows excellent agreement (Figure 2-18). The wave and energy friction factors predicted by the new theory are very similar to those predicted by the more complex time-varying model of Gonzalez-Rodriguez (2009).

From analyzing an extensive set of laboratory data, we found that both the non-dimensional ripple height and wave energy dissipation factor are well represented as functions of the skin-friction Shields parameter, ψ', and the fluid-sediment parameter, S_*. The data from periodic and random waves correlate well when the significant near-bottom velocity is used in the skin-friction Shields parameter for the random waves. The best-fit exponential equations (3.14) and (3.16) represent the data well: 80% of the non-dimensional ripple height data lie within $\pm50\%$ of the best-fit line and 72% of the energy dissipation factor data lie within $\pm25\%$ of the best-fit line. With the roughness taken as $k_N = \gamma_{rb}\eta$ for the common method, the best-fit γ_{rb} factor is found, using the energy dissipation data, to be equal to 16 and 2 for the new and

Jonsson (1966) friction factor models, respectively; the wide variability in this factor is a major drawback of this method.

For the sheet flow regime, laboratory friction factor data was used to develop an expression for the energy friction factor as a function of ψ' and S_* as in the ripple regime. Due to the scatter in the data, a simple linear fit (3.19) was found for the data, with 39% of the data within ±25% of the best-fit line. With the roughness taken as $k_N = \gamma_{sf}\psi'd$ for the common method, the best-fit γ_{sf} factor is found, using the laboratory friction factor data, to be equal to 4 for the new model. Unlike in the ripple regime, due to the form of the roughness expression, the γ_{sf} factor may not be a constant but instead is expected to vary with $s = \rho_s/\rho$ and ω, and as a result the best-fit factor found for the nylon and acrylic laboratory data with $s \sim 1$ is expected to be too small to be applicable to quartz sediment. By directly fitting the energy dissipation data, the proposed method avoids this issue entirely.

The proposed roughness method for the ripple and sheet flow regimes predicts the energy friction factor using the empirical expressions, from which the roughness can be back-calculated using any friction factor model. The proposed method does not require a model-dependent factor, and comes directly from the same friction factor data which is used to find those factors for the common method. Also, the energy friction factor method provides a continuous transition between the ripple and sheet flow regimes.

We showed that the variation of ripple height in the field follows a different trend than in the laboratory, even for random waves. However, we chose not to include field data on ripple dimensions because energy dissipation, used to find the model-dependent γ_{rb}-value in the common method and at the core of the proposed method, can only be reliably measured in the lab. However, while the appropriateness of applying our laboratory-developed equations to field conditions is questionable, we have shown that they provide reasonable predictions of the current shear velocity in combined wave-current flows in the field.

The roughness methods yield acceptable accuracy when applied to combined wave-current field data using the new three layer wave-current theory. In the lower flat-bed regime, where the roughness is simply equal to the sediment diameter, the model underpredicted the current shear velocity by only 1% on average, with a bias of 0.99±0.14. Because the roughness method is well understood in this regime, these results help to verify the accuracy of the new wave-current theory.

In the ripple regime, when the significant near-bottom orbital velocity is used in the skin-friction Shields parameter to predict the roughness of the field flows, the common and proposed methods overpredict the current shear velocity by 20% and 12% on average, with biases of 1.20±0.22 and 1.12±0.19, respectively. Better predictions are obtained when the 1/10 near-bottom orbital velocity is used: the overprediction is reduced to 17% and 8%, and the standard deviations are reduced such that the biases become 1.17±0.20 and 1.08±0.17, respectively. More field data will need to be considered before the appropriate representative near-bottom orbital velocity can be determined.

In the sheet flow regime, using the significant near-bottom orbital velocity in the skin-friction Shields parameter, the proposed method overpredicts the current shear velocity by 5%, with a bias of 1.05±0.17. The common method, however, underpredicts the shear velocity by 11%, with a bias of 0.89±0.14, when $\gamma_{sf} = 4$ is used, which is the best-fit value for the nylon and acrylic laboratory data. For the field data with quartz sediment, a value of $\gamma_{sf} = 14$ is needed to give the smallest bias. This supports the idea that the γ_{sf} value, due to the form of the roughness expression, is not in fact a constant, but depends on the sediment density and possibly the wave frequency. Laboratory data on the friction factor under sheet flow with quartz sediment is necessary to prove this. Using the 1/10 near-bottom velocity with the proposed method improves the predictions in the sheet flow regime; the bias is reduced to 1.01±0.17, for an improvement of 4%. Again, these results imply that the larger near-bottom orbital velocity should be used to predict roughness in the field, but more field data is needed for confirmation.

References

Abramowitz, M., and I. A. Stegun. 1972. *Handbook of Mathematical Functions*. Dover.

Asano, T. 1992. Observations of granular-fluid mixture under an oscillatory sheet flow. Proceedings of the 23rd International Conference on Coastal Engineering. ASCE, Venice, Italy, 1896-1909.

Cacchione, D. A., W. D. Grant, D. E. Drake, and S. M. Glenn. 1987. Storm-dominated bottom boundary layer dynamics on the Northern California continental shelf: Measurements and predictions, *Journal of Geophysical Research*, 92(C2), 1817–1827.

Carstens, M.R., F.M. Nielson, and H.D. Altinbilek. 1969. *Bed Forms Generated in the Laboratory Under an Oscillatory Flow: Analytical and Experimental Study*, U.S. Army Corps of Engineers, Coastal Engineering Research Center, TM-28, Vicksburg, MS.

Clauser, F.H. 1956. The turbulent boundary layer. *Advances in Applied Mechanics*, 4:1-51.

Davies, A.G., R.L. Soulsby, and H.L. King. 1988. A numerical model of the combined wave and current bottom boundary layer. *Journal of Geophysical Research*, 93(C1):491-508.

Dick, J.E., and J.F.A. Sleath. 1991. Velocities and concentrations in oscillatory flows over beds of sediment, *Journal of Fluid Mechanics*, 233: 165-196.

Dingler, J.R. 1974. *Wave Formed Ripples in Nearshore Sands*, Ph.D. Thesis, University of California, San Diego, 136 pp.

Dohmen-Janssen, C. M. 1999. *Grain Size Influence on Sediment Transport in Oscillatory Sheet Flow. Phase Lags and Mobile-Bed Effects*, Ph.D. Thesis, Technical University of Delft, Delft, Netherlands.

Drake, D.E., and D.A. Cacchione. 1989. Estimates of the suspended sediment reference concentration and resuspension coefficient from near-bottom observations on the California shelf, *Continental Shelf Research*, 9(1):51-64.

Drake, D.E., and D.A. Cacchione. 1992. Wave-current interaction in the bottom boundary layer during storm and non-storm conditions: observations and model predictions, *Continental Shelf Research*, 12, 1331-1352.

Drake, D.E., D.A. Cacchione, and W.D. Grant. 1992. Shear stress and bed roughness estimates for combined wave and current flows over a rippled bed, *Journal of Geophysical Research*, 97: 2319-2326.

Faraci, C., and E. Foti. 2002. Geometry, migration and evolution of small-scale bedforms generated by regular and irregular waves, *Coastal Engineering*, 35-52.

Gonzalez-Rodriguez, D. 2009. *Wave Boundary Layer Hydrodynamics and Cross-Shore Sediment Transport in the Surf Zone*. Ph.D. Thesis, Massachusetts Institute of Technology, Cambridge, MA.

Gonzalez-Rodriguez, D., and O.S. Madsen. 2011. Boundary-layer hydrodynamics and bedload sediment transport in oscillating water tunnels. *Journal of Fluid Mechanics*, 667: 48-84.

Grant, W. D., and O.S. Madsen. 1979. Combined wave and current interaction with a rough bottom, *Journal of Geophysical Research*, 84(C4): 1797-1808.

Grant, W. D., and O.S. Madsen. 1982. Movable bed roughness in unsteady oscillatory flow, *Journal of Geophysical Research*, 87: 469-481.

Grant, W.D., and O.S. Madsen. 1986. The continental shelf bottom boundary layer. *Annual Review of Fluid Mechanics,* 18: 265-305.

Grant, W.D., A.J. Williams, and S.M. Glenn. 1984. Bottom stress estimates and their prediction on the Northern California continental shelf during CODE-1: The importance of wave-current interaction. *Journal of Physical Oceanography.* 14:506-524.

Grasmeijer, B.T., and M.G. Kleinhans. 2004. Observed and predicted bed forms and their effect on suspended sand concentrations, *Coastal Engineering*, 51, 351-371.

Green, M.O., J.M. Rees, and N.D. Pearson. 1990. Evidence for the influence of wave-current interaction in a tidal boundary layer, *Journal of Geophysical Research*, 95(6), 9629-9644.

Green, M.O., C.E. Vincent, I.N. McCave, R.R. Dickson, J.M. Rees, and N.D. Pearson. 1995. Storm sediment transport: observations from the British North Sea shelf, *Continental Shelf Research,* 15(8):889-912.

Gross, T. F., and A.R.M. Nowell. 1983. Mean flow and turbulence scaling in a tidal boundary layer. *Continental Shelf Research*, 2:109-126.

Hanes, D.M., V. Alymov, Y.S. Chang, and C. Jette. 2001. Wave-formed sand ripples at Duck, North Carolina, *Journal of Geophysical Research,* 106(C10), 22,575-22,592.

Herrmann, M.J., and O.S. Madsen. 2007. Effect of stratification due to suspended sand on velocity and concentration distribution in unidirectional flows. *Journal of Geophysical Research*, 112(C02006).

Hildebrand, F. 1976. Advanced calculus for applications. 2nd ed., Prentice Hall.

Holmedal, L.E., D. Myrhaug, and H. Rue. 2003. The sea bed boundary layer under random waves plus current. *Continental Shelf Research*, 23:717-750.

Humbyrd, C.J., and O.S. Madsen. 2011. Predicting movable bed roughness in coastal waters, *Proceedings of the International Conference on Coastal Engineering*, No. 32(2010), Shanghai, China. Paper #: sediment.6.

Inman, D.L. 1957. *Wave Generated Ripples in Nearshore Sands*, TM-100, U.S. Army Corps of Engineers, Beach Erosion Board.

Inman, D. L., and A.J. Bowen. 1963. Flume experiments on sand transport by waves and currents, *Proceedings of the 8th Coastal Engineering Conference*, 137-150.

Jonsson, I.G. 1966. Wave boundary layers and friction factors, *Proceedings of 10th Conference on Coastal Engineering*, ASCE, 127-148.

Jonsson, I.G., and N.A. Carlsen. 1976. Experimental and theoretical investigations in an oscillatory boundary layer. *Journal of Hydraulic Research,* 46:75-123.

Kamphuis, J.W. 1975. Friction factor under oscillatory waves. *Journal of the Waterways Harbors and Coastal Engineering Division.* Proceedings of the American Society of Civil Engineering, 101, 135-44.

Kennedy, J. F., and M. Falcon. 1965. *Wave Generated Sediment Ripples*, Hydrodynamics Laboratory, Dept. of Civil Engineering, Massachusetts Institute of Technology, Report 86, Cambridge, MA.

Kim, H. 2004. Effective form roughness of ripples for waves. *Journal of Coastal Research*, 20(3), 731-738.

Kos'yan, R.D. 1988. On the dimensions of passive ripple marks in the nearshore zone, *Marine Geology*, 80, 149-153.

Lambie, J. M. 1984. *An Experimental Study of the Stability of Oscillatory Flow Bed Configurations*, M.S. thesis, Massachusetts Institute of Technology, Cambridge, MA.

Lambrakos, K.F., D. Myrhaug, and O.H. Slaattelid. 1988. Seabed current boundary layers in wave-plus-current flow conditions, *Journal of Waterway, Port, and Coastal Engineering*, ASCE, 114(2), 161-174.

Li, M.Z., and C.L. Amos. 1999. Sheet flow and large wave ripples under combined waves and currents: field observations, model predictions and effects on boundary layer dynamics, *Continental Shelf Research*, 19, 637-663.

Lofquist, K.E.B. 1978. *Sand Ripple Growth in an Oscillatory-Flow Water Tunnel*. U.S. Army Corps of Engineers, Coastal Engineering Research Center, TP-78-5, Fort Belvoir, VA.

Lofquist, K.E.B. 1986. *Drag on Naturally Rippled Beds Under Oscillatory Flows*, U.S. Army Corps of Engineers, Coastal Engineering Research Center, MP-86-13, Vicksburg, MS.

Madsen, O.S. 1994. Spectral wave-current bottom boundary layer flows. *Proceedings of 24th International Conference on Coastal Engineering*, ASCE, 384-398.

Madsen, O.S. 2002. Sediment Transport Outside the Surf Zone. In: Walton, T. (editor), *Coastal Engineering Manual*, Part III, Coastal Processes, Chapter III-6, Engineer Manual 1110-2-1100, U.S. Army Corps of Engineers, Washington, DC.

Madsen, O.S., and W.D. Grant. 1976. Quantitative description of sediment transport by waves. *Proceedings of the 15th International Conference on Coastal Engineering*, ASCE, 1, 492-504.

Madsen, O.S., and P. Salles. 1998. Eddy viscosity models for wave boundary layers. *Proceedings of the 26th International Conference on Coastal Engineering*, ASCE, 2615-2627.

Madsen, O.S., L.D. Wright, J.D. Boon, and T.A. Chisholm. 1993. Wind stress, bed roughness and sediment suspension on the inner shelf during an extreme storm event, *Continental Shelf Research*, 13(11):1303-1324.

Mathisen, P.P. 1989. Experimental Study on the Response of Fine Sediments to Wave Agitation and Associated Wave Attenuation, M.S. thesis, Massachusetts Institute of Technology, Cambridge, MA.

Miller, M.C., and P.D. Komar. 1980. Oscillation sand ripples generated by laboratory apparatus, *SEPM Journal of Sedimentary Research*, 50.

Mogridge, G. R., and J.V. Kamphuis. 1972. Experiments on bed form generation by wave action, *Proceedings of the 13th Coastal Engineering Conference*, 1123-1142.

Mogridge, G., M. Davies, and D. Willis. 1994. Geometry prediction for wave-generated bedforms, *Coastal Engineering*, 255-286.

Myrhaug, D. and O.H. Slaattelid. 1989. Combined wave and current boundary layer model for fixed rough seabeds, *Ocean Engineering*, 16(2), 119-142.

Nielsen, P. 1979. *Some Basic Concepts of Wave Sediment Transport*, Series Paper No. 20, Institute of Hydrodynamics and Hydraulic Engineering, Technical University of Denmark.

Nielsen, P. 1981. Dynamics and geometry of wave-generated ripples, *Journal of Geophysical Research*, 86(C7), 6467-6472.

Nielsen, P. 1983. Analytical determination of nearshore wave height variation due to refraction, shoaling and friction. *Coastal Engineering*, 7, 233-251.

Nielsen, P. 1984. Field measurements of the time-averaged suspended sediment concentration under waves, *Coastal Engineering*, 8, 51-72.

O'Donoghue, T., and G.S. Clubb. 2001. Sand ripples generated by regular oscillatory flow, *Coastal Engineering*, 44, 101-115.

O'Donoghue, T., J.S. Doucette, J.J. van der Werf, and J.S. Ribberink. 2006. The dimensions of sand ripples in full-scale oscillatory flows, *Coastal Engineering,* 53, 997-1012.

Rankin, K.L., and R.I. Hires. 2000. Laboratory measurement of bottom shear stress on a movable bed, *Journal of Geophysical Research*, 105(C7), 17,011-17,019.

Raudkivi, A.J. 1988. The roughness height under waves, *Journal of Hydraulic Research*, 26(5), 569-584.

Ribberink, J. S., and A.A. Al-Salem. 1994. Sediment transport in oscillatory boundary layers in cases of rippled beds and sheet flow, *Journal of Geophysical Research*, 99, 12707-12727.

Rosengaus, M. 1987. *Experimental Study on Wave Generated Bedforms and Resulting Wave Attenuation*, Sc.D. thesis, Massachusetts Institute of Technology, Cambridge, MA.

Sato, S. 1987. *Oscillatory Boundary Flow and Sand Movement Over Ripples*, Ph.D. thesis, University of Tokyo, Tokyo, Japan.

Sato, S., and K. Horikawa. 1988. Sand ripple geometry and sand transport mechanism due to irregular oscillatory flows, *Proceedings of the 21st Coastal Engineering Conference*, 1748-1762.

Sawamoto, M., and T. Yamashita. 1986. Sediment transport rate due to wave action. *Journal of Hydroscience and Hydraulic Engineering*, 4(1), 1-15.

Shields, A. 1936. Application of Similarity Principles and Turbulent Research to Bed-Load Movement, (translation of original in German by W.P. Ott and J.C. van Uchelen, California Institute of Technology). Mitteilungen der Preussischen Versuchsanstalt fur Wasserbau und Schiffbau.

Sleath, A.I. 2004. *Simple models for turbulent wave-current bottom boundary layer flow: theoretical formulations and applications*, M.S. thesis, Massachusetts Institute of Technology, Cambridge, MA.

Styles, R., and S.M. Glenn. 2002. Modeling bottom roughness in the presence of wave-generated ripples, *Journal of Geophysical Research*, 107: 24/1-24/15.

Swart, D.H. 1976. Predictive equations regarding coastal transports, *Proceedings of 15th Conference on Coastal Engineering*, 2:1113-1132.

Thorne, P. D., A.G. Davies, and J.J. Williams. 2003. Measurements of near-bed intra-wave sediment entrainment above vortex ripples, *Geophysical Research Letters*, 30, 4 pp.

Thorne, P. D., J.J. Williams, and A.G. Davies. 2002. Suspended sediments under waves measured in a large-scale flume facility, *Journal of Geophysical Research*, 107, 16 pp.

Traykovski, P., A.E. Hay, J.D. Irish, and J.F. Lynch. 1999. Geometry, migration, and evolution of wave orbital ripples at LEO-15. *Journal of Geophysical Research*, 104(C1), 1505-1524.

Treloar, P. D., and C. L. Abernethy, 1978. Determination of a bed friction factor for Botany Bay, Australia, *Coastal Engineering*, 2, 1-20.

Trowbridge, J. and O.S. Madsen. 1984. Turbulent wave boundary layers. 1. Model formulation and first-order solution. Journal of Geophysical Research, 89(C5):7989-7997.

van der Werf, J.J., J.S. Doucette, T. O'Donoghue, and J.S. Ribberink. 2007. Detailed measurements of velocities and suspended sand concentrations over full-scale ripples in regular oscillatory flow, *Journal of Geophysical Research*, 112, 18 pp.

van der Werf, J.J., J.J.L.M. Schretlen, J.S. Ribberink, and T. O'Donoghue. 2009. Database of full-scale laboratory experiments on wave-driven sand transport processes, *Coastal Engineering*, 56: 726-732.

van Rijn, L.C. 1989. *Handbook of Sediment Transport by Currents and Waves*. Delft Hydraulics, Delft, 450 pp.

van Rijn, L.C. 1993. *Principles of Sediment Transport in Rivers, Estuaries and Coastal Seas*. Aqua Publications, The Netherlands.

van Rijn, L.C. 2007. Unified view of sediment transport by currents and waves. I: Initiation of motion, bed roughness, and bed-load transport, *Journal of Hydraulic Engineering*, 133: 649-667.

Wiberg, P.L., and C.K. Harris. 1994. Ripple geometry in wave-dominated environments, *Journal of Geophysical Research*, 99: 775-789.

Wijetunge, J.J., and J.F.A. Sleath. 1998. Effects of sediment transport on bed friction and turbulence, *Journal of Waterway, Port, Coastal, and Ocean Engineering*, 172-178.

Wikramanayake, P.N. 1993. *Velocity profiles and suspended sediment transport in wave-current flows*, Ph.D. thesis, Massachusetts Institute of Technology, Cambridge, MA.

Wikramanayake, P.N., and O.S. Madsen. 1990. *Calculation of Movable Bed Friction Factors*, Technical Report No. 2, Dredging Research Program, U.S. Army Corps of Engineers, Coastal Engineering Research Center.

Wikramanayake, P.N., and O.S. Madsen. 1994. *Calculation of Movable Bed Friction Factors*, U.S. Army Engineer Waterways Experiment Station, DRP-94-5, Vicksburg, MS.

Williams, J.J., P.S. Bell, P.D. Thorne, N. Metje, and L.E. Coates. 2004. Measurement and prediction of wave-generated suborbital ripples, *Journal of Geophysical Research*, 109: 18 pp.

Wilson, K. 1989. Friction of wave induced sheet flow. *Coastal Engineering*, 12:371-389.

Xu, J.P., and L.D. Wright. 1995. Tests of bed roughness models using field data from the Middle Atlantic Bight, *Continental Shelf Research*, 15: 1409-1434.

Zala Flores, N., and J. Sleath. 1998. Mobile layer in oscillatory sheet flow. Journal of Geophysical Research, 106 (C6), 12783-12793.

Appendix

Mean suspended sediment concentration profile approximation

In section 2.1.1, it was shown that the three layer current velocity profile, found using the three layer eddy viscosity model, can be reduced to an approximate two layer profile that is equivalent to the three layer profile except very near the transition level. The mean suspended sediment concentration profile, which also depends on the eddy viscosity model, can be approximated by a two layer profile with the same transition level as the velocity profile.

The governing equation for the mean suspended sediment concentration, $\bar{c}$, is

$$\nu_t \frac{\partial \bar{c}}{\partial z} + w_{s0}\bar{c} = 0 \tag{A.1}$$

where w_{s0} is the sediment fall velocity. The concentration profile is governed by a reference concentration, c_R, at a level z_R,

$$\bar{c} = c_R \quad \text{at} \quad z = z_R \tag{A.2}$$

The eddy viscosity is the same three layer eddy viscosity model given in (2.7),

$$\nu_t = \begin{cases} \kappa u_{*m}z, & z_0 \leq z < \delta_t \\ \kappa u_{*m}\delta_t, & \delta_t \leq z < \delta_t/\alpha \\ \kappa u_{*c}z, & z > \delta_t/\alpha \end{cases} \tag{A.3}$$

Using this eddy viscosity model in the governing equation for the mean suspended sediment concentration (A.1), the general equation for the concentration at all three levels is given by

$$-\frac{w_{s0}}{\kappa u_{*m}}\bar{c} = \begin{cases} z\dfrac{\partial \bar{c}}{\partial z}, & z_0 < z < \delta_t \\[2mm] \delta_t\dfrac{\partial \bar{c}}{\partial z}, & \delta_t < z < \delta_t/\alpha \\[2mm] \alpha z\dfrac{\partial \bar{c}}{\partial z}, & z > \delta_t/\alpha \end{cases} \tag{A.4}$$

For the bottom layer, where the eddy viscosity is linear, the solution to (A.4) is

$$\bar{c} = C_1 z^{-\frac{w_{s0}}{\kappa u_{*m}}} \tag{A.5}$$

The constant C_1 is found with the reference concentration defined by (A.2), which gives for the profile in the bottom layer

$$\bar{c} = c_R \left(\frac{z}{z_R}\right)^{-\frac{w_{s0}}{\kappa u_{*m}}} \tag{A.6}$$

Then for the intermediate layer, with a constant eddy viscosity, the general solution to (A.4) is

$$\bar{c} = C_2 \exp\left\{-\frac{w_{s0}}{\kappa u_{*m}}\left(\frac{z}{\delta_t}-1\right)\right\} \tag{A.7}$$

The constant C_2 is found by requiring the concentration to be continuous at $z = \delta_t$, which gives

$$\bar{c} = c_R \left(\frac{\delta_t}{z_R}\right)^{-\frac{w_{s0}}{\kappa u_{*m}}} \exp\left\{-\frac{w_{s0}}{\kappa u_{*m}}\left(\frac{z}{\delta_t}-1\right)\right\} \tag{A.8}$$

For the upper layer, the eddy viscosity is again linear, and the general solution to (A.4) is

$$\bar{c} = C_3 \left(\alpha\frac{z}{\delta_t}\right)^{-\frac{w_{s0}}{\kappa u_{*c}}} \tag{A.9}$$

The constant C_3 is found by requiring the concentration to be continuous at $z = \delta_t/\alpha$, which gives

$$\bar{c} = c_R \left(\alpha\frac{z}{\delta_t}\right)^{-\frac{w_{s0}}{\kappa u_{*m}\alpha}} \left(\frac{\delta_t}{z_R}\right)^{-\frac{w_{s0}}{\kappa u_{*m}}} \exp\left\{-\frac{w_{s0}}{\kappa u_{*m}}\left(\frac{1}{\alpha}-1\right)\right\} \tag{A.10}$$

Combined, the full concentration profile is

$$\frac{\bar{c}}{c_R} = \begin{cases} \left(\dfrac{z}{z_R}\right)^{-\frac{w_{s0}}{\kappa u_{*m}}}, & z_0 \leq z \leq \delta_t \\[2ex] \left(\dfrac{\delta_t}{z_R}\right)^{-\frac{w_{s0}}{\kappa u_{*m}}} \exp\left\{-\dfrac{w_{s0}}{\kappa u_{*m}}\left(\dfrac{z}{\delta_t} - 1\right)\right\}, & \delta_t \leq z \leq \delta_t/\alpha \\[2ex] \left(\alpha\dfrac{z}{\delta_t}\right)^{-\frac{w_{s0}}{\kappa u_{*m}\alpha}} \left(\dfrac{\delta_t}{z_R}\right)^{-\frac{w_{s0}}{\kappa u_{*m}}} \exp\left\{-\dfrac{w_{s0}}{\kappa u_{*m}}\left(\dfrac{1}{\alpha} - 1\right)\right\}, & z \geq \delta_t/\alpha \end{cases} \tag{A.11}$$

As was done for the current velocity profile, the three layer concentration profile can be approximated by a two layer profile composed of the top and bottom layers of the three layer profile. The transition level is found by equating the top and bottom velocity profiles at the transition level, $z = \delta_{cw}$, which gives

$$\delta_{cw} = \frac{\delta_t}{e} \alpha^{\left(\frac{1}{\alpha-1}\right)} \tag{A.12}$$

This transition level is exactly the same as was found for the current velocity profile. Therefore, the same simplified two layer discontinuous eddy viscosity model, (2.24), composed of the top and bottom layers of the three layer model, can also be used for the concentration profile.